ISTANBUL TECHNICAL UNIVERSITY ★ GRADUATE SCHOOL OF SCIENCE ENGINEERING AND TECHNOLOGY

DESIGN AND OPTIMIZATION OF CRASH ENERGY MANAGEMENT SYSTEMS ON RAILWAY PASSENGER WAGONS

Ph.D. THESIS

Ahmad PARTOVI MERAN

Department of Mechanical Engineering

Mechanical Engineering Programme

SEPTEMBER 2014

ISTANBUL TECHNICAL UNIVERSITY ★ GRADUATE SCHOOL OF SCIENCE ENGINEERING AND TECHNOLOGY

DESIGN AND OPTIMIZATION OF CRASH ENERGY MANAGEMENT SYSTEMS ON RAILWAY PASSENGER WAGONS

Ph.D. THESIS

Ahmad PARTOVI MERAN
(503092021)

Department of Mechanical Engineering

Mechanical Engineering Programme

Thesis Advisor: Prof. Dr. Tuncer TOPRAK
Co-advisor : Prof. Dr. Ata MUĞAN

SEPTEMBER 2014

İSTANBUL TEKNİK ÜNİVERSİTESİ ★ FEN BİLİMLERİ ENSTİTÜSÜ

YOLCU VAGONLARINDA ÇARPIŞMA ENERJİSİNİN SÖNÜMÜ İÇİN TASARIM VE OPTİMİZASYON

DOKTORA TEZİ

Ahmad PARTOVI MERAN
(503092021)

Makina Mühendisliği Anabilim Dalı

Makina Mühendisliği Doktora Programı

Tez Danışmanı: Prof. Dr. Tuncer TOPRAK
Eş danışman : Prof. Dr. Ata MUĞAN

EYLÜL 2014

Ahmad PARTOVI MERAN a **Ph.D.** student of ITU **Graduate School of Engineering and Technology** student ID **503092021**, successfully defended the **thesis** entitled "Design and Optimization of Crash Energy Management Systems on Railway Passenger Wagons" which he prepared after fulfilling the requirements specified in the associated legislations, before the jury whose signatures are below.

Thesis Advisor :	**Prof. Dr. Tuncer TOPRAK** İstanbul Technical University	.....
Co-advisor :	**Prof.Dr. Ata MUĞAN** İstanbul Technical University	.....
Jury Members :	**Prof. Dr. Alaeddin ARPACI** İstanbul Technical University	.....
	Prof. Dr. Zahit MECİTOĞLU İstanbul Technical University	.....
	Prof. Dr. Mustafa KARAŞAHİN İstanbul University	.....
	Prof. Dr. Erhan Altan Yildiz Technical University	.....
	Doç.Dr. Cüneyt Fetvacı İstanbul University	.....

Date of Submission : 17 July 2014
Date of Defense : 9 September 2014

To my mother, father and my spouse for their support and encouragement,

FOREWORD

I would like to thank my advisers, Prof Dr. Tuncer TOPRAK and Prof. Dr. Ata MUĞAN for their patient guidance and constant support during the courses and thesis studies. I would also to thank all the faculty and staff members of the Department of Mechanical Engineering for their help and support.
I am extremely grateful to my family, for their support, and encouragement throughout my academic years. I also thank my brother, Mr. Yusuf PARTOVI MERAN, for his constant encouragement and support.
I am grateful to the support of the Scientific & Technological Research Council of Turkey (TUBITAK) through of the PhD scholarship for foreign citizens between 2009 and 2012 years.

September 2014

Ahmad PARTOVI MERAN
(Research Assistant)

TABLE OF CONTENTS

Page

FOREWORD ..... **ix**
TABLE OF CONTENTS ..... **xi**
ABBREVIATIONS ..... **xiii**
LIST OF TABLES ..... **xv**
LIST OF FIGURES ..... **xvii**
SUMMARY ..... **xxi**
ÖZET ..... **xxiii**
1. INTRODUCTION **1**
1.1 Purpose of Thesis 4
1.2 Literature Review 4
1.2.1 Crashworthiness of railway passenger cars 4
1.2.2 Thin-walled tubes 14
1.2.3 Honeycomb structures 20
1.3 Crashworthiness Optimization of Thin-Walled Tube by Response Surface Method 25
1.4 Motivation 27
2. EVALUATION OF CRASHWORTHINESS CHARACTERISTICS OF THIN-WALLED TUBES **29**
2.1 Objectives 29
2.2 Crashworthiness Characteristics Definition 29
2.3 Numerical Simulation of Thin-Walled Tubes with Various Cross-Sectional Shapes 32
2.4 Simulation Results of Thin-Walled Tubes with various Cross-Sectional Shapes 35
2.5 Solidity Effects on Crashworthiness Characteristics of Thin-Walled Tubes 40
3. HONEYCOMB STRUCTURES: TEST AND NUMERICAL SIMULATION .. **47**
3.1 Objectives 47
3.2 Honeycomb Structures Test 47
3.3 Description of the FE Model 50
3.4 Effect of Cell Expanding Angle on Crashworthiness Parameters 52
3.5 Effect of Foil Thickness and Cell Size on Crashworthiness Parameters 55
3.6 Effect of Foil Thickness and Cell Side Size on Crashworthiness Parameters 57
3.7 Effect of Impact Velocity and Mass on Crashworthiness Parameters 60
4. DESIGN AND OPTIMIZATION OF PRIMARY ENERGY ABSORBER ELEMENTS **65**
4.1 Objective 65
4.2 Response Surface Methodology Usage for Crashworthiness Optimization 65
4.3 Crashworthiness Optimization of Thin-Walled Tube by RSM 69
4.4 Design and Verification of Energy Absorber Element Response 73
5. CRASH ENERGY MANAGEMENT DESIGN OF RAILWAY PASSENGER CAR **77**

5.1 Objective 77
5.2 Modeling of Conventional Passenger Car 77
5.3 New Crush Zone Design 84
5.3.1 One car collision with rigid wall 84
5.3.2 Crush zone components 85
5.3.3 Orthotropic material modeling of honeycomb structures 86
5.3.4 Simulation of shearing bolts 88
5.3.5 Working mechanism of crush zone system 89
5.4 Crush Zone Integration to the Conventional Passenger Car 91
5.5 Stress Analysis of Passenger Car Integrated with CEM System Under Static Loading 91
5.6 Dynamic Analysis of Passenger Car Integrated with CEM System Under Impact Loading for 50 km/h 96
5.7 Investigation of the Accuracy of Numerical Simulation of Collision 98
5.8 Comparison of Impact Results for CEM and Conventional Car for 50 Km/h ... 100
5.8.1 Force-crush characteristics for 50 km/h impact velocity 100
5.8.2 Shock tolerance of the human body 102
5.8.3 Acceleration-time histories for 50 Km/h impact velocity 103
5.8.4 Secondary impact velocity (SIV) for 50 Km/h impact velocity 104
5.8.5 Velocity-time histories for 50 Km/h impact velocity 105
5.9 Comparison of Impact Results for CEM and Conventional Car for 10 and 15 km/h 106
5.9.1 Stress distribution for CEM and conventional car for 10 Km/h velocity .. 106
5.9.2 Velocity and acceleration-time histories for 10 Km/h impact velocity 110
5.9.3 Stress distribution for CEM and conventional car for 15 km/h velocity .. 112
5.9.4 Velocity and acceleration-time histories for 15 Km/h impact velocity 115
6. CONCLUSIONS AND RECOMMENDATIONS 119
6.1 Thin-Walled Tube Cross-Section Shape and conical angle and Wall Thickness Effect on Crashworthiness Characteristics 119
6.2 Effect of Cell Configuration of Honeycomb Structures on Crashworthiness Parameters 120
6.3 CEM System Benefits to Improve Crashworthiness of Railway Passenger Car 121
6.4 Recommendations 122
REFERENCES 123
CURRICULUM VITAE 131

ABBREVIATIONS

CEM **:** Crash Energy Management
CFE **:** Crush Force Efficiency
CFR **:** Code of Federal Regulations
CPU **:** Central Processing Unit
CS : Crush Strain
DHHC **:** Double-walled Hexagonal Honeycomb Core
GFRP **:** Glass Fiber Reinforced Plastic
EN **:** European Norm
FE **:** Finite Element
FEM **:** Finite Element Method
FMTS **:** Foam-filled Multi-cell Thin-walled Structures
HSLA **:** High Strength Low Alloy
IUC **:** Union of Railways Cooperation
KRG **:** Kriging
PCF **:** Peak Crush Force
PRS **:** Polynomial Response Surface
RBF **:** Radial Basis Function
RSM **:** Response Surface Methodology
RV **:** Relative Velocity
SEA : Specific Energy Absorption
SIV : Secondary Impact Velocity
SNCF **:** French National Railway Company (Société Nationale des Chemins de fer)
SVR : Support Vector Regression
TE **:** Total Efficiency
TEA **:** Total Energy Absorbed
TMT **:** Tailor Made Tubes

LIST OF TABLES

Page

Table 2.1 : Mechanical properties of high strength low alloy steel (HSLA) 350.....34
Table 2.2 : Specifications of tubes with different cross-sectional shape and FE simulation results.....36

LIST OF FIGURES

Page

Figure 1.1 : Accident modes 2
Figure 1.2 : Schematic drawing of in-line impact test by FRA [8]..... 5
Figure 1.3 : Passenger car impact tests of CEM and conventional car [9]. 6
Figure 1.4 : Rigid wall used by FRA in passenger car impact tests [10]..... 6
Figure 1.5 : Photographs of British railway passenger car test [4]. 7
Figure 1.6 : Modes of deformation for different initial speed, in-line loading [15]. .. 9
Figure 1.7 : Linear impact model of two trains collision suggested by Lu [16]..... 10
Figure 1.8 : KRRI train crush zone test designed by ROTEM company [18]..... 10
Figure 1.9 : Multibody dynamics analysis model of KHST [20]. 11
Figure 1.10 : Use of metallic thin-walled tubes as energy absorbers [37]..... 14
Figure 1.11 : Thin-walled tube used in passenger car designed by FRA [5]..... 15
Figure 1.12 : Different honeycomb structure for usage as the shock absorber [55]. 21
Figure 1.13 : Typical load-deflection curve for honeycomb structures [55]. 22
Figure 2.1 : Cross-section of thin-walled tubes. 33
Figure 2.2 : True Stress vs. Strain for HSLA 350 [83]. 34
Figure 2.3 : Load-deformation curve for square cross-section, $\emptyset$=0.15. 37
Figure 2.4 : Load-deformation curve for triangular cross-section, $\emptyset$=0.15. 37
Figure 2.5 : Load-deformation curve for hexagonal cross-section, $\emptyset$=0.15. 38
Figure 2.6 : Load-deformation curve for octagonal cross-section, $\emptyset$=0.15. 39
Figure 2.7 : Load-deformation curve for multi-cell cross-sectional , $\emptyset=0.1$5. 40
Figure 2.8 : Load-deformation curve for multi-cell cross-section, $\emptyset=0.1$5. 40
Figure 2.9 : Variations of CFE with solidity for various cross-sectional shapes..... 41
Figure 2.10 : Variations of the CS with solidity for various cross-sectional. 42
Figure 2.11 : Variations of TE with solidity for various cross-sectional shapes. 43
Figure 2.12 : Variations of η with solidity for various cross-sectional shapes. 43
Figure 2.13 : Variations of ψ with solidity for variuos cross-sectional shapes. 44
Figure 3.1 : (a) Geometric configuration, (b) a sample honeycomb (c) numerical model of honeycomb structure..... 48
Figure 3.2 : MTS machine used for honeycomb structure in and out-of-plane test. 48
Figure 3.3 : (a) Specimen in MTS, (b) Top view and (c) Enlarged view of the honeycomb after the test. 49
Figure 3.4 : Stress-strain curves of specimens during out-of-plane crushing. 50
Figure 3.5 : The FE model with S= 3.175 mm, t= 0.025 mm with 0.1 mm/s..... 51
Figure 3.6 : Numerical and experimental stress-strain results. 52
Figure 3.7 : Impact load-deformation curves as cell expanding angle α changes where v= 14 m/s and m= 0.21 kg, cell number 60..... 53
Figure 3.8 : Variation of normal collapse stress vs cell expanding angle. 53
Figure 3.9 : Variation of crush force efficiency as the cell expanding angle. 54
Figure 3.10 : Variation of total energy absorption vs cell expanding angle. 54
Figure 3.11 : Variation of crush force efficiency as the cell expanding angle. 55

Figure 3.12 : The geometry of honeycomb when mass of the model is constant. 56
Figure 3.13 : Load-deformation curves for different foil thickness and cell size. 56
Figure 3.14 : The crush force efficiency-foil thickness while the total mass is constant. 56
Figure 3.15 : Total energy absorption-foil thickness curve while the total mass is constant. 57
Figure 3.16 : Energy absorber effectiveness factor-foil thickness curve while the total mass is constant. 57
Figure 3.17 : Energy absorber effectiveness -foil thickness curve while the total mass is not constant. 58
Figure 3.18 : Energy absorber effectiveness factor-foil thickness curve while the total mass is not constant. 58
Figure 3.19 : Energy absorber effectiveness factor-foil thickness curve for the constant side size of 3 mm where the total mass is not constant. 59
Figure 3.20 : Crush force efficiency-cell side size curve with constant foil thickness of 0.025 mm where the total mass is not constant. 59
Figure 3.21 : Specific energy absorption-cell side size curve with constant foil thickness of 0.025 mm where the total mass is not constant. 60
Figure 3.22 : Energy absorber effectiveness-cell side size curve for the constant foil thickness of 0.025 mm where the total mass is not constant.....60
Figure 3.23 : Load-deformation curves for various impact mass values while the impact velocity is 5 m/s, cell number 100. 61
Figure 3.24 : Variation of energy absorber effectiveness factor as impact mass values change for the impact velocity of 5 m/s. 61
Figure 3.25 : Load-deformation curves for different impact velocities while the impact mass is 0.6 kg, cell number 100. 62
Figure 3.26 : Variation of energy absorber effectiveness factor as impact velocity changes for the impact mass of 0.6 kg. 63
Figure 4.1 : Bending buckling of pyramidal 69
Figure 4.2 : Peak force of tube respect to thickness and conical angle. 70
Figure 4.3 : Mean force of tube respect to thickness and conical angle. 71
Figure 4.4 : Crush strain of tube respect to thickness and conical angle 71
Figure 4.5 : Total efficiency of tube respect to thickness and conical angle, RSM. . 73
Figure 4.6 : Pyramidal tube dimensions designed for usage in crush zone of CEM. 74
Figure 4.7 : Deformation of thin-walled tube designed for usage in crush zone. 75
Figure 4.8 : Force-Crush behavior of a thin walled tube impact to a rigid plate. 76
Figure 5.1 : Solid model of convetional passenger car N13 Type used by TCDD. . . 78
Figure 5.2 : The dismantled view of N13 type made from St12, Stw24, St52. 78
Figure 5.3 : The dismantled parts of passenger car N13 model fabricated by St372. 79
Figure 5.4 : a) setup for passenger car test, b) and some strain gauges.. 81
Figure 5.5 : The comparisons of the measurements with FE stress results for of 200 tons compression force. 81
Figure 5.6 : The stress distribution in conventional passenger car impact, 50 km/h. 82
Figure 5.7 : The progress of deformation in conventional car crash with 50 km/h. . 83
Figure 5.8 : The force v.s. time variation of conventional car in 50 km/h impact. . . . 83
Figure 5.9 : The schematic impact of one passenger car into a rigid standing wall. 84
Figure 5.10 : The view of crush zone system attached to the end of passenger car. . 86
Figure 5.11 : a) Orthotropic material modeling b) Shell element modeling. 87
Figure 5.12 : A honeycomb specimen with coordinate systems. 87

Figure 5.13 : The finite element model of spot weld failure step.. 89
Figure 5.14 : Working mechanism of crush zone system before installing to car.... 90
Figure 5.15 : The end part of the passenger car with an integrated crush zone..... 91
Figure 5.16 : Schematic loading in static simulation [94]. 92
Figure 5.17 : Von Mises stress distribution for compression force of 1970 kN..... 93
Figure 5.18 : Von Mises stress distribution, compression force in high stress area. 93
Figure 5.19 : Von Mises stress, diagonal compression force of 491 kN. 94
Figure 5.20 : Von Mises stress distribution, diagonal force in high stress area. 94
Figure 5.21 : von Mises stress distribution for tensile force about 1470 kN. 95
Figure 5.22 : Von Mises stress distribution for tensile force in high stress area. 95
Figure 5.23 : The stress distribution in car with CEM for 50 km/h impact. 96
Figure 5.24 : Under-frame views of the CEM passenger car with 50 km/h. 97
Figure 5.25 : The deformation of tubes in the crush zone (50 km/h). 97
Figure 5.26 : Force-crush behavior of the CEM passenger car (50 km/h). 98
Figure 5.27 : Analysis of the energy balance for CEM car simulation (50 km/h).... 99
Figure 5.28 : Post-impact views: (a) side view of CEM car (b) underframe view CEM car, (c) side view of conventional car, (d) underframe view of conventional car for 50 km/h impact velocity. 101
Figure 5.29 : Comparison of the force-crush characteristics for 50 km/h impact. . 101
Figure 5.30 : Shock tolerance of the human body [95]. 102
Figure 5.31 : Acceleration-time histories of the conventional passenger car and passenger car having the CEM system for 50 km/h impact velocity. 104
Figure 5.32 : Acceleration-time histories of the conventional passenger car and the passenger car having the CEM system 50 km/h impact velocity. 105
Figure 5.33 : Velocity-time histories of conventional passenger car and the passenger car having the CEM system. 106
Figure 5.34 : The stress distribution in the conventional car after 10 km/h impact. 108
Figure 5.35 : The stress distribution in the passenger car with an installed CEM system after 10-km/h impact with a rigid wall. 109
Figure 5.36 : Von Mises Stress changes respect to the time after 10 km/h impact velocity. 110
Figure 5.37 : Velocity-time histories of the conventional and the passenger car equipped with the proposed CEM system after 10-km/h impact. 111
Figure 5.38 : Acceleration-time histories of the conventional and the passenger car equipped with the proposed CEM system after 10 km/h impact. 112
Figure 5.39 : The stress distribution in conventional car after impact with 15 km/h velocity. 113
Figure 5.40 : The stress distribution in passenger car with an installed CEM system after 15-km/h impact velocity with a rigid wall. 114
Figure 5.41 : Von Mises Stress changes respect to the time after 15-km/h impact velocity. 115
Figure 5.42 : Velocity-time histories of the conventional and the passenger car equipped with the proposed CEM system after 15-km/h impact. 116
Figure 5.43 : Acceleration-time histories of the conventional and the passenger car equipped with the proposed CEM system after 15-km/h impact. 117

DESIGN AND OPTIMIZATION OF CRASH ENERGY MANAGEMENT SYSTEMS ON RAILWAY PASSENGER WAGONS

SUMMARY

A design approach for crash energy management (CEM) system of railway passenger car has been developed in this thesis. The aim of a crash energy management (CEM) design approach is to absorb the kinetic energy during collision of railway cars in a controlled manner and decrease the acceleration of passengers to reduce fatal injury risks. In this study, the CEM system is composed of a crush zone. The crush zone includes the honeycomb-structured boxes, primary energy absorbers, shear bolts, a sliding sill mechanism and a fixed sill mechanism. The crush zone that is located in the passenger-free space at the end of the passenger car, during the accident collide in progressive and controlled manner and absorb kinetic energy of car. The energy absorber components in the crush zone include honeycomb structure and thin-walled tubes. The shear bolts act as trigger in the system. The sliding sill provides a guide for the crush zone of the passenger car and energy absorber elements to collide systematically. The crush zone is attached to the under-frame of passenger car by fixed sill.

The primary energy absorber inside of the crush zone composed of thin-walled tube. In order to find the optimum design of thin-walled tube with high crashworthiness characteristic, numerical study conducted. The numerical modeling of thin-walled tube has been validated by theoretical studies. The numerical simulation of thin walled tubes crushing pattern are carried out with different cross-sectional shapes. The crashworthiness characteristics of different shape are compared together. The FE simulation result reveals that multi-cell cross-section is effective in increasing energy absorbing factor. But by consideration the another crashworthiness parameters, the comparison results indicate that the square tube with low striker acceleration, stable deformation, and reasonable energy absorption capacity is the favorable cross section geometry as energy absorption elements in passive safety issue. In order to obtain the pyramidal tube dimension with high crashworthiness characteristics, response surface methodology (RSM) and MATLAB optimization tool is used. By changing the thickness of the tube between 4 mm to 10 mm and pyramidal angle between 0º to 4.5º, it is attempted to maximize total efficiency function. The pyramidal angle and tube thickness constraints are limited by global bending collapse pattern and space restrictions on the under-frame of passenger car. The optimum pyramidal angle and thickness are obtained with 3.06º pyramidal angle with 6 mm thickness.

Low energy absorber component in crush zone system is honeycomb structure. Honeycomb structures collide with low and mainly constant average force and provide low acceleration/deceleration in crush patterns. Fabricated honeycomb structures geometry and configuration is limited. Therefore, it is necessary to investigate the optimum configuration of hexagonal honeycomb with high

crashworthiness characteristics. Crashworthiness parameters of aluminum hexagonal honeycomb structures under impact loads are numerically investigated by using the software RADIOSS. To verify the results of explicit nonlinear finite element models, numerical results are compared with experimental measurements and theoretical results presented in literature. It is observed that there are good agreements between numerical, experimental and theoretical results. In numerical simulation of honeycomb structures, out-of-plane loads are considered while the aluminum foil thickness, cell side size, cell expanding angle, impact velocity and mass are varying, and dynamic behavior and crashworthiness parameters are examined. Numerical simulations predict that crashworthiness parameters depend on cell specification and foil thickness of the honeycomb structure, and are independent of impacting mass and velocity. Finally the geometric configuration of hexagonal honeycomb structure with high crashworthiness characteristic has been achieved for application in crush zone of railway passenger car.

In order to investigate the benefits provided by the CEM system, designed crush zone is applied a N13-type used by the Turkish State Railway Company. A full-scale railway passenger car collision with a rigid wall is simulated by using dynamic/explicit finite element (FE) methods. The crushing force, secondary impact velocity, acceleration and velocity curves, and deformation modes are computed to allow a comparison of the crashworthiness performance of a passenger car equipped with the proposed CEM system with that of a conventional passenger car. Comparisons of FE analysis results show that a passenger car incorporating the CEM system has a superior crashworthiness performance to that of the conventional passenger car.

YOLCU VAGONLARINDA ÇARPIŞMA ENERJİSİNİN SÖNÜMÜ İÇİN TASARIM VE OPTİMİZASYON

ÖZET

Lokomotifin ani fren yaptığı, karşıdan gelen başka bir trene çarptığı veya ray üzerinde herhangi bir cisimle çarpıştığı anda yolcu vagonlarında yüksek kinetik enerjisi vagonların raydan çıkmasına, vagonların iç içe girmesine veya vagonların üst üste tırmanmasına neden olmaktadır. Böyle kazalar büyük can ve mal kaybına neden olur. Bu nedenle demir yolu mühendisleri kaza sonucu mal ve can kaybını engellemek veya azaltmak için pasif emniyet yöntemleri önermiştir.

Tez kapsamında, kaza esnasındaki çarpışma enerjisini sönümleme amacıyla demiryolu yolcu vagonlarında Çarpışma Enerjisi Yönetimi (Crash Energy Management-CEM) sisteminin tasarımı geliştirilmiştir. Günümüzde pasif emniyet yöntemi olarak CEM sistemi kullanılmaktadır. CEM sistemi trenlerin seyir hızına ve yapısına bağlı olarak kendilerine özgü yapısal elemanlara ve enerji sönümleme özelliklerine sahiptir. CEM sisteminin görevi, kaza esnasında vagonların kinetik enerjisini kontrollü şekilde absorbe edip, yolculara etki eden ivmeden kaynaklanan atalet kuvvetini azaltarak, can ve mal kaybını en aza indirmektir. Bu amaçla, CEM sisteminin elemanlarının optimum şekilde tasarlanması gerekmektedir. Bu tez çalışması kapsamında CEM sistemini oluşturan yapısal elemanlar incelenmiş, matematik modelleri çıkarılmış, analiz edilmiş, sonlu elemanlar yöntemleri ile hesaplamalar yapılmış ve optimizasyon teknikleri uygulanmış ve optimum bir CEM sisteminin sahip olması gereken özellikler belirlenmiştir.

CEM sisteminin tasarımında, uluslararası standartlardaki ilgili emniyet kriterleri temelinde vagonların kazalara karşı emniyetinin arttırılması ele alınmıştır. Birinci bölümde, yolcu vagonlarında kaza esnasında emniyeti arttırmak için yapılan çalışmalar incelenmiştir. Bunun yanı sıra, literatürdeki ince cidarlı tüpler ve bal peteği yapılarının darbe yükleri altında ezilme davranışları, enerji sönümle özellikleri ve Cevap Yüzeyi Yöntemiyle (Respone Surface Method - RSM) çarpışmaya elverişli (crashworthiness) optimizasyonu incelenmiştir. İkinci bölümde, çeşitli kesit biçimine sahip ince cidarlı tüplerin çarpışmaya elverişli (crashworthiness) özellikleri elde edilmiştir. Üçüncü bölümde, bal peteği yapılarının ezilme davranışları ve çarpışmaya elverişli (crashworthiness) özellikleri, hücre geometrik özelliklerine bağlı olarak deneysel ve sayısal olarak incelenmiştir. Dördüncü bölümde, CEM sistemi için gerekli olan ana enerji sönümleyici komponent tasarımı ve enerji sönümleyici elemanların RSM yöntemiyle optimizasyonu yapılmıştır. Beşinci bölümde, CEM sistemi tasarlanmış, örnek yolcu vagonu üzerine entegre edilmiş, vagonun çeşitli hızlarda çarpışma davranışları incelenmiş ve konvansiyonel vagonun davranışları ile karşılaştırılmıştır. Altıncı bölümde ise çalışma sonuçları ve önerilere yer verilmiştir.

Uluslararası stadartlar tarafından belirlenmiş kriterler göz önünde bulundurularak yolcu vagonlarını kazalara karşı daha güvenli yapmak için değişik sistemler

geliştirilmiştir. Raylı taşımacılıkta CEM sistemi olarak tanımlanan bu sistemler farklı mekanizmalarla çalışmaktadırlar. Bu tez kapsamında geliştirdiğimiz CEM sistemi iki kademeli enerji sönümleme mekanizmasının birleşiminden oluşmaktadır. Literatürde "crush zone" olarak adlandırılan sistem, bu çalışmada "ezilen bölge" olarak isimlendirilmiştir. Ezilen bölge, alüminyum bal peteği yapılar, ana enerji sönümleyici komponent, kesme civataları, kayar taban ve sabit taban mekanizmalarından oluşmaktadır. Enerji sönümleme mekanizması, alüminyum bal peteği yapısının ve ince cidarlı tüplerin çarpışma enerjisini absorbe edilmesini sağlar.

Herhangi bir kaza durumunda vagonlar ilk olarak tampon bölgelerinden darbeye maruz kalırlar. Darbe etkisi ile tamponun içinde bulunan yay sıkışır ve darbe etkisini sönümler. Etki eden darbe şiddeti belli bir değerden fazla olursa kuvvet tamponun sonuna doğru aktarılır ve kesme civatalarının kırılmasına neden olur. Sonuç olarak, alüminyum bal peteği yapı devreye girer ve plastik şekil değiştirerek belli bir miktarda kinetik enerji sönümlenmesini sağlar. Bal peteği yapısında yaklaşık %70-80 oranında plastik şekil değiştirme gerçekleştikten sonra, petek yapının yoğunluğu artarak daha sert hale gelir ve çarpma kuvveti, kayar taban ile sabit taban arasında bulunan civatalara aktarılır. Vagonların kinetik enerjisi sabit taban ve kayar taban aralarında bulunan kesme civatalarının kırılması için yeterli olursa, kesme civataları kırılır ve ana enerji sönümleyici elemanlar devreye girer. Ana enerji sönümleyici elemanların malzemesi, kolay şekil değiştirebilen düşük alaşımlı çelik A350'den seçilmiş ve ince cidarlı tüp şeklinde tasarlanmıştır.

Ana enerji sönümleyici elemanların darbe enerjisini sönümleme açısından optimum biçimini bulmak amacıyla üçgen, kare, altıgen, sekizgen, daire ve çok hücreli kare kesitli tüplerin darbe etkisinde sayısal analizleri yapılmıştır. Tüplerin darbe etkisinde ezilme davranışlarını gerçek sonuçlara yaklaştırmak için darbe similasyonu yapmadan önce burkulma analizi yapılmıştır. Burkulma analizinden elde edilen ilk on burkulma mod şekli düzensizlik (imperfection) olarak darbe analizi için tanımlanmıştır. Analizde, her nodda altı derece serbestliği olan shell elemanlar kullanılmıştır. Sayısal model, literatürde yapılan analitik çalışmaların sonuçlarıyla karşılaştırılarak doğrulanmıştır. Değişik kesit biçimine sahip tüplerin darbe etkisinde davranışları sayısal yöntemle incelenmiştir. İnce cidarlı tüplerde darbe enerjisi sönümleme özelliklerini incelemek için önemli parametreler ortalama ezilme kuvveti, tepe kuvvet, ezilme kuvvet verimi, ezilme birim uzaması, toplam verim, yapısal etkinlik, enerji sönümleme etkinliği, spesifik enerji sönümleme ve toplam enerji sönümleme parametrelerinden oluşmaktadır. Bu parametrelerin tanımları tezde yapılmıştır. Bu özellikler aynı sertliğe (solidity) sahip farklı biçimde tüpler için karşılaştırılmış ve çoklu hücreye sahip tüplerin enerji sönümleme özelliğinin daha fazla olduğu saptanmıştır. Diğer darbe sönümleme özellikleri kapsamında enerji sönümleme elemanı olarak kare kesit tüpler, kararlı şekil değiştirme ve makul enerji sönümleme kapasitesine sahip oldukları için seçilmiştir.

İnce cidarlı tüplerde biçimle birlikte, tüplerin piramit şekli ve cidar kalınlığının da darbe sönümleme özelliklerinde etkili olduğu görülmüştür. Piramit tüplerde malzeme ağırlığını sabit tutup, açı ve kalınlığı değiştirerek darbe sönümleme bakımından optimum koniklik açısı ve kalınlığı belirlemek amacıyla MATLAB programı ve RSM metodu kullanılmıştır. Tüplerin optimizasyonunda kalınlık ve koniklik açısı bağımsız değişken olarak tanımlanırken, toplam verim optimizasyon maliyet fonksiyonu olarak seçilmiştir. RSM yöntemi kullanılarak koniklik açısı 0º-4.5º aralığında ve kalınlık 4-10 mm aralığında değiştirilerek maksimum toplam verim değeri 3.06º koniklik açısı ve 6 mm cidar kalınlığında elde edilmiştir. 3.75º koniklik

açısı ve 8 mm kalınlık üzerinde, tüp kararlı şekil değiştirmesini kaybetmiş ve Euler burkulma modu yani eğilme burkulması ortaya çıkmıştır. Ayrıca, tüplerin koniklik açısı değişkeni, vagonun şasi bölgesinde bulunan alanla da kısıtlıdır.

Ezilme bölgesinin tasarımında ince cidarlı tüplerin yanı sıra bal peteği yapılar da kullanılmıştır. Bal peteği yapılar kaza anında düşük seviyede enerji sönümleyerek ivmenin alt seviyede kalmasını sağlar. Bu yapılar hafif ve sabit ortalama ezilme kuvvetine sahip olduları için darbe sönümleyici elemanı olarak otomobil, uçak ve demir yolu vagonlarında kullanılmaktadır. Bal peteği yapıların enerji sönümleme özellikleri, hücre yapılarının konfigrasyonuna bağlıdır. Bu çalışma kapsamında, bal peteği yapılarınının darbe sönümleme özellikleri üzerine optimum parametre değerlerini belirlemek amacıyla bir çalışma yapılmıştır. Bu yapıların darbe sönümleme özelliklerini incelemek için sonlu elemanlar programı RADIOSS kullanılmıştır. Sonlu elemanlar modelini doğrulamak için testler yapılmıştır. Sonlu elemanlar modelinin sonuçları, yapılan deneylerde alınan ölçümlerle ve literatürde bulunan teorik sonuçlarla karşılaştırılmış ve analiz sonuçlarının bunlarla uyumlu olduğu görülmüştür. Sonlu elemanlar analizlerinde hücre kalınlığı, hücre kenar boyu, hücre açısı çarpma hızı ve kütlesi değiştirilerek düzlem dışı reaksiyon kuvveti elde edilmiştir. Yapının darbe kuvveti etkisinde burkulması ve darbe sönümleme özellikleri incelenmiştir. Çalışmalar sonucunda darbe sönümleme özelliğinin, hücre cidar kalınlığına ve kenar boyuna bağlı olarak değiştiği görülmüştür. Aynı zamanda çarpma hızı ve kütlesinin darbe sönümleme özeliğine etkisi olmadığı ortaya çıkmıştır. Sonuç olarak, küçük hücre kenar boyu ve ince cidarlı hücrelerin daha yüksek darbe sönümleme özelliklerine sahip oldukları belirlenmiştir. Elde edilen sonuçlar, ezilme bölgesinde bal peteği yapıların tasarımında dikkate alınmıştır.

CEM sisteminde vagonun geometrik merkezinin hareket yönündeki ivmesi göz önüne alınarak, bal peteği yapısı ve ince cidarlı tüpler tasarlanmıştır. Enerji sönümleme elemenlarını bir arada tutacak ve onları tetikleyerek devreye girmelerini sağlayacak ara elemanlar, sabit taban ve kayar taban tasarlanmıştır. Sabit tabanla kayar taban arasında bulunan kesme civatalarının, punta kaynağı “spot weld” modeli ile simülasyonu yapılmıştır. CEM sisteminin ezilme davranışları inceledikten sonra istenilen sonuçları elde etmek için, sistemin elemanlarında gereken modifikasyonlar yapıldıktan sonra bir yolcu vagonu üzerine CEM sistemi uygulanmıştır.

Tasarlanan CEM sisteminin vagon üzerinde olan yararlarını incelemek amacıyla ezilme bölgesi, “Türkiye Devlet Demiryolları” tarafından kullanılan N13 tipi vagona uygulanmıştır. CEM sistemi vagon üzerine monte edildikten sonra statik analizler yapılmıştır. EN 12663 (Structural requirements of railway vehicle body) standardına göre yolcu vagonlarını kullanmaya başlamadan önce statik testler, üç farklı yükleme durumuna göre yapılmalıdır. Yükleme durumları basma kuvveti, çekme kuvveti ve diagonal basma kuvvetinden oluşmaktadır. Yapılan statik analizler sonucu, CEM sistemli vagonun statik yükler altında dayanaklı olduğu saptanmıştır.

Konvansiyonel vagonun ve CEM sistemli vagonun rijit duvarla çarpışması, tam ölçekli olarak “dynamic/explicit” sonlu elemanlar ortamında simüle edilmiştir. Bojiler vagonun sonlu elemanlar modelinde, kütle olarak bulundukları bölgedeki düğüm noktalarında tanımlanmıştır. Sınır şartı olarak bojilerin bulunduğu konumdaki düğüm noktalarının düşey yönde hareketi engellenmiş ve diğer yönlerde serbest bırakılmıştır. Her iki vagon türünde 10, 15 ve 50 km/sa hızla rijit duvara çarpma senaryoları modellenmiştir. Simülasyonda rijit duvar sabit tutularak vagona ilk hız tanımlanmıştır. CEM sisteminin darbe sönümleme ve yolcu emniyeti açısından yararını görmek amacıyla ezilme kuvveti, hız, ivme, ikinci darbe hızları,

deformasyonlar ve burkulma modları incelenmiştir. 10 ve 15 km/sa hızla çarpma durumunda her iki türdeki vagonda büyük çapta şekil değiştirmelerinin ortaya çıkmadığı görülmüştür. 50 km/sa hızla çarpışma durumunda konvansiyonel vagonda, vagonun başından yaklaşık olarak 6 metre uzaklıkta büyük bir yerel burkulma gerçekleştiği saptanmıştır. CEM sistemli vagonda kalıcı şekil değiştirmeler, ezilme bölgesinde yani vagonun ön bölümünün ilk 1 metrelik kısmında ve yolcuların bulunmadığı alanda gerçekleşmiştir. Karşılaştırmalar sonucu CEM sisteminin, ivme ve darbe kuvvetinin azaltılmasında etkili olduğu belirlenmiştir. CEM sistemli vagonda ezilme bölgesinin kontrollü şekilde ezildiği ve bu bölge dışında burkulma ve kalıcı şekil değiştirme olmadığı saptanmıştır. Sonuç olarak optimum CEM sistemi tasarımı gerçekleştirilmiş ve bu sistemin yolcu emniyeti ile ilerleyen hasar özellikleri ile yararlı olduğu ortaya konmuştur.

1. INTRODUCTION

Railways are a safer means of public transport. However, the scale of damage to structures, injuries and fatalities in railway accidents are generally higher than those of traffic accidents. Hence, railway crashworthiness engineers intend to minimize injuries and loss of life in accidents. There is a general trend throughout the world to improve the crashworthiness of railway vehicles by passive safety strategies. In collisions of trains, considerable amount of kinetic energy has to be dissipated during collision in a controllable manner. This energy is absorbed in catastrophic deformation modes of passenger car structure.

Typically, in rail equipment, an accident may result in five mode, 1) Telescoping, 2) Overriding, 3) Lateral Buckling, 4) Jackknifing, 5) Derailment. These five modes are illustrated schematically in Figure 1.1.

In a railway accident, telescoping occurs when the underframe of one vehicle overrides that of another, and smashes through the second vehicle's body. The term is derived from the resulting appearance of the two vehicle bodies: the body of one vehicle may appear to be slid inside the other like the tubes of a collapsible telescope the body sides, roof and underframe of the latter vehicle being forced apart from each other. Telescoping often results in heavy fatalities if the cars telescoped are fully occupied. The car riding on top will often be destroyed by the structure of the car below (physics of the incident can often reverse this damage), leaving very little survivable space. The chances of telescoping can be reduced by use of anticlimbers and crash energy management (CEM) structural systems [1-5].

A traditional coupler acts as an essentially rigid link between the cars. In a collision where there are high longitudinal forces present as the cars rapidly decelerate, a small lateral perturbation can cause the cars to become misaligned. When misaligned, the large longitudinal force transferred through the coupler places a lateral force on the adjacent car. Such behavior not only leads to derailment, but can propagate throughout the length of a train and large scale buckling may occur in the

formation of an accordion-like zigzagging pattern between cars. As the cars pile up, side impacts are more likely.

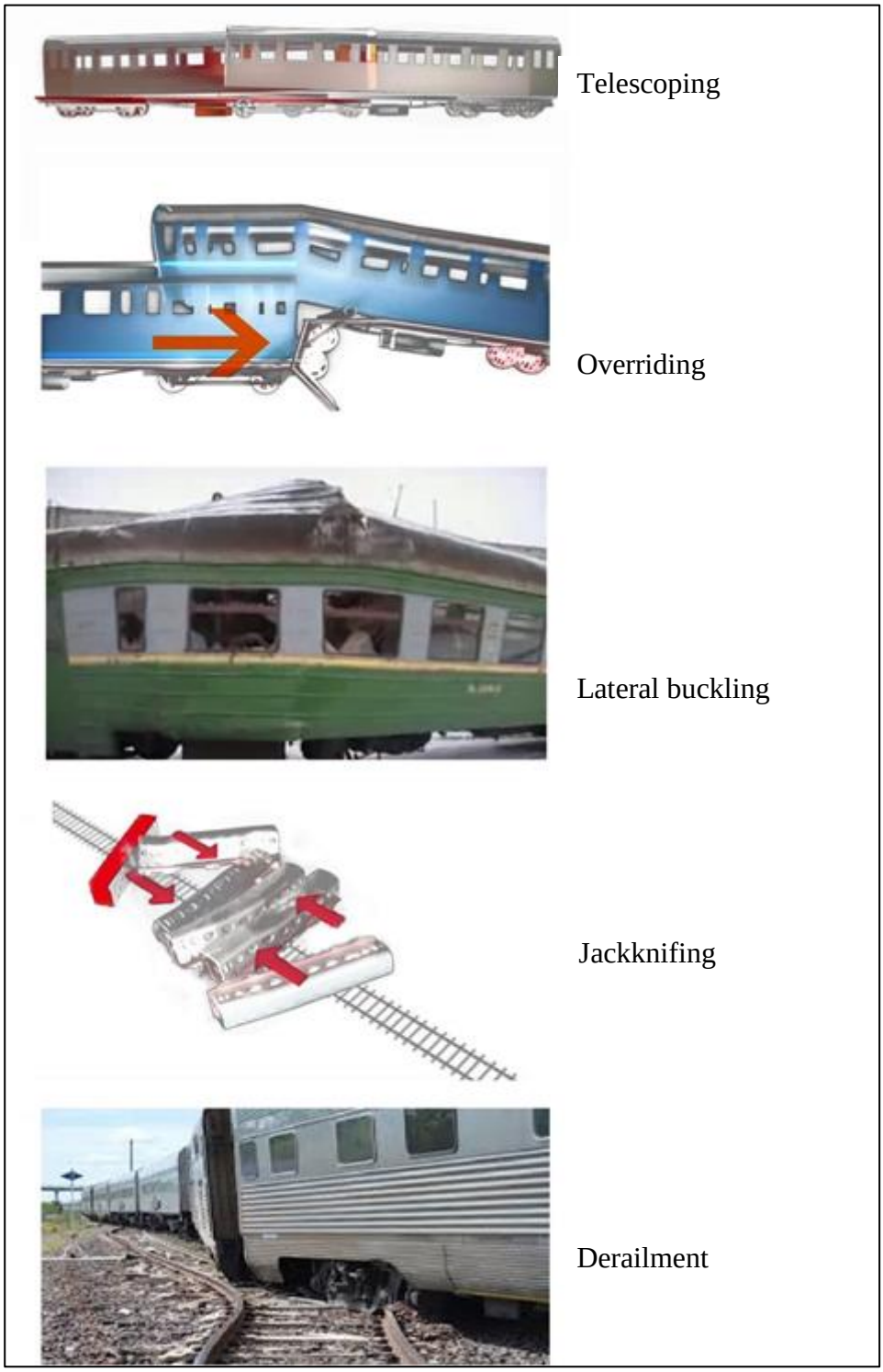

Figure 1.1 : Accident modes [1-5].

Thin-walled tubular structures are widely used in railway and road vehicles to improve the safety of occupants during collision. The research and development of energy absorbing structures and materials, which dissipate kinetic energy during

impact or intense dynamic loading, has received attention since the 1970s [6]. Beside thin-walled tubes, honeycomb structures are used in crashworthiness improvement of vehicle due to their low weight to strength ratio, high-energy absorbing capacity, low cost and good crashworthiness characteristics. For instance, honeycomb structures can be used as shock absorbers in airplanes and high-speed trains for energy absorption during crush. In these events, impact energy is transformed into plastic strain energy and it is absorbed through large compressive strokes of materials. In case of out-of-plane impact, these structures are more effective in terms of energy absorption. The crashworthiness parameters under impact loads are strongly influenced not only by the mechanical properties of the honeycomb material and thickness of the cell wall, but also by the geometric parameters of the honeycomb cell. Crashworthiness is defined as resistance to the effect of a collision. Crashworthiness engineers attempt to increase the structure's ability to protect its contents; these contents could be combustible liquid in fuel tanks or passengers in railcars, automobile or airplane. In all instances, the aim is to improve the safety of the contents by engineering a structure that deforms in a controlled manner and absorbs the kinetic energy. When the contents are passengers, the objectives of crashworthiness engineering could be summarized as: a) Preservation of the occupied space so that the passengers can ride out the collision. b) Limitation of the secondary impacts experienced by the passengers within survivable levels [2]. Crash energy management (CEM) in railway engineering maybe defined as a strategy for managing the collision energy of a train during accident by designing a dedicated area of a railcar and distributing the crush throughout the length of a train. Integration of crush zones on passenger railcars can significantly increase the crashworthiness of passenger rail equipment over conventional railcar design. Crushable crush zones can be designed into unoccupied areas of railcars. CEM improves crashworthiness with crush zone at the ends of the wagons. These zones will be designed to collapse in a controlled manner during a collision, distributing the crush and absorbing the energy among the unoccupied ends of the train cars. This technique preserves the occupied spaces in the train and limits the deceleration of the occupant volumes. To achieve this, the crush zones are required to absorb several million joules of energy and deform progressively as the crush continues, minimizing vertical and lateral wagon motion and preventing override [7-9].

1.1 Purpose of Thesis

The objective of this thesis is to develop a design of a railway passenger car crash energy management system that can be applied to one of the existing Turkish railroad passenger car. Also it is aimed to optimize the crashworthiness performance of primary energy absorber elements in crush zone. Tasks include research and analyses of the existing international crash energy management systems on railway passenger cars, preparing a preliminary design by using analytical and numerical methods for component design, applying optimization methods to energy absorption elements of system, testing of some critical components of the system, and finalizing the design with test and simulation results.

1.2 Literature Review

1.2.1 Crashworthiness of railway passenger cars

The aim of a crash energy management (CEM) design approach is to absorb the kinetic energy during collision of railway cars in a controlled manner and decrease the acceleration of passengers to reduce fatal injury risks. Although the CEM concept has been used in airplane and automobile industries for decades, it has been applied to trains for the last twenty years. In the first published paper [1], design loads of railway passenger vehicles in Europe and the United States are investigated. By examining the UK accident statistics, alternative ways to improve the structural crashworthiness are proposed. A design concept is proposed in [4] to localize the deformation to the vehicle ends and absorb collision energy in a controlled manner to protect the main passenger space. For the same purpose, crush zone systems have been designed and examined in Europe and the United States.

In the last two decades, many research projects have been initiated to improve crashworthiness features of railway vehicles in Europe, United States, Japan and India. Several experimental, finite element analysis and modern multi-body dynamics modeling studies have been conducted to investigate the railway vehicle collision and crashworthiness. Most kind of crush zone systems, impact energy absorber elements and crash energy management strategies are available in literature [7-10].

In the united states the Federal Railroad Administration (FRA) have been conducted a series of tests to evaluate the crashworthiness performance of railway equipment. The collision scenarios selected in tests carried out by FRA are as follow and showed schematically in Figure 1.2.

1. Single-car impact into a fixed barrier

2. Two-car impact into a fixed barrier

3. Cab car-led train collision with standing locomotive-led train

The reported test results conducted by FRA show that the CEM design has superior crashworthiness performance over conventional equipment. In the single-car test of conventional passenger car at a closing velocity of 56 km/h, the car was deformed in length by approximately 2 m. the draft sill was damaged during the impact with plastic deformation extending past the buff stops. As a result of the plastic deformation on the car body structure, the car wheels lifted by about 22 cm from the rail. Single-car with CEM system under the same test condition at a closing velocity of 54 km/h, the CEM car crushed about 1 m, the passenger occupied area was preserved. As results of the controlled crush in the CEM zone, the car wheels remained on the rails.

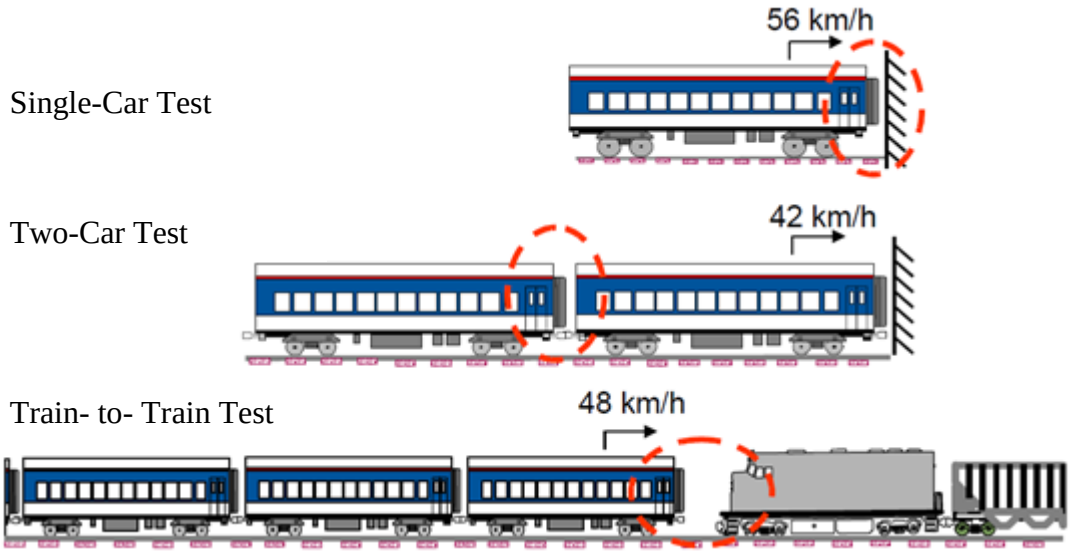

Figure 1.2 : Schematic drawing of in-line impact test by FRA [8].

In the reported results of the two-car test by FRA with a closing velocity of 42 km/h, the impact conventional car crushed in length by approximately 1.83 m. no crush occurred in the trailing car. The plastic deformation of the car body caused the car to raise about 22 cm form the rail. The conventional coupler caused the cars to buckle

laterally. As a result of the misalignment of the couple cars, the trucks adjacent to the coupled connection derailed. In the two-car with CEM system, at a closing velocity of 46.6 km/h, the occupant areas were preserved. The lead car crushed at the front and rear, the trailing car crushed at the front. The push-back couplers allowed the cars to remain in-line with all of the wheels on the rails [5-9].

The reported results for train-train test carried out by FRA showed that the conventional car at a closing velocity of crushed by approximately 6.7 m. the cab car overrode the locomotive. The space for the operator's seat and by approximately 47 passenger seats was lost. In train-train test of cars with CEM system, at the closing velocity of 50 km/h, the front of the cab car crushed by approximately 1 m. all the crew and passenger space was preserved and the controlled deformation of the cab car prevented override.

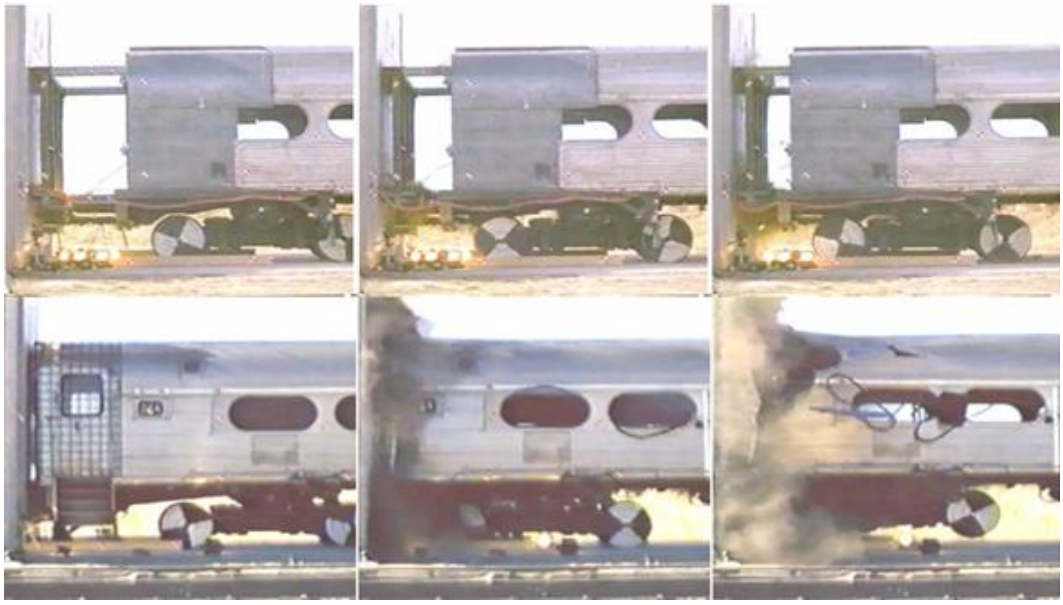

Figure 1.3 : Passenger car impact tests of CEM and conventional car [9].

Figure 1.4 : Rigid wall used by FRA in passenger car impact tests [10].

British Rail Research in 1994 conducted full-scale tests to validate the performance of crush zone designs. The photographs of the test show that crush zone include pushback coupler and anticlimber to prevent override. the reported results demonstrate the train-train test with energy absorption capabilities and crush distribution through the train. Mark I modification car crash energy management system includes push-back coupler with 45° bolted shear plane without energy absorption. This car includes none primary energy absorber elements. By cut-out the existing steel underframe has been modified for some energy absorption [4].

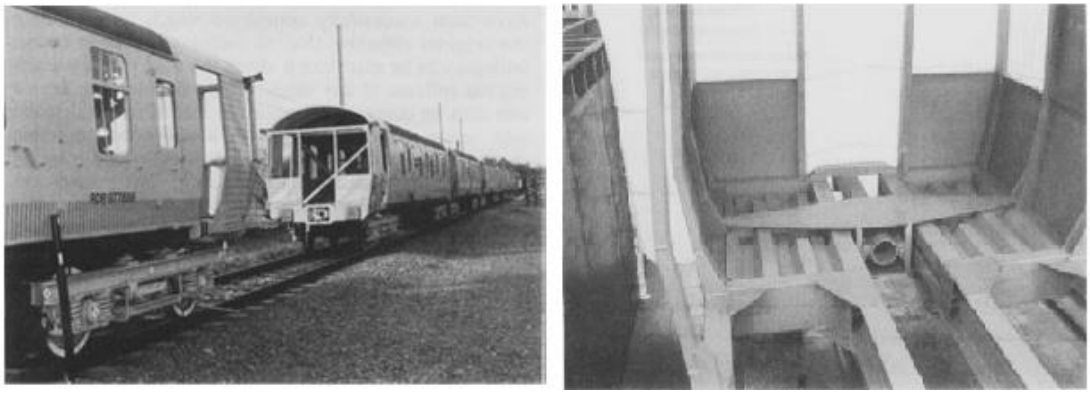

Figure 1.5 : Photographs of British railway passenger car test [4].

In 1997, SAFETRAIN project started in order to design an improved railcar structure to reduce the fatalities and serious injuries in railway accidents in Europe. SAFETRAIN project sponsored by international union of railways cooperation (IUC). SAFETRAIN car, push-back mechanism system consist of shear bolts on push-back coupler with 0.48 MJ energy absorption. Also this car has steel crush zone with 2.17 MJ energy absorption capacity. At coupled interface energy absorption is 0.68 MJ [11].

Between 1994-1996, the French National Railway Company (SNCF) sponsored a number of full-scale tests of TGV passenger cars. As reported by Cleon, Legait and Villemin, these tests have been conducted to qualify the crashworthiness features in the bi-level TGV and the XTER DUM. TGV Duplex intermediate cars crush zone system consist of conventional buffers that interlock and pushback without energy absorption. HSLA in underframe, roof and side members has 2.7 MJ energy absorption. At front and rear of lead vehicle there is 0.54 MJ energy absorption with articulated interface. Also in France, XTER cab car shear bolts on coupler works as push back mechanism with 0.81 MJ energy absorption. Primary energy absorber

system consist of steel crush zone with 3.5 MJ energy absorption and articulated interface with 0.8 MJ energy absorption [12].

Ministry of Railways in India in 2003, started a project to improve the crash behavior of its passenger coaches. By cooperation of USA experts Indian organization carried out necessary crash simulations by using a lumped mass model for two 24-coach trains. They developed new crashworthy design for existing GS and SLR passenger cars. The process of development of crashworthy coach designs was based on simulations using state of art methods and full scale crash testing. The coach has been designed to absorb collision energy in controlled manner. The modified coach designs has a center buffer coupler with a twin draft gear typical to many types of passenger coaches. The rear draft lug is designed to shear away from the draft sill in a collision to allow the car to come into contact with each other in a controlled manner. As the passenger cars collide, the rear draft lug acts as piston to crush a primary energy absorber that is placed behind the draft lug to absorb impact energy. India Railway first full-scale rail vehicle crash test was conducted in 2005. The redesigned prototype crashworthy GS couch collided with a 110 ton platen wagon at a closing speed of 42 km/h. two more crash tests were carried out in 2006. The GS design was further validated at a closing speed of 54 km/h [13].

Other international passenger railway vehicles that have been investigated is Acela cars. For instance, Acela power car has push-back coupler with 1 MJ energy absorption capacity and primary energy absorbers are prismatic stainless steel with 5 MJ energy absorption capacity. In Acela couch car shear bolts with tube expansion which has 1 MJ energy absorption capacity works as push-back mechanism. Also primary energy absorbers include composite cylinders and HSLA (high strength low alloy) underframe, roof and side members with 5 MJ energy absorption capacity [14].

Manufacturing and crash test of railway equipment worth multi-million dollar expenses, therefore computer aided analysis and simulation play an important role in the design and crashworthy evaluation of new equipment. As a result, beside the evolution of crashworthiness design of railcars, analysis of railcar crash behavior has been developed.

The crashworthiness analysis of railcar could be classified in some modeling type: finite element analysis of car body structural crush, collision dynamic analysis and

interior occupant analysis. Each model provides important information to assess the crashworthiness performance of the railway equipment. The finite element analysis evaluates the various deformation modes of car body, stress distribution, crush-load data, car time-velocity and time-acceleration history. This modeling especially important in the design phase in order to design crush zone features that collapse for prescribed loads. Also load-crush behavior of the system is used as a model input to define characteristic of collision dynamic model. The collision dynamic model produces the crush occurred in the car body for a closing speed and gross motions of the car. In secondary impact evaluation, crush-acceleration history can be used. Interior occupant analysis generates the secondary motions experienced by the passengers in different seating arrangements of railway car [10-14].

Priante, Tyrell and Perlman [15] describes a collision dynamic model for one car model and full train model in mutli-level cars in collision with rigid wall. A collision dynamic model is a lumped parameter model, where rigid bodies are connected by springs and are constrained to move in prescribed directions. The model simulates three-dimensional rigid body motion, force-crush characteristics at the front end and transition structures, couplers and car-to-car interactions. Figure 1.6 shows the modes of deformation for different initial speed, in-line loading and symmetric transition structure characteristic. Priante et al [15] extracted the velocity and acceleration trace for the center of masses of the cars and secondary impact velocity and deformation modes of cars in train.

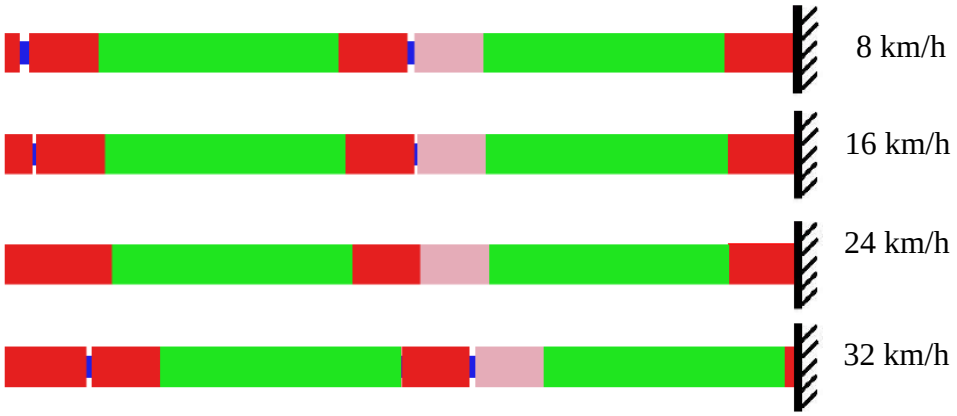

Figure 1.6 : Modes of deformation for different initial speed, in-line loading [15].

Lu [16] studied the energy absorption requirement for crashworthy of trains by suggesting linear and nonlinear model. Lu reported that linear model analysis is very useful in understanding the collision behavior of two trains, particularly the

interaction between the vehicles in collision between two rakes of three or four vehicles would be sufficient to represent the behavior of longer rakes. Figure 1.7 shows the general impact model suggested by Lu. By solving the motion equation for train, energy absorption and force-time histories in interfaces were be calculated [16].

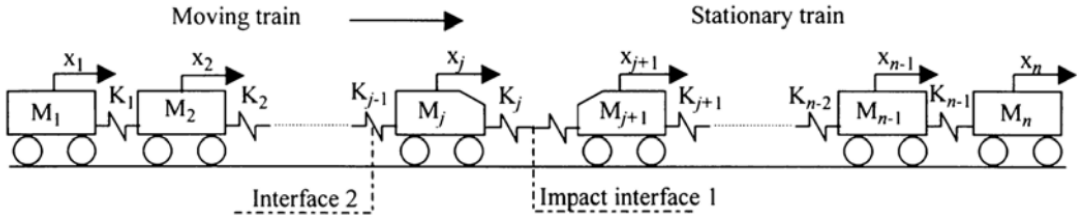

Figure 1.7 : Linear impact model of two trains collision suggested by Lu [16].

Nemeth et al [17] studied the dynamics of train impact to a buffer stop. A simplified model which each car has only one degree-of-freedom, ideal elastic-plastic connections has been developed. They extracted the connection forces and plastic deformation. Circular thin walled tube is employed as energy absorber elements.

KRRI train crashworthiness research team has performed the full-scale crash test of intercity rail cab structures designed by Hyundai ROTEM company. The cab structure has two identical energy absorber in front-end. The test result includes test speed, crush load, energy absorption characteristics and acceleration with respect to time[18].

Figure 1.8 : KRRI train crush zone test designed by ROTEM company [18].

Gao and Tian [19] conducted a finite element simulation of single passenger car impact to rigid wall. The passenger car model 25-type that travel in china railway is

used in simulation. To evaluate the crashworthiness features of car from the united state standards section 238.403 “crash energy management requirements” of 62FR49727 “passenger equipment safety standards” and Federal Motor Vehicle Safety Standard (FM VS.S208) for head and chest injury criterion have been used. Gao and Tian increased the crashworthy of passenger car by changing the geometric configuration of car end [19].

Han and Koo [20] investigated crash behavior of high-speed train by using multibody dynamics. They showed that it is possible to simulate overriding, derailment and lateral buckling by employing three-dimensional crash motion simulation method. The commercial multibody dynamics analysis software DADS is used in their study w. In this method the main parts of a train represented by a body with 6 degrees of freedom and the relative constraints of the bodies are defined using the joints. The Han and Koo’s study, the first 5 frontal cars modeled with detailed multibody dynamic including bogie, suspension element, coupler and car body. The rest of the cars modeled by lumped mass method [20].

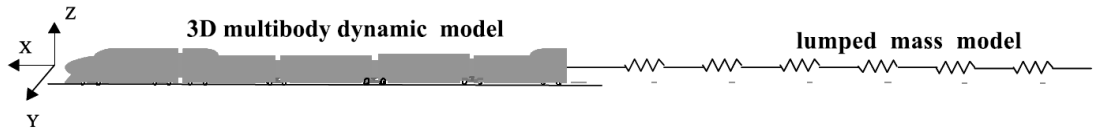

Figure 1.9 : Multibody dynamics analysis model of KHST consists of 20 cars [20].

Xue and et al studied the accuracy of rigid wall and symmetric models in rail vehicle impact stability. They showed a symmetric impact may lead to asymmetric deformations. The symmetric models that only consider a half or a quarter of the structure miscounting relevant on symmetric response. As a result of their study symmetric modeling is unsuitable in the use of structured impact studies. Rigid wall modeling may overestimate crashworthy consequences of cars, therefore this model should be used with caution [21].

Sun et al. [22] reported the modelling and analysis of the crush zone for a typical Australian passenger train. They developed detailed multibody dynamic model of a 3D passenger train. Each passenger car analyzed as fully detailed multibody dynamic model with the nonlinear springs and dampers. The crush zone system includes push back coupler, buffer and crush zone structure. The model established in Gensys. In

order to evaluate the crashworthiness features of passenger car, they carried out the simulation of a single vehicle longitudinally colliding with a fixed barrier [22].

Kirkpatrick et al. [23] compared the various experimental, analytical and computational approaches to evaluate rail vehicle crashworthiness. They used LS-DYNA3D commercial software to simulate the passenger car impact to rigid wall.in the paper there are photographs of finite element simulation of TGV type crush zone system but detail technical information about crush zone has been not included in the paper [23].

Simic and et al. studied about the passive safety elements in railway vehicles. In their study thin-walled tube considered as energy absorber elements in the car during collision. They performed a quasi-static test on square thin-walled tube. Also one type of energy absorber design has been introduced as pipe absorber [24].

Xie and Tian [25, 26] applied multi-body coupling impact model to a whole train. Then obtained the velocity and acceleration characteristics of the cars and secondary impact velocity curves of their occupants. Multi-body coupling impact modeled collision pattern of two trains; one moving at 10 m/s and the other static. Xie and Tian divided the movement of an unrestrained occupant in the compartment into three phases. In the first phase, the railway vehicles struck an obstacle at initial velocity V_0 and decelerated, while the occupant moved uniformly at an approximate velocity V_0 until the free space ran out; the second phase began when this occupant struck the surface of a compartment structure. The RV (relative velocity) of the occupant and train compartment is the SIV of the occupant. In this phase, the velocity of the occupant decreased rapidly, until the RV of occupant and compartment was zero. In the third phase, assuming that the contact between the occupant and the compartment structure was an ideal plastic contact, the occupant remained in contact with the compartment structure and they moved together until they stopped. Their result indicated that by increasing SIV, both the head injury and thoracic cumulative increased 3 ms. The reason why injury severity increased with increasing SIV was that the larger the SIV the more severe the interactions between the occupant and the internal structures of the passenger compartment during a collision, which then caused more severe impact injuries to the occupants [25, 26].

In earlier studies finite element methods used in train's crashworthiness design and collision analysis. Several research results presented on application of aluminum

honeycomb structures as an energy absorber of high-speed train nose and thin walled tubes as main energy absorbers [27-30]. The effectiveness of thin walled tubes in passive safety of railway vehicles in collision is experimentally demonstrated in literature. In addition, the mutli-body dynamic method applied to simulation of high-speed train crashes and analysis of occupant protection strategies in train collision [31-34]. However, there is rare full-scale finite element simulation of passenger car in order to demonstrate the crush zone effect on crashworthiness improvement. In future studies it is possible to simulate the train set collision by applying super-element concept. The crash energy management design philosophy generally includes the selection of a collision scenario against which the protection is to be provided . The scenario selected in this study is the collision of a passenger car with a fixed rigid wall. A single passenger car impact with a rigid wall is a simple and ideal model to reveal the general characteristics of impact behavior of a full-scale car with impact test and computational simulations [8,10]. Earlier investigations have been conducted on the accuracy of rigid wall and symmetric model demonstrate that using a rigid wall model for impacts results overestimate the crashworthy consequence [21]. Nevertheless, rigid wall model widely used in full scale simulation analysis and impact tests, because a single passenger car impact with a rigid wall is a simple and ideal model. It is noteworthy, in this study it is aimed to compare the crashworthiness performance of the CEM system with that of a conventional passenger car. Therefore, that is reasonable to take advantages of simplicity of single car impact to the rigid wall model in terms of time and CPU advantages. However, modeling of whole train set is necessary to evaluate and check the stability, the level of deceleration, the wheels-lift and the carbody strength. In the railroad equipment crashworthiness, there are two standards. In U.S.A., the principal design standard for rail equipment crashworthiness is the Federal Static End Strength Regulation, 49 Code of Federal Regulations (CFR), and paragraph 238.203. Based on this regulation, a passenger rail car structure must be able to support a longitudinal static compressive load of 3.56 MN applied at the buff stops without permanent deformation [35]. Related European standard (EN15227–Railway applications, crashworthiness requirements for Railway vehicle bodies) defines some collision scenarios and passive safety requirements [36].

1.2.2 Thin-walled tubes

Metallic thin-walled tubes are commonly used as energy absorber elements. Besides their high stiffness and strength combined with a low weight they offer a high specific energy absorption capacity when subjected to axial loading. This energy absorption capacity can be used for the purpose of controlled absorption of kinetic crash energy, for example in automobile and train structures to protect passengers from major injuries and to limit severe structural damage to a localize deformation of crash elements. Fig. 1.10 shows examples for the possible use of metallic thin-walled tubes as energy absorbers in the longitudinal frames of automobiles and in the front structure of trains.

More studies have focus on crushing behavior and energy absorption capacity of tubular structures under static, quasi-static or dynamic axial or oblique impact loads. Some studies have been reported on cross-sectional shape effect on crushing behavior of thin-walled tube. For instance, Alavinia and Hamedani [38] compared the energy absorption capacity of thin-walled aluminum tubes with different cross sections. The tubes have the same volume, height, average section area, thickness and material are subjected under axial quasi static loading. Their results indicated that the energy absorption capacity of the circular tubes is the highest and the tapered tubes have the highest crush force efficiency in comparison with other cross sections. Since the maximum force is concerned in impact events, pyramidal and conical tubes are recommended, due to their uniform load–displacement curves and therefore, less difference between the maximum and the average forces.

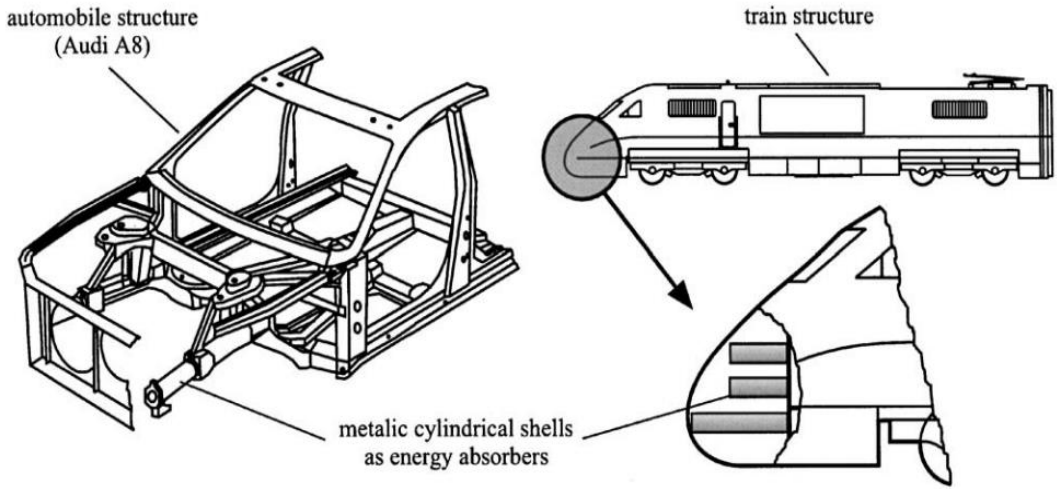

Figure 1.10 : Use of metallic thin-walled tubes as energy absorbers [37].

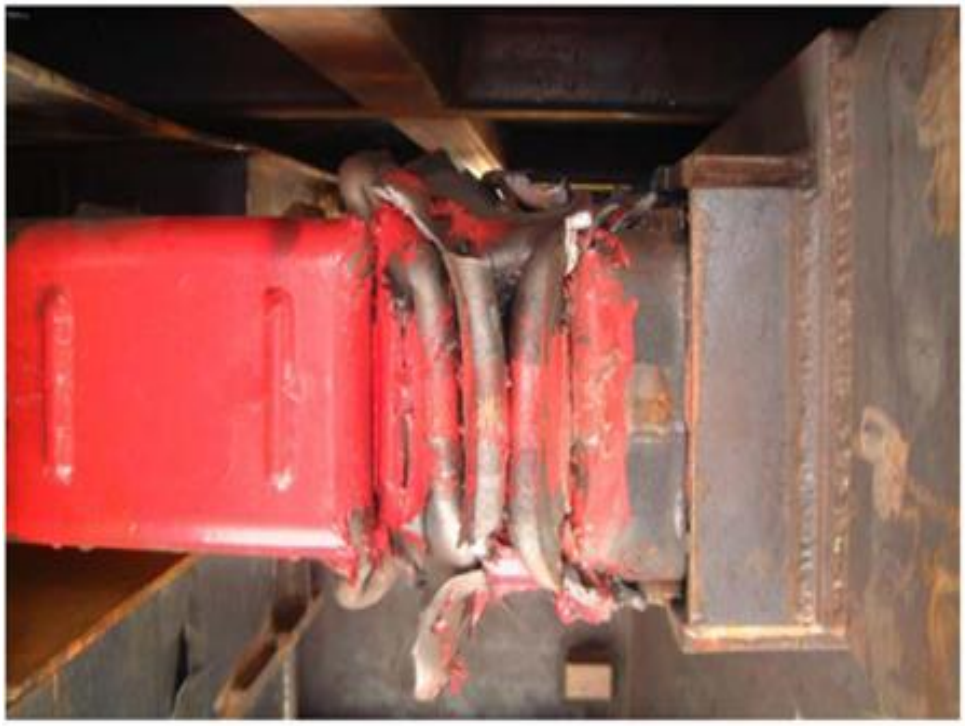

Figure 1.11 : Thin-walled tube used in passenger car designed by FRA [5].

Alavi Nia and Parsapour [39] have compared the energy absorption capacity of muli-cell sections with single shape for triangular, square, hexagonal and octagonal sections under quasi-static loading. They also conducted simulations by using LS-DYNA code. The reported data shows good consistency between the test data and simulation results. Experimental samples showed lower initial peak load in comparison with simulations because on the type of connection. Their results proved that the energy absorption capacity of multi-cell sections is greater than for that of simple section.

Jones [40] reported a study on the energy-absorbing effectiveness factor, which was introduced recently. The factor is defined as the quotient of the total energy, which can be absorbed in a system, to the maximum energy up to failure in a normal tensile specimen, which is made from the same volume of material. This dimensionless parameter allows comparisons to be made of the effectiveness of various geometrical shapes and of energy absorbers made from different materials. The influence of material properties and various geometrical parameters on the value of the dimensionless parameter has been examined for the static and dynamic axial crushing behaviors of thin-walled sections. The influence of foam fillings and the

stiffening of circular and square tubes is examined. It transpires that, according to the energy-absorbing effectiveness factor, an axially crushed circular tube is the most effective structural shape. Moreover multi-cellular cross-sections, and axial stiffening, increases the effectiveness of thin-walled sections. In these latter two cases, the energy absorbed by the additional material in a tensile test is included in the denominator of the energy-absorbing effectiveness factor. The influence of foam filling was found to increase the energy-absorbing effectiveness factor even though the additional energy absorbed by the foam is retained in the denominator. It was also noted that a circular tube, crushed axially either statically or dynamically, and made from an aluminum alloy, had a larger energy-absorbing effectiveness factor than a similar one made from a stainless steel, because the steel had a larger rupture strain which was not required during the deformation of the particular geometry examined.

In real crash pattern, the collapse of thin-walled tubes occurs under axial and oblique loading. Song and Guo [41] investigated the energy absorbing performance of multi-cell and windowed square tubes under dynamic axial and oblique loading numerically. They showed that under axial loading, both windowing method and multi-cell method can significantly increase tube's mean crushing force, and the multi-cell method is more effective. The mean crushing force of windowed tube increases with the increase of tube's wall thickness if no diamond mode occurs. If the thickness is too larger, the mean crushing force of windowed tube may decrease as the tube may collapse in diamond mode. The initial peak force can be reduced by the windowing method, but it increases with the use of multi-cell method. At small load angles, the effectiveness of multi-cell method and windowing method reduces as the load angle increases. The critical load angle of the tube may be decreased by these two methods. So under oblique loading with certain load angles, the multi-cell tube or windowed tube may collapse in bending mode while the conventional tube in axial mode. At large load angle where the conventional tube collapses in bending mode, the multi-cell tube has performance comparable to that of the conventional one. The windowed tube also has mean crushing force comparable than the conventional tube, but with lower initial peak force.

Algalib and Limam [42] studied on the axial crushing of circular aluminum tubes under static and dynamic loadings using both experimental and numerical methods.

Their study indicates that dynamic loading causes an increase in the mean crush force. Also the comparison of the mean crushing force from different analytical solutions and numerical predictions for $10 < D/t < 65$ (D is the diameter of circular tube, t is the thickness of tube) shows good concordance between them. Therefore, with the ability of numerical simulation to predict the crash behavior of thin-walled tubes, this type of analysis is expected to be highly useful in the design and analysis of circular aluminum tubes before actual destructive tests are to be realized.

More studies have been carried out to increase the energy absorption capacity and to reduce initial peak load simultaneously. For instance, Zhang el al [43] studied the effect of a buckling initiator on energy absorption and initial peak force of square thin walled tube. The peak force, mean force and half-length of a fold of the tested specimens are examined. Their results show that the mean crushing force and deformation mode are not affected by the buckling initiator, while the reduction of the peak force strongly depends on the pre-hit height. They also found that the buckling initiator can ensure the deformation more stable and uniform. They introduced a simplified analytical model to study the relationship between the reduction of the peak force and the geometric imperfections; this model can successfully predict the effectiveness of the buckling initiator.

Aljawi et al [44] researched the effect of filler foams on the maximum crush force and the amount of absorbed energy. They reported the results of both an experimental study and a finite element analysis of elastic plastic square steel tubes subjected to dynamic axial impact loadings. Examined tubes are either filled with foams or without foams. Details of the deformation processes are examined using the non-linear facilities of the finite element code ABAQUS. Typical histories of deformation of single steel extrusion tubes and their load-compression curves are presented. Good agreement is reported between the FE deformation histories of tubes with those obtained experimentally for dynamic impact loading. They demonstrated that the use of foams can lead to an increase in energy absorption an approximately 10% reduction in the maximum crush force.

Zhang and Cheng [45] used numerical simulation (nonlinear explicit finite element codes LS-DYNA) to compare the energy absorption properties of single-cell and multi-cell square columns filled by foam. They derived the average forces of these foam-filled columns and multi-cell columns to validate the simulation result with

theoretical predictions. The simulation results indicated that the energy absorption efficiency of multi-cell columns could be between 50% to 100% higher than that of the single-cell columns, which means that multi-cell columns were more attractive than foam-filled columns.

Zhang and Huh [46] researched the energy absorption characteristics of longitudinally grooved square tubes under axial compression by using explicit nonlinear finite element code LS-DYNA. Their results demonstrated that when grooves are introduced on the sidewalls, the specific energy absorption of conventional tubes can be increased by up to 82.7% and the peak force can be reduced by up to 22.3%. The influences of several parameters, including the width of the tube, the length of the groove and the number of the grooves are investigated in their study . Their reported results show that the introduction of groove is an effective way to improve the crashworthiness of thin-walled structures.

Nagel and Thambiratnam [47] studied the energy absorption of tapered thin-walled tube under oblique impact loading by dynamic simulation. They compared the energy absorption response of straight and tapered thin-walled rectangular tubes under oblique impact loading, for variations in the load angle, impact velocity and tube dimensions. Their results showed that the mean load and energy absorption decrease significantly as the angle of applied load increases, due to a change in the failure mode. Tapered tubes display a more stable and gradual decrease in mean load over the transition region. The energy absorption capacity of tapered tubes is greater than for straight tubes of equivalent cross-section dimensions, when the response is dominated by global bending collapse. The energy absorption per unit mass can be increased for a global collapse response by increasing the web width and decreasing the tube length.

Lee et al [48] studied the effect of several types of crush initiators on the energy absorption capacity and maximum crush force of aluminum tubes using FE simulation and quasi-static compressive tests. Their results indicated that the FE simulation results correlated well with the compressive deformation mode, indicating that the simulation was useful for the evaluation of absorbed energy. When triggering dents were introduced at the folding sites pre-estimated by the FE simulation, energy absorption could be improved, and the half-dented specimens absorbed more effectively than the full-dented specimens. On the other hand, when triggering dents

of the same interval were introduced without consideration of the peak location of the folding wave, inhomogeneous deformation, together with overall bending, occurred, and deteriorated energy absorption because energies in bending were not as effectively absorbed as on folding.

Jandaghi Shahi and Marzbanrad [49] studied the energy absorption parameters of tailor-made tubes analytically and experimentally. The axial crush behavior and energy absorption characteristics of four-segmented aluminum tubes with circular cross sections were investigated in their study. In these tubes which are known as Tailor-Made Tubes (TMTs), the length, thickness and mechanical properties of each tube segment varies along the length. All the specimens were crushed under quasi-static compressive loading and their force–displacement curves were obtained. Their results showed that for a constant crush length, these tubes possess higher specific energy absorption than the simple circular tubes.

Hong et al [50] proposed a method to predict the mean crushing force of the triangle tube. They conducted a study including of the collapse mode and energy absorption of triangular tubes, quasi-static axial compression experiments. They derived the deformation curves and collapse modes by the experiments. Based on various combinations of the two basic folding elements, four potential collapse modes were proposed and compared to predict the mean crushing force of the tube theoretically. Also by applying numerical simulations a fitted formula of the mean crushing force was suggested. They compared both the analytical and numerical predictions with the experiments to build an analytical method. As a result they proposed an effective method to predict the mean crushing force of the triangular tube [50].

Mahdi and Sebaey investigated the best cross-section of composite tubes under quasi-static loading. They considered crushing load and energy absorption capacities of tubes for crashworthiness evaluation. Their results showed that the tubes with radial reinforcements had a higher peak load and an average crushing load, crush-load efficiency, absorbed energy, and specific-absorbed energy. Compared to the coreless circular tubes, the tube with two geometrical reinforcements exhibited 41% improvement in the peak load, 98% improvement in the average crushing load, and 38% improvement in the specific-absorbed energy. The tubes with the fuselage-shaped cross section showed a very poor response as compared to the other tubes.

The study results indicated that improving the crashworthiness of composite tubes by internally reinforcing the tubes with GFRP webs is possible [51].

Gupta and Gupta [52] studied the influence of the tube thickness and cone angle on the tube deformation mode numerically and experimentally. A new mode of collapse of shells having combined tube–cone geometry was presented in their study. The mode of collapse forms by the development of one axisymmetric fold towards inner side of the shell followed by the plastic zone. The axisymmetric fold develops fully while plastic zone develops continuously till the end of compression process. During the development of mode of collapse some portions of the shell move radially inward and some radially outward. As the wall thickness of shell specimen increases the load carrying capacity and energy absorption also increases. They found that the semi-apical angle of the cone mainly governed the collapse mode of specimens [52].

Salehghaffari et al [53] conducted an experimental study by adding a rigid steel ring to the upper end of cylindrical aluminum tubes and creating wide grooves on the outside of steel tubes. When the tube was subjected to axial compression, plastic deformation occurred within the space of each wide groove, and thick portions control and stabilize collapsing of the whole structure. In the study, several specimens of each developed design methods with various geometric parameters were prepared and compressed quasi-statistically. Also, some ordinary tubes of the same size of these specimens were compressed axially to investigate efficiency of the presented structural solutions in energy absorption applications. They reported the significant efficiency of the presented design methods in improving crashworthiness characteristics and collapse modes of circular tubes under axial loading [53].

1.2.3 Honeycomb structures

Honeycomb structures are used in various industrial products for their high weight/strength ratio, in which the honeycomb core is commonly sandwiched between flat plates. Further, the honeycomb structure can be used as a shock absorber in impacted objects, e.g., an air-dropped container and a crashed vehicle body. In these events, impact energy is transformed into the energy of plastic deformation and it is absorbed through the large compressive stroke. The honeycomb core exhibits the cyclic plastic buckling deformation. The energy absorption characteristic in impact crush deformation is strongly influenced not only by the mechanical properties of the

honeycomb material and the thickness of cell wall but also by the geometric configuration of the honeycomb cell. Investigations on the energy absorption characteristic or the compressive strength in the out-of-plane crush situation have been performed for aluminum honeycomb panel or core [54], where the honeycomb is compressed in the longitudinal direction of the cell.

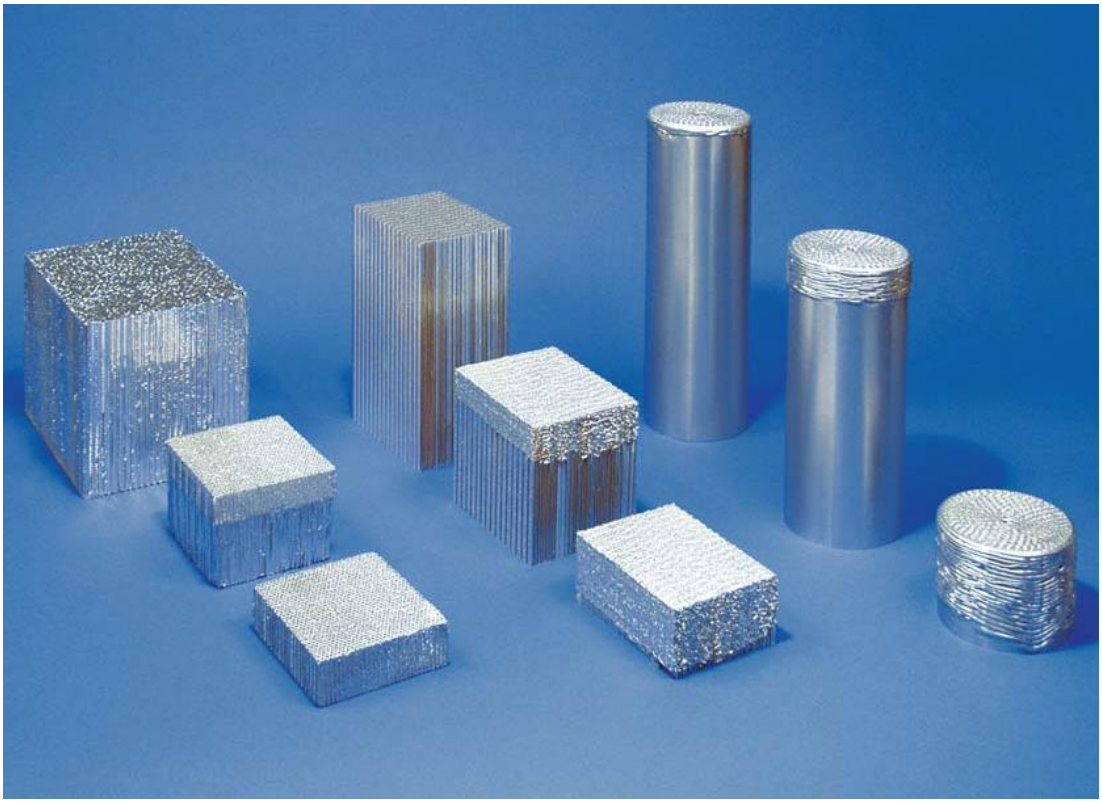

Figure 1.12 : Different honeycomb structure for usage as the shock absorber [55].

Honeycomb absorbs energy by crushing under load. This characteristic has proven to be one of the most reliable and efficient methods of providing "G" limit protection. The definition of some main terms that used in honeycomb structures literature are as follows [55]:

Peak Load: The honeycomb bare compressive strength (specimen not precrushed). **Precrushing**: Prefailing the honeycomb cell walls to eliminate the peak load. Can be accomplished by precrushing the honeycomb.

Stroke: The thickness of honeycomb crushed, usually between 55% to 80% of the initial height.

Minimum Stopping Distance: The vertical dashed line drawn down Figure 1.12, represents a hypothetical stopping distance minimum established in conjunction with the maximum crush level value. This value represents a minimum value for the

maximum crush level line and any crush level selected below the maximum limit will require an increase in this minimum thickness.

Average Crush Load: The average of the peaks and valleys of the crush load, P_{cr}. The peaks and valleys of aluminum and aramid honeycomb are caused by the cell walls buckling and then folding over themselves.

Maximum Crush Level: A horizontal line has been drawn across the curve in Figure 1.13 representing a maximum crush level. If this hypothetical line had been developed as a design maximum, then the actual honeycomb piece P_{cr} value must remain equal to or below this level, P_{cr} maximum for crushing to take place.

Bottomed Out: When the honeycomb is fully crushed to a solid piece, and the load drastically increases. Note: fiberglass honeycomb is just a quantity of resin and broken fiberglass after being crushed.

Energy Absorbed: The energy used in crushing the honeycomb. Calculated as the area under the load-deformation curve, usually P_{cr} times S.

Rebound: After aramid honeycomb is fully crushed, it will regain some of its thickness.

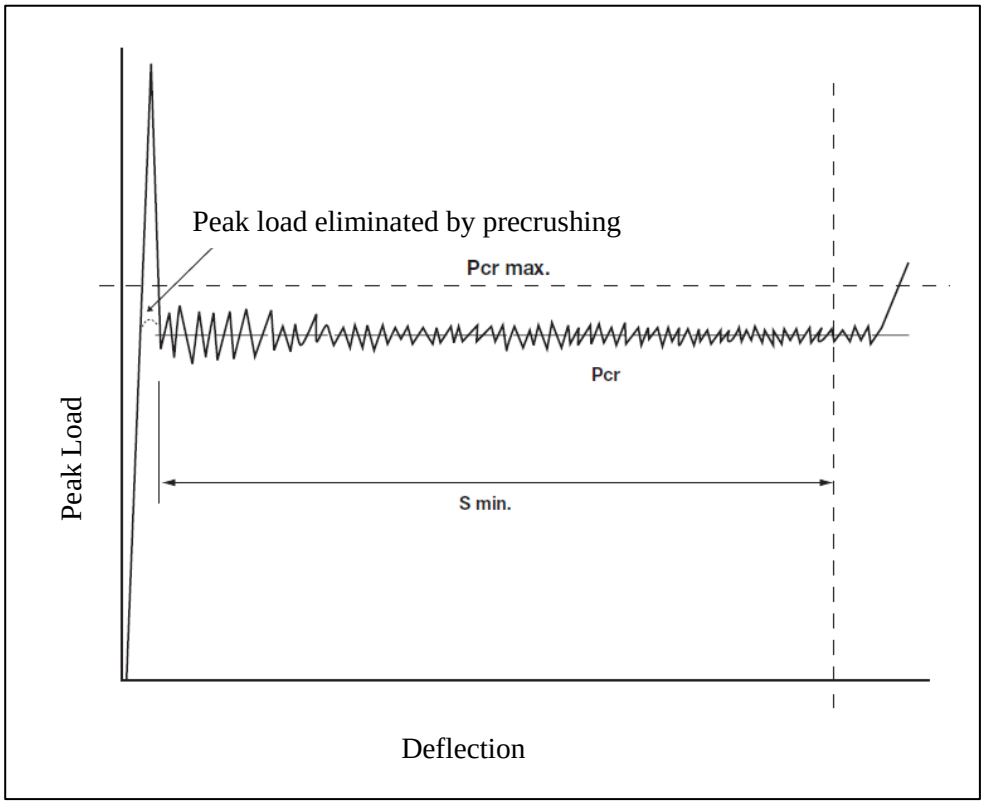

Figure 1.13 : Typical load-deflection curve for honeycomb structures [55].

There are many theoretical, numerical, and experimental investigations on honeycomb structures to determine the mean crush stress and crush behavior. Zhao and Gary [54] used Split Hopkinson viscoelastic pressure bar for dynamic test of aluminum honeycomb structure under out-of-plane and in-plane loads. The post-test observation reported in their study showed that only out-of-plane crushing behavior is affected by the loading rate and the mean crushing pressure was nearly the same for impact velocities from 2 to 28 m/s. In addition, the densification point seems independent of the loading rate (at 65% crush) and the mean crushing pressure for in-plane loading is the same for both dynamic and quasi-static loads. The densification point is between 70% and 80% crush in both directions, which is independent of the loading rate, e.g., see [54].

Zhang and Ashby [56] analyzed crushing behavior of honeycomb structures under both shear loads and simple compression in out-of-plane direction. They derived a theoretical model by consideration of buckling, debonding of adhesives and fracture as possible collapse mechanisms. Their experimental results and theoretical prediction showed that out-of-plane strength of a honeycomb structure is generally independent of the height of the cells and the cell expanding and highly sensitive to the density of the honeycomb material [56].

By using the finite element (FE) method, Deqiang et al [57] investigated the relations between configuration parameters of DHHCs and their out-of-plane dynamic plateau stresses at the impact velocities from 3 to 350 m/s. FE simulations demonstrated, when all configuration parameters are kept constant, mean out-of-plane dynamic plateau stresses are related to impact velocities by conic curves. For a given impact velocity, mean out-of-plane dynamic plateau stresses are related to the ratios between cell wall thickness and edge length and to edge length ratios by power laws. There are complicated relations between mean out-of-plane dynamic plateau stresses and expanding angels [57].

Mellquist and Wass [58] studied the effect of cell size and honeycomb size on energy absorption properties experimentally and numerically; their FE solutions and experimental measurements showed that energy absorption is independent of the number of cells and cell size [58].

Yin and Wen [59] proposed a new theoretical method to determine the mean crushing stress and folding wavelength for honeycomb structures having different

cell specifications. He also simulated a honeycomb structure having the shape of a "Y" column by employing symmetric boundary conditions and bonds of the honeycomb by using a tie-break contact. He showed that numerical results are in good agreement with theoretical results [59].

Gotoh et al [60] studied the crush behavior of a honeycomb structure experimentally and numerically and showed that the crush strength increases slightly as the impact velocity and foil thickness increases. Buckling pattern became irregular as the relative cell dimension to the foil thickness increased. Crush strength was almost proportional to the foil thickness. The honeycomb with smaller cell dimension was considered more proper as an energy absorber from the viewpoint of structural lightness. The maximum value of deceleration of the hammer was found almost constant to the impact velocity.

Yamashita and Gotoh [61] studied experimentally and numerically the effects of the cell shape and foil thickness on the crush behavior of a honeycomb structure. In numerical simulations, by using a single "Y" cross- sectional column model, they showed that crush strength per unit mass gets the largest value when the cell shape is a regular hexagon. hexagon. Although computational and experimental analyses of honeycomb structures are investigated by many researchers in literature, crashworthiness and associated parameters are not studied; thus, motivated by these issues, this study is undertaken to examine crashworthiness and energy absorption characteristics of honeycomb structures.

Hou and et al [62] introduced a numerical virtual model of honeycomb specimen as a small structure to simulate the combined shear-compression behavior of honeycomb structure under impact loading. By using ABAQUS explicit code, they determined the normal behavior and shear behavior of honeycomb specimen under dynamic combined shear-compression. It was found that the normal strength of honeycomb decrease with the increasing shear load.

Hu and Yu [63] analyzed the dynamic behaviors of hexagonal honeycombs from a structural point of view instead of continuum. The reported result was not consistent with that obtained from the theory of continuum, so that the consistency does exist between the two theories on the mechanical behaviors of cellular materials. With the structural point of view as adopted in their study, a thorough analytical formula on the dynamic crushing strength of the honeycomb was obtained by studying the

repeatable collapsing processes of the cell structure. Both of the analytical formulas and the numerical results showed that the dynamic crushing strength of the double-thickness honeycomb was about 1.3 times of that of the single-thickness honeycomb.

1.3 Crashworthiness Optimization of Thin-Walled Tube by Response Surface Method

TrongNhan et al [64] employed response surface method (RSM) to multiobjective optimization in multicell triangular thin-walled tube. The full quartic polynomial basis function was selected for the regression analysis. With two objectives functions of SEA and PCF, the multiobjective optimization problem for minimizing PCF and maximizing SEA was defined by the linear weighted average methods. The wall thickness and cross-section edge length in triangular tube were selected independent variables.

Hou et al [65] adopted RSM method to optimize the complex crashworthiness objective functions for tapered circular tubes. The objective function were the specific energy absorption and the maximum impact load. The ranges of two design independent variables were considered as the taper angle $0.0524 \leq \theta \leq 0.1571$ and foam-filler's density 0.027×10^3 kg/m$^3 \leq \rho \leq 0.27 \times 103$ kg/m^3.

Qi et al [66] optimized the crashworthiness parameters of tapered square tubes under oblique impact loading by using RSM. The wall thickness, t and the taper angle, θ selected as independent variable to maximize the specific energy absorption and minimize the maximum impact load. It was found that the load angle, as well as wall thickness and taper angle have significant effects on specific energy absorption and peak crush force of the multi-cell tubes. Also they showed that a larger taper angle was preferred for both SEA maximization and PCF minimization. The wall thickness, however, shows negative effects on SEA and PCF.

Yin et al [67] in order to maximize the specific energy absorption of foam-filled multi-cell thin-walled structures, used polynomial response surface (PRS), radial basis function (RBF), Kriging (KRG) and support vector regression (SVR) to establish the objective function. It was shown that FMTS with cell number n=9 had excellent energy absorption characteristic.

Fang, et al [68] in a study of the multi-objective optimization of the frontal crush of an automobile chassis. For comparison purpose, RSM and radial basis function methodology were employed together. It was found that the both of them were effective in the optimization of the intricate structure of automobile frontal section. In order to create the response surface an orthogonal sampling array was implemented. An orthogonal polynomial function was chosen as objective function. Additionally, to validate the objective function, dynamic tests were carried out.

Hou, et al [69] optimized a square crush box with multi-cell sections with respect to cell numbers and cell geometrical parameters by using RSM. In their study the objective functions including linear, quadratic, cubic, quadratic and quantic polynomial were employed. It was found that the minimum error was achieved by using a quadratic polynomial objective function.

Liu [70] used RSM method to optimize the crushing behavior of multi-corner, thin-walled columns. In the maximization of SEA, the wall thickness and cross-section edge length were selected independent variables. Various shapes of the impact side of circular tubes were investigated for the maximization of crush performance by Chiandussi and Avalle [71].

Square tapered mild steel tubes were optimized in terms of tube thickness and width and taper angle by Liu [72] by using RSM. It was shown that taper angle had a great effect on the crushing behavior of tube. Lower values of taper angle were shown to improve SEA and mean load/maximum load values. The taper length and the smallest diameter of tube were selected independent variable and the load uniformity (maximum load divided by mean load) dependent variable. The crashworthiness optimization of the circular tubes was studied by Zarei and Kröger [73].

Cho et al [74] studied the shape optimization of a non-uniform closed hat front crash absorber section of an automobile using RSM. Two different crush initiator shapes, rectangular hole-type and circular dent-type, were investigated to maximize the crush energy absorption.

Kim, et al [75] carried out the minimum weight optimization of an Aluminum foam filled S-Frame by using an analytical energy absorption equation as an objective function. The optimized variables, the thickness and cross-section length of the frame and the foam relative density, were validated with the finite element simulations. The

simulation and optimization results showed 5% difference. Zarei and Köreger [76] worked on the optimization of foam-filled Al tubes to maximize SEA for the crush box applications by taking the width of cross-section and foam density as independent variables. The optimum parameters of empty square Al tubes were determined under the maximum mean load constraint. Equivalent SEA values of the optimized empty square tubes were compared with those of the optimized foam filled aluminum tube. Approximately, 20% increase in SEA values was found after the optimization in foam filled tubes.

Zhang et al [77] performed an optimization study on the honeycomb filled bitubular hexagonal columns using Chebyshev's orthogonal polynomial as objective function with the independent variables of inner side length and the thickness of inner and outer wall. With the maximized average mean load, 40% increase in SEA values was found in the optimized bitubal honeycomb filled aluminum tubes.Yamazaki and Han [78] conducted a study to investigate the optimum radius and thickness of cylindrical tubes by using RSM. Also there are more study reported on optimization of energy absorption characteristics of thin-walled tube by using RSM method [79-80].

1.4 Motivation

In literature mainly multi-body dynamic method used to study the train's crashworthiness design and collision analysis. There are limited study on crashworthiness features of railway passenger car with finite element simulation in full-scale. Also in previous studies reported the crash behavior of thin-walled tubes and honeycomb structure, their energy absorption characteristics and their application on high speed train applications. Relatively there are few reported studies on comparison of crashworthiness characteristics of thin walled tubes in terms of energy-absorbing effectiveness factor, crush force efficiency, total efficiency, structural efficiency and crush strain with respect to solidity. Until we achieved there are not reported studies on cross-sectional shapes effect on crashworthiness characteristics of thin-walled tube with consideration of solidity. Also there are not reported studies on the effect of geometric configuration and impacting condition on crashworthiness features of honeycomb structures. In railway application accident may happen with different velocity and moment of inertia of impactor, it is necessary

to conduct investigation on effect of inertia and impactor velocity on crashworthiness behavior of energy absorber elements.

The contributions of this study to literature are investigation of crashworthiness performance of tubes with different cross-sectional shape and determine the cross-section shape with high crashworthiness characteristics. Also determine the hexagonal honeycomb structure configuration with high crashworthiness characteristics. The main originality of this study, is to design of a crush zone system with optimum energy absorber elements from crashworthiness point of view under dynamic loads that applicable to railway passenger cars. For instance in this study the crush zone system is applied to a N13-type passenger car that used by the Turkish State Railway Company. Full-scale finite element simulation of collision with a rigid wall is conducted both for conventional and passenger car having CEM.

2. EVALUATION OF CRASHWORTHINESS CHARACTERISTICS OF THIN-WALLED TUBES

2.1 Objectives

Thin-walled tubes are widely used in energy absorption systems of railway equipment and vehicle. Therefore it is necessary to research and analyze the crashworthiness features of these structures here. The objectives of this chapter are to study the crushing behavior of thin-walled tube under dynamic impact loading and determine crashworthiness characteristics of thin-walled tubes. Relatively there are few reported studies on comparison of crashworthiness characteristics of thin walled tubes in terms of energy-absorbing effectiveness factor, crush force efficiency, total efficiency, structural efficiency and crush strain with respect to solidity. until we achieved there are not reported studies on cross-sectional shapes effect on crashworthiness characteristics of thin-walled tube with consideration of solidity as well as striker acceleration. Here we investigate the influence of cross-sectional shape, solidity ($\varnothing$), and taper angle (α) on crashworthiness characteristics of thin-walled tubes. For this purpose, numerical modeling is conducted for tubes with triangular, square, circular, hexagonal, octagonal, multi-cell cross-sectional shapes. The tubes have the same mass and length and crashworthiness performance comparison is carried out in identical solidity. The crush force efficiency (*CFE*), crush strain (*CS*), total efficiency (*TE*), structural efficiency (η), dynamic energy absorbing effectiveness (ψ') and striker mean acceleration (a_m) parameters are obtained for tubes with respect to solidity parameter.

2.2 Crashworthiness Characteristics Definition

Crush force efficiency: Crush force efficiency (CFE) is the ratio between the mean crushing force (F_m) and the maximum crushing force (F_{max}). Mean crushing force F_m for a typical deflection δ can be calculated as

$$F_m = \frac{\int_0^{\delta} F(x)dx}{\delta} \quad \textbf{(2.1)}$$

F(x) is the crushing force in force-deflection curve. Maximum crushing force F_{max} is the first peak force in force-deflection curve.

$$CFE = \frac{F_m}{F_{max}} \quad \textbf{(2.2)}$$

CFE parameter evaluates the performance of the tube during crushing process.

Crush strain: crush strain (CS) is the ratio between the crushing length to the total length of tube and can be calculated as

$$CS = \frac{L_f - L_i}{L} \quad \textbf{(2.3)}$$

where L_f and L_i are the final and initial crushing distance respectively. L is the length of the tube.

Total efficiency (TE): in order to assist the crashworthiness efficiencies of thin-walled tube the dimensionless parameter TE presented in literature. TE is defines as total energy absorbed in unit length of tube divided by the maximum force. In crashworthiness studies the maximum value of TE for a given energy absorber is desired.

$$TE = \frac{E}{F_{max}L} \quad \textbf{(2.4)}$$

where E is the total energy absorbed, F_{max} is maximum force and L is the length of the tube. Total energy absorbed can be obtained by multiplication of mean force F_m and crush distance $L_f - L_i$.

Eq. (2.4) may be written in form

$$TE = \frac{F_m(L_f - L_i)}{F_{max}L} = CFE \times CS \quad \textbf{(2.5)}$$

Therefore TE can be calculated by multiplication of crush force efficiency and crush strain.

Structural effectiveness is a ratio between the mean crushing force and the squash load [6]. σ_0 is the plastic flow stress, p_m is the mean crushing force and A is the cross-section area of thin- walled tube cross section.

Structural effectiveness: structural effectiveness is defined as

$$\eta = \frac{P_m}{A\sigma_0} \tag{2.6}$$

In order to compare the crashworthiness characteristics of thin walled tube solidity ratio is kept fixed for all tubes. Solidity ratio is defined as

$$\emptyset = A/A_1 \tag{2.7}$$

Here A_1 is the enclosed total area of the section and A is the material area of the cross section of tube [6].

Energy-absorbing effectiveness: energy-absorbing effectiveness factor is defined as the division of the total energy, which can be absorbed in a system, to the maximum energy up to failure in a normal tensile specimen, which is made from the same volume of material [40]. It can be calculated as follows:

$$\psi = \frac{3mV_0^2}{8\sigma_0 A\delta_f \varepsilon_r} \tag{2.8}$$

where m and V_0 are the mass of striker and initial impact velocity respectively, A is the cross-sectional area of a thin-walled section, δ_f and ε_r are the final axial displacement and rupture strain respectively. σ_0 is the dynamic flow stress and could be calculated as $\frac{1}{2}(\sigma_y + \sigma_u)$.

Total Energy Absorption: The area under the load-displacement curve which represents the Total Energy Absorption (TEA) is given by

$$TEA = \int P_i ds \tag{2.9}$$

Specific Energy Absorption: The specific energy absorption (SEA) is the most important factor in design of the parts by considering minimum weight objectives.

The SEA is the energy absorbed per unit mass of the specimen and the SI unit of the SEA is kJ/kg. It can be calculated as follows

$$SEA = \frac{\int p_i ds}{m} \tag{2.10}$$

In next section crashworthiness parameters of thin-walled tube will be calculated by numerical simulation.

2.3 Numerical Simulation of Thin-Walled Tubes with Various Cross-Sectional Shapes

The numerical simulation of thin walled tubes crushing pattern are carried out by using the ABAQUS 6.10. Six thin walled tubes with various cross section are simulated. It is noted that all sample tubes in simulation have been developed with same mass (m≈0.98 kg) and length (L=200 mm). The cross-section configuration of tubes are demonstrated in Figure 2.1.

The crushing thin-walled tube undergoes very complicated strain-stress behavior. During the crush process, material may go into tension, compression and shear. In order to start the first step of deformation the compression load must reaches to the buckling load of tube. The amount of stress and strain due to pure axial compression depend on the configuration of imperfection or trigger mechanism and the effect of dynamic load in term of stress wave propagation. The effects are negligible when a trigger mechanism is used in conjunction with quasi-static loading. In the horizontal hinge lines, the main mechanism of deformation is bending where the material experiences both tension and compression through the wall thickness. Here, it is assumed that the tension and compression stress-strain behaviors of the material are identical and can be taken from the uniaxial tension test.

Experiments prove that in order to achieve the real collapsing shape of tubes under axial loads in numerical simulations, an initial geometric imperfection corresponding to the plastic buckling modes should be introduced on the tube geometry before the impact event. As much as the tubes deformation under axial load will involve buckling, it is necessary to perturb the initial geometry of the tube in the crushing analysis proportional to the buckling modes [81]. By ignoring the geometrical

perturbation, numerical methods only predict the axisymmetric collapsing mode for all case studies because the geometrical model and load condition are both axisymmetric in collapsing of tubes under axial load. However, the experimental tests show that concertina collapsing happens only for a narrow range of tube dimensions. This phenomenon can be explained by considering an instantaneous buckling just before the crushing of tube. The effect of this initial buckling can be introduced in numerical simulation by applying an initial imperfection proportional to the buckling modes on the tube in crushing analysis. In model analysis, in order to obtain a smooth postbuckling response of the deformed tube; the first 10 buckling modes that obtained by running an eigenvalue buckling analysis of the tube using ABAQUS/Standard. Then, the *IMPERFECTION option in ABAQUS/Explicit has been introduced to read the buckling modes, and to perturb the nodal coordinates [82].

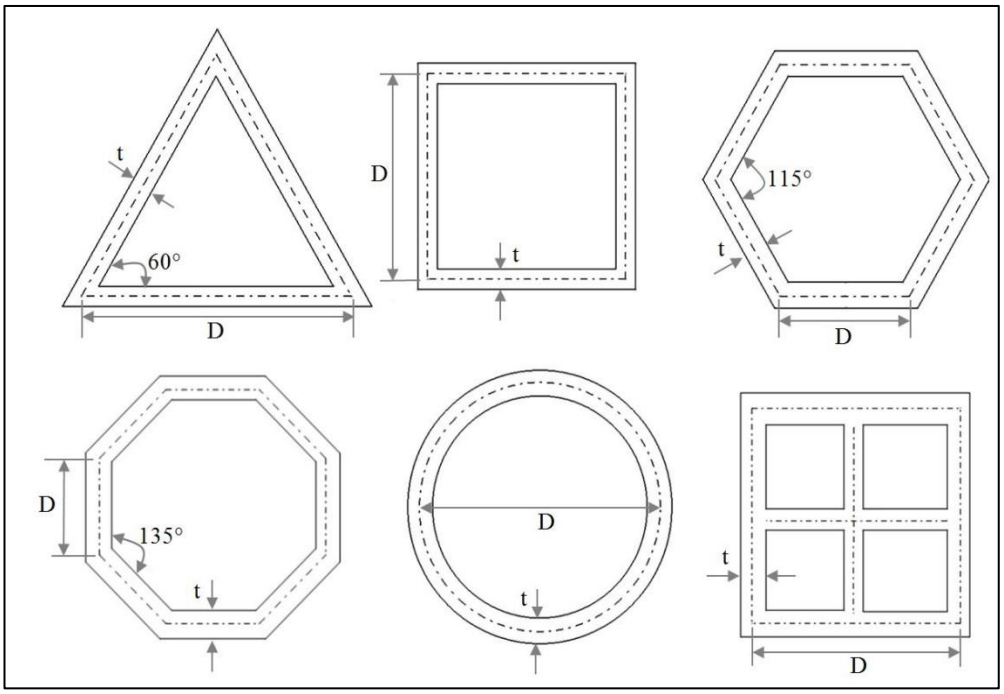

Figure 2.1 : Cross-section of thin-walled tubes.

Thin walled tube crash FE result is so affected by meshing size, therefore different mesh sizes employed to complete the convergence analysis. An element size of 2 mm is found to produce sufficiently accurate results. A mix of quadrilateral and triangular meshes are developed in HyperMesh. The shell element, type of SHELL 4 node with 5 integration points through shell thickness and material model of elastic-plastic is assigned to the tubes. The material of tubes is high strength low alloy steel

(HSLA) 350 with mechanical properties presented in Table 2.1. The stress-strain curve with strain rate 10 s^{-1} is showed in Figure 2.2. The material model of the contact between the tube and the striker is defined as surface interaction with a friction coefficient of 0.2, as well as a self-impact interaction with friction coefficient of 0.2 for inner and our surfaces of the tube is defined. The end of tube is fixed at all DOFs. Rigid wall is used to model the striker which has an initial velocity of 10 m/s and 138.8 kg mass. The load-deflection curve is a useful tool for study the crashing behavior of thin walled tube under impact load. It enables us to determine the mean load, peak load and crush length.

Table 2.1 : Mechanical properties of high strength low alloy steel A 350 [83].

ρ(kg/m^3)	E (GPa)	σ_y(MPa)	σ_u(MPa)	ν	δ_r
7800	210	435	604.6	0.3	0.29

Crashworthiness characteristics of a thin-walled tube are affected not only by cross-sectional shape, solidity and mass but also by striker initial velocity and mass. Therefore in order to assist the effect of cross-sectional shape on crashworthiness characteristic of thin-walled tube, it is necessary that mass and length of tube remain constant in all samples and also the striker mass and initial velocity be identical.

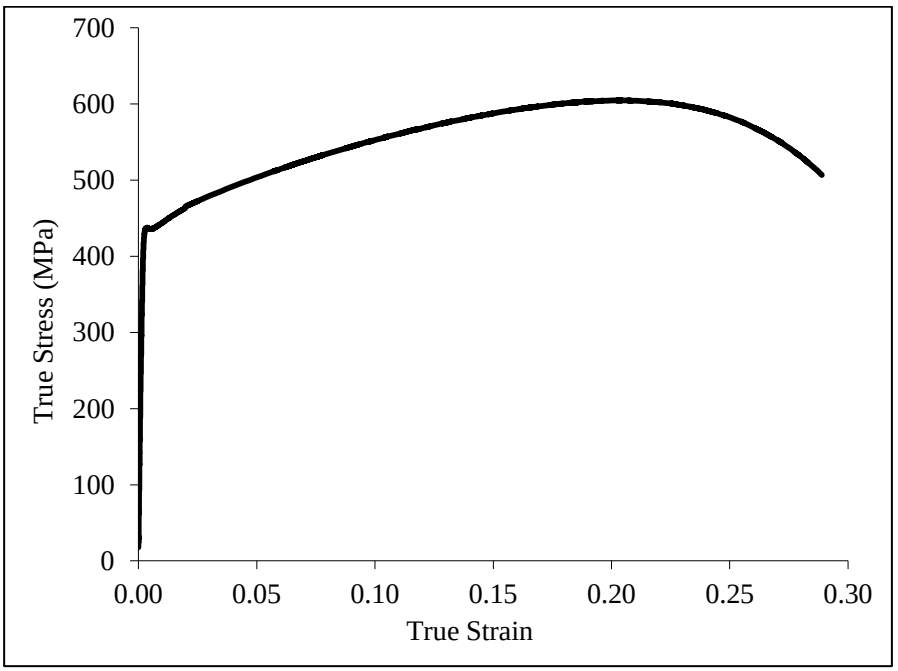

Figure 2.2 : True Stress vs. Strain for HSLA 350 [83].

2.4 Simulation Results of Thin-Walled Tubes with various Cross-Sectional Shapes

In previous comparative studies on various section geometries solidity of tubes were not considered. In this study axial impact simulation on tubes with various cross section geometry has been conducted. The striker mass and velocity is kept same for all tubes. The crashworthiness characteristics of tube have been investigated in different solidity parameter. By keeping the mass and length of tubes fixed and changing the solidity between 0.05 and 0.25 the side size and wall thickness values for all cross-sections have been calculated. The deformation modes and crush load deformation are presented in Figures 2.3 to 2.8. The maximum force, mean force and deformation length are derived from the crash load deformation curves. The geometric specifications of tubes with different cross-sectional shape and FE simulation results are presented in Table 2.2. In order to validate the numerical simulation model, mean crush force F_m derived from the numerical simulation has been compared with the theoretical or empirical equation. That extracted from the experimental results. The comparison results show the good agreement between numerical and theoretical and experimental results.

A typical load-deformation curve for tube with square cross-sectional shape is shown in Figure 2.3, which is for an HSLA tube with $\emptyset=0.15$. The square tube collapse asymmetrically. The axial force reaches an initial peak about 330 kN magnitude, followed by a sharp drop and then fluctuations. These fluctuations are a result of formation of the successive folding. Each subsequent peak corresponds to the onset of a folding process. The energy absorbed is simply the area under this curve. For practical purposes, the average force is often worked out as an indication of energy absorption capacity. A typical view of the crushed square tube is shown in Figure 2.3. The tube wall undergoes sever inward and outward plastic bending, with possible stretching.

Table 2.2 : Specifications of tubes and FE simulation results.

Cross section geometry	*Ø*	*t[mm]*	*D[mm]*	F_m*[kN]*	F_{max}*[kN]*	*δ[mm]*
Triangle	0.05	1.237	169.38	40.436	326.35	119.3
	0.1	1.759	119.10	64.219	326.97	87.8
	0.15	2.167	96.66	83.622	325.37	70.0
	0.2	2.517	83.20	111.227	326.33	61.3
	0.25	2.831	73.97	118.682	327.26	55.7
Square	0.05	1.414	110.22	63.640	324.21	110.5
	0.1	2.026	76.92	102.803	326.85	84.1
	0.15	2.515	61.95	147.19	324.31	66.6
	0.2	2.947	52.88	177.078	326.34	58.8
	0.25	3.345	46.59	197.972	324.73	53.6
Hexagonal	0.05	1.525	68.66	66.426	323.6	90.9
	0.1	2.185	47.92	123.148	326.73	59.4
	0.15	2.714	38.59	159.662	326.97	48.6
	0.2	3.179	32.94	173.176	326.34	44.6
	0.25	3.608	29.02	201.605	329.03	40.6
Octagonal	0.05	1.567	50.12	77.369	321.6	78.9
	0.1	2.258	34.78	125.363	326.9	58.4
	0.15	2.823	27.82	161.628	326.58	47.0
	0.2	3.33	23.59	202.494	326.3	43.6
	0.25	3.809	20.62	222.766	328.81	39.9
Circle	0.05	1.602	124.88	86.903	328.77	66.5
	0.1	2.295	87.16	157.073	326.97	53.2
	0.15	2.850	70.19	189.179	326.34	44.0
	0.2	3.338	59.91	238.606	327.53	41.0
	0.25	3.789	52.78	276.868	327.35	36.4
Multi-cell	0.05	0.942	111.21	91.348	332.62	61.3
	0.1	1.344	77.91	160.427	328.12	52.5
	0.15	1.661	63.06	209.138	327.81	41.8
	0.2	1.935	53.11	251.036	328.78	38.6
	0.25	2.184	47.95	281.711	331.33	35.1

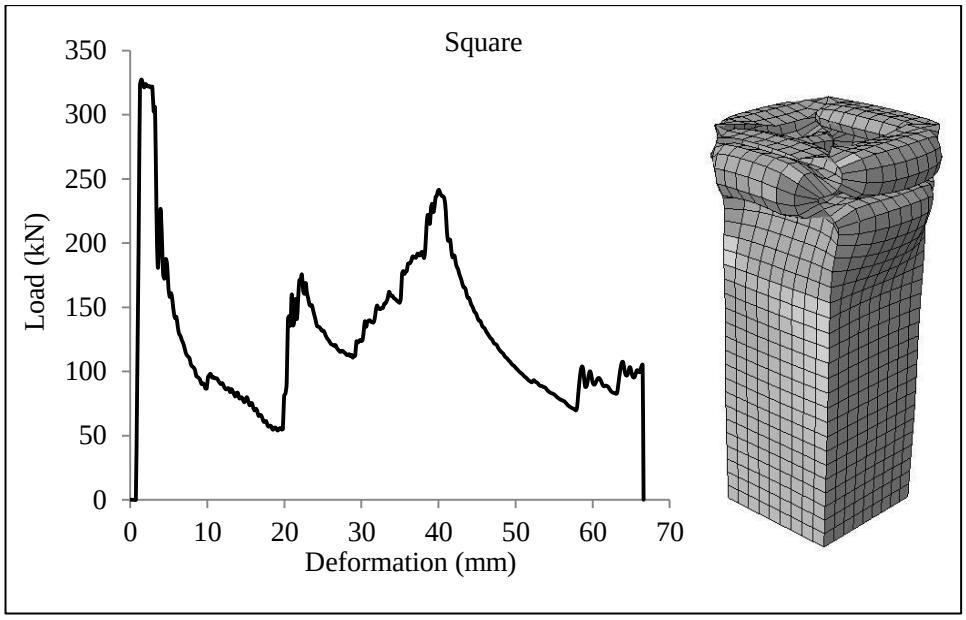

Figure 2.3 : Load-deformation curve for square cross-section, $\emptyset$=0.15.

The collapse mode and the corresponding load-deformation curve of typical triangular tube is shown in Figure 2.4, which is for an HSLA tube with $\emptyset=0.2$. The first fold appeared in the middle of the tube. The axial force reaches an initial peak about 330 kN magnitude, followed by a sharp drop and then smooth fluctuations which are relatively smooth in comparison with other cross-sectional shapes. These fluctuations are a result of formation of the successive folding. Each subsequent peak corresponds to the onset of a folding process.

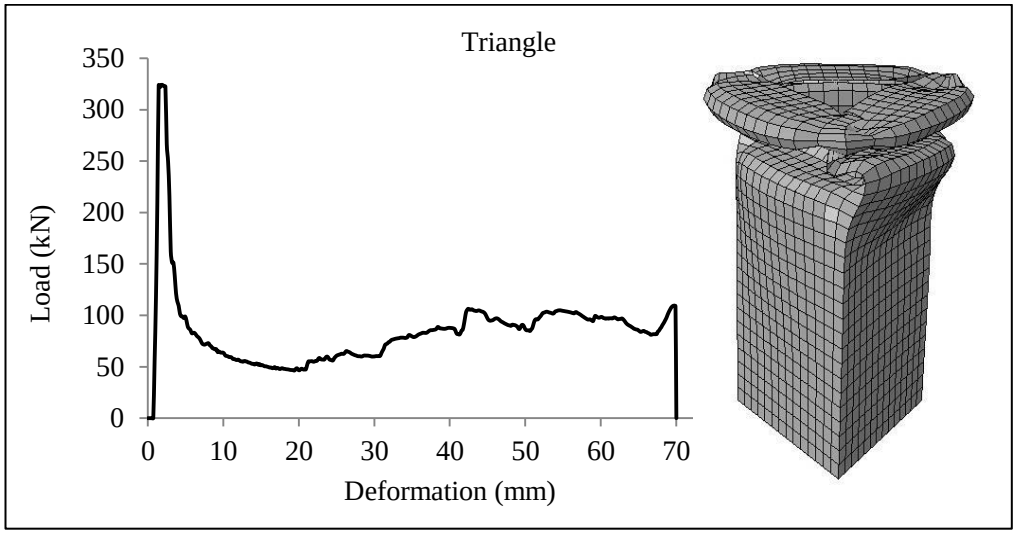

Figure 2.4 : Load-deformation curve for triangular cross-section, $\emptyset$=0.15.

Liu [84] suggested the axial resistance of the thin-walled triangular columns based on the method developed by Abramowicz and Wierzbicki [85], where the axial crushing resistance for a multi-corner thin-walled tube equals to the appropriate

crushing force per one element times the number of corner elements, n. For triangular columns, n=3. The mean crushing force is

$$P_m/M_0 = 39.17\left(\frac{c}{t}\right)^{1/3} \quad \textbf{(2.11)}$$

Where c is the side size of triangle cross-section and t is the thickness of shell.

The plastic deformation mode and impact load-deformation curve for tube with hexagonal cross-section shape are shown in Figure 2.5. The typical deformation mode and curve is for the tube with *Ø=0.15.* The axial force reaches an initial peak about 326 kN magnitude, followed by a sharp drop and then fluctuations.

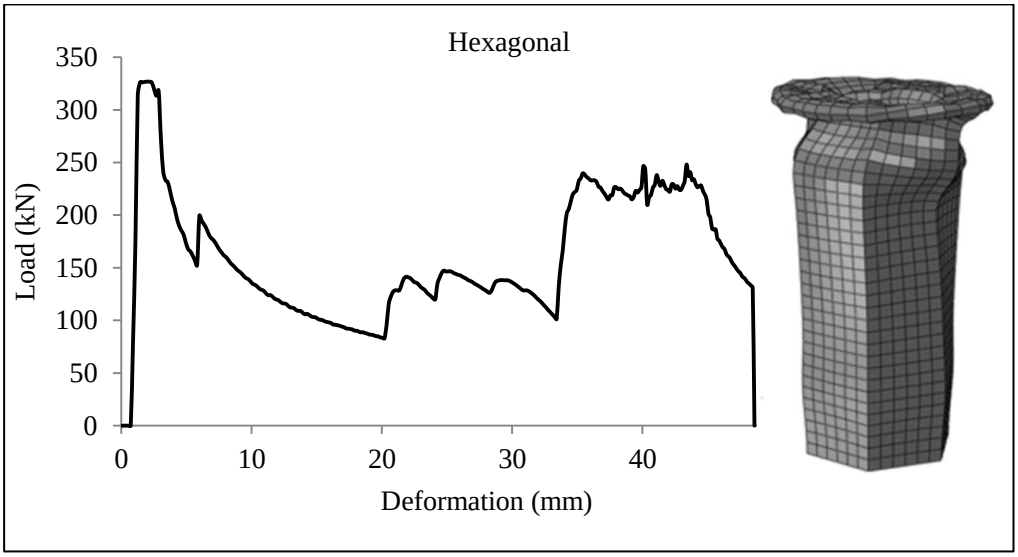

Figure 2.5 : Load-deformation curve for hexagonal cross-section, *Ø*=0.15.

Liu [84] introduced a formula based on the method developed by Abramowicz and Wierzbicki [85] to calculate the axial resistance of the thin-walled octagonal columns. According to the published method, the axial crushing resistance for a multi-corner thin-walled column equals to the appropriate crushing force per one element times the number of corner elements, n. the axial resistance of the steel thin-walled octagonal columns can be approximated by the function

$$P_m = 24.44\ \sigma_0 t^{1.6} C^{0.4} \quad \textbf{(2.12)}$$

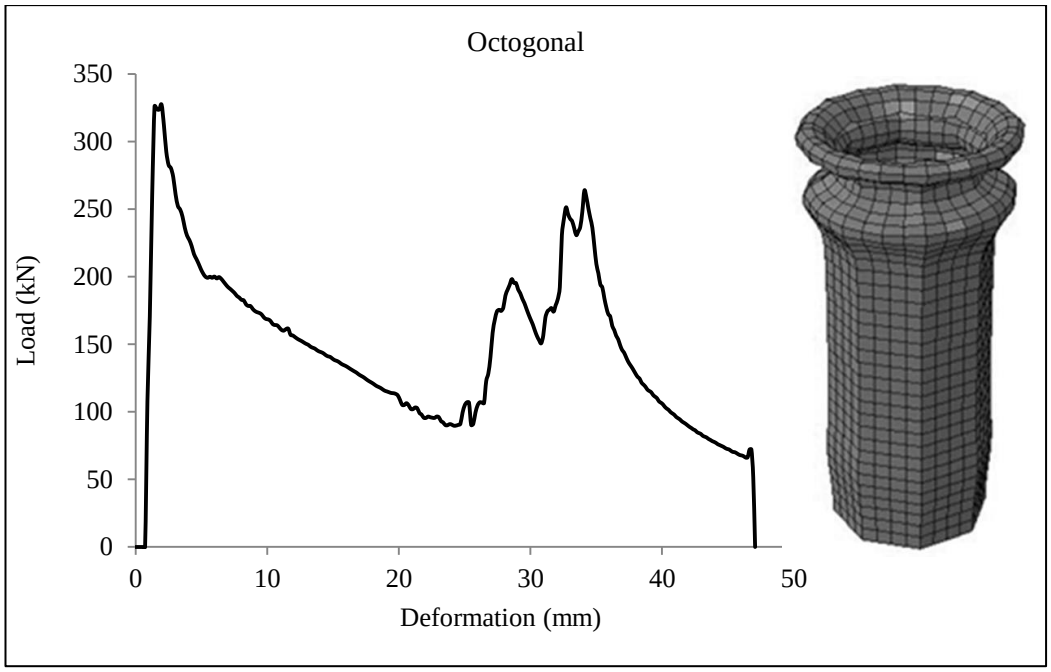

Figure 2.6 : Load-deformation curve for octagonal cross-section, *Ø*=0.15.

Experimental results on axial crushing of circular tubes are extensive. Most of the researchers who proposed theoretical models conducted experiments in an attempt to validate the models. However, the range of D/h used was usually very limited. Lu and Yu [6] by using experimental results on axial crushing of circular tubes, proposed an empirical equation. This equation is based on the results of the research by Guillow et al which conducted for aluminum tubes [6].

$$P_m/M_0 = 72.3\left(\frac{D}{h}\right)^{1/3} \qquad \textbf{(2.13)}$$

where D is the diameter of circular tube and h is the thickness of shell.

Figure 2.7 shows the crushing force and deformation mode of the tube with *Ø=0.2* after the peak load a sharp drop occurred on the tube. Fluctuation of axial crush force show the folding pattern on the crush tube.

Figure 2.8 shows the numerical simulation results for tube with square multi-cell. Square multi-cell tube as shown in Figure 2.8, has a stable deformation mode. As well as in tube with this sectional shape F_m is high in comparison with other cross-section shape. The fluctuation around the mean crush force occur in smooth pattern.

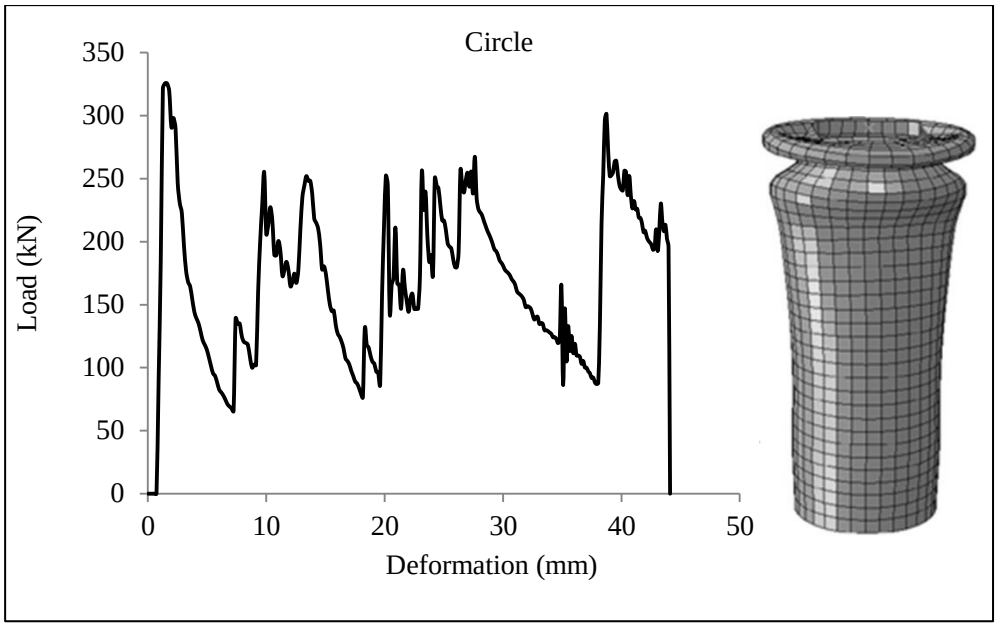

Figure 2.7 : Load-deformation curve for multi-cell cross-sectional , *Ø=0.1*5.

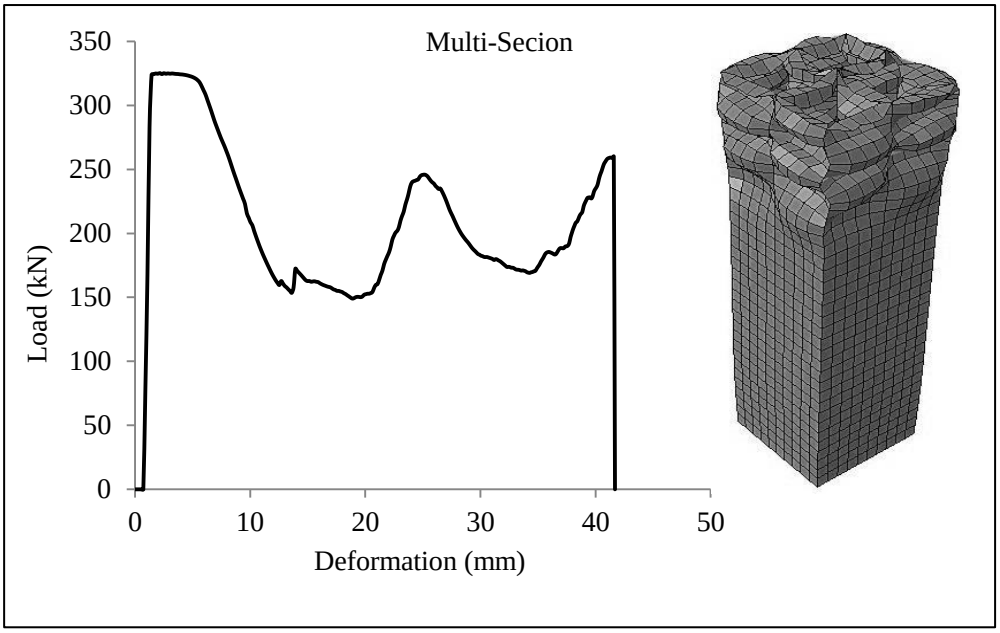

Figure 2.8 : Load-deformation curve for multi-cell cross-section, *Ø=0.1*5.

2.5 Solidity Effects on Crashworthiness Characteristics of Thin-Walled Tubes

In Table 2.2 values of the solidity, wall thickness, side size or diameter, average and maximum force and crushing length are listed. The study of simulation results reveals that the average crush force of tube increase with an increase in solidity parameter in all tubes. But the maximum force is invariant with cross-section geometry and solidity and equals to 326 ± 6 kN for all tubes. This is in agreement

with the quasi-static experimental result of [39], which showed for tubes with same perimeter the maximum force is 34 ± 2 kN. It can be get result that first maximum force is affected by cross-section area of tube and is independent from geometry and solidity of tube.

The crush force efficiency for different cross-sectional shapes is obtained by Eq. 2.2 and F_m, F_{max} values which are listed in Table 3. In order to compare the CEF for different shapes, the variation of CEF are plotted in Figure 2.10 with respect to solidity parameters. These results reveals that CFE increases significantly with an increase in the solidity parameter for all cross-section geometries. The circular tube and multi-cell with Ø=0.05and 0.1 have the highest CFE. The multi-cell with solidity higher than 0.1 has the highest CFE and triangular tube has the lowest CFE.

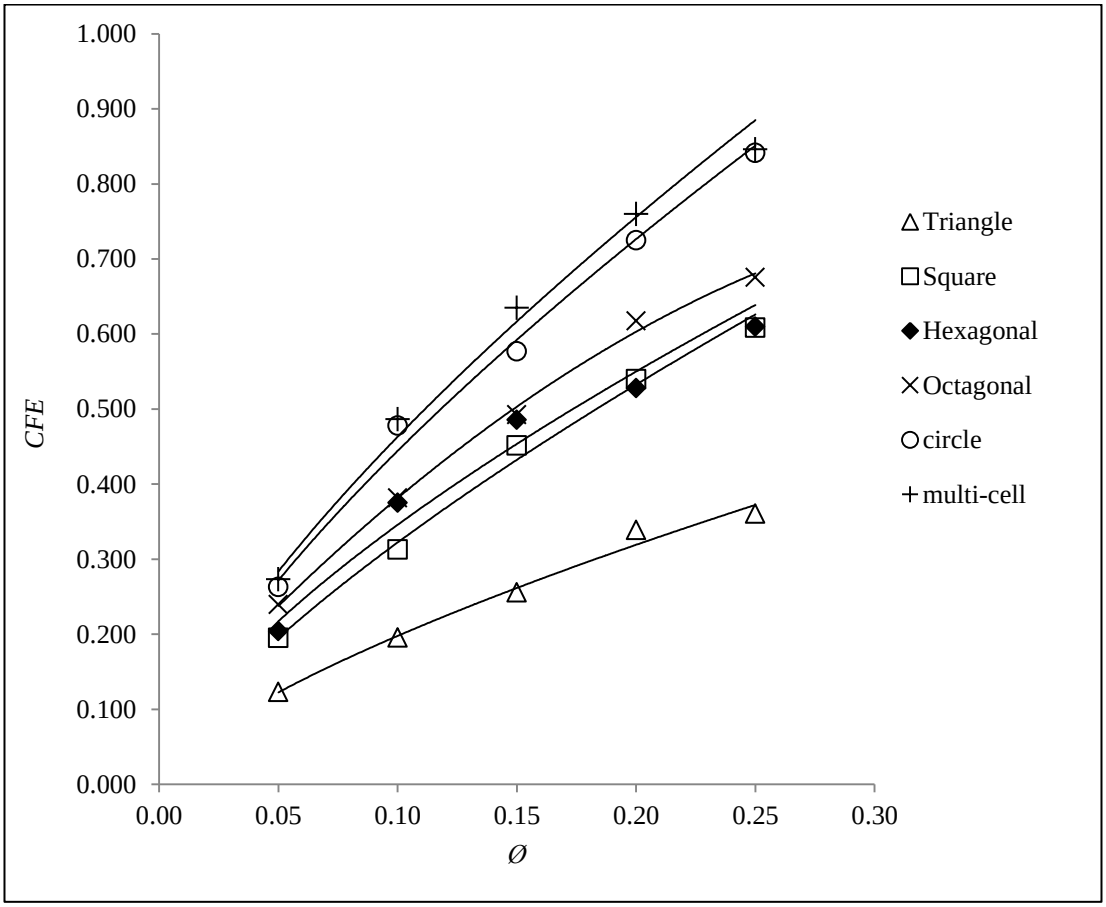

Figure 2.9 : Variations of CFE with solidity for various cross-sectional shapes.

The crush strain for various cross-sectional shapes is obtained by Eq. 2.3 and crush length values, which are listed in Table 2.2. The crush strain values reduce significantly with an increase in the solidity for all cross-section geometries as shown in Figure 2.11. The triangular tube has the highest crush strain value.

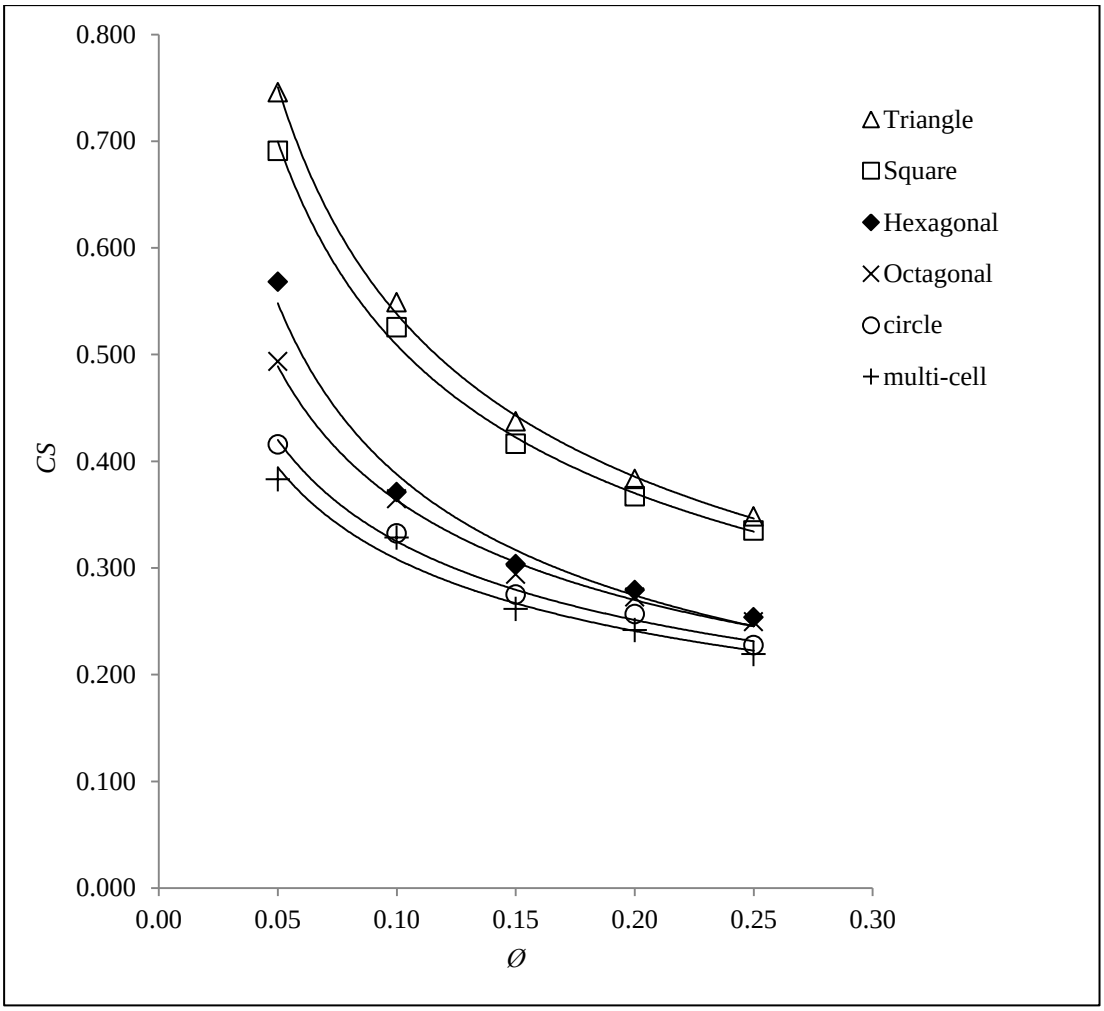

Figure 2.10 : Variations of the CS with solidity for various cross-sectional shapes.

Total efficiency is obtained by multiplication of crush force efficiency and crush strain values for each cross-sectional shape. The plotted result in Figure 2.12 presents the variations of the total efficiency with solidity parameter for different cross-sectional shape. The comparison results demonstrate that with Ø=0.1 octagonal cross-section has the highest and multi-cell has lowest TE. TE reduces slightly with an increase in solidity for all tubes exceptional of square. for Ø≥ 0.3, TE of square shape remains unchanged.

Structural effectiveness parameter (η) is another factor that is obtained to compare the crashworthiness characteristic of different cross-sectional shapes. Structural effectiveness is calculated by usage Eq. 2.6, and P_m which is listed in Table 2.2. A and σ_0 remain constant for all tubes.

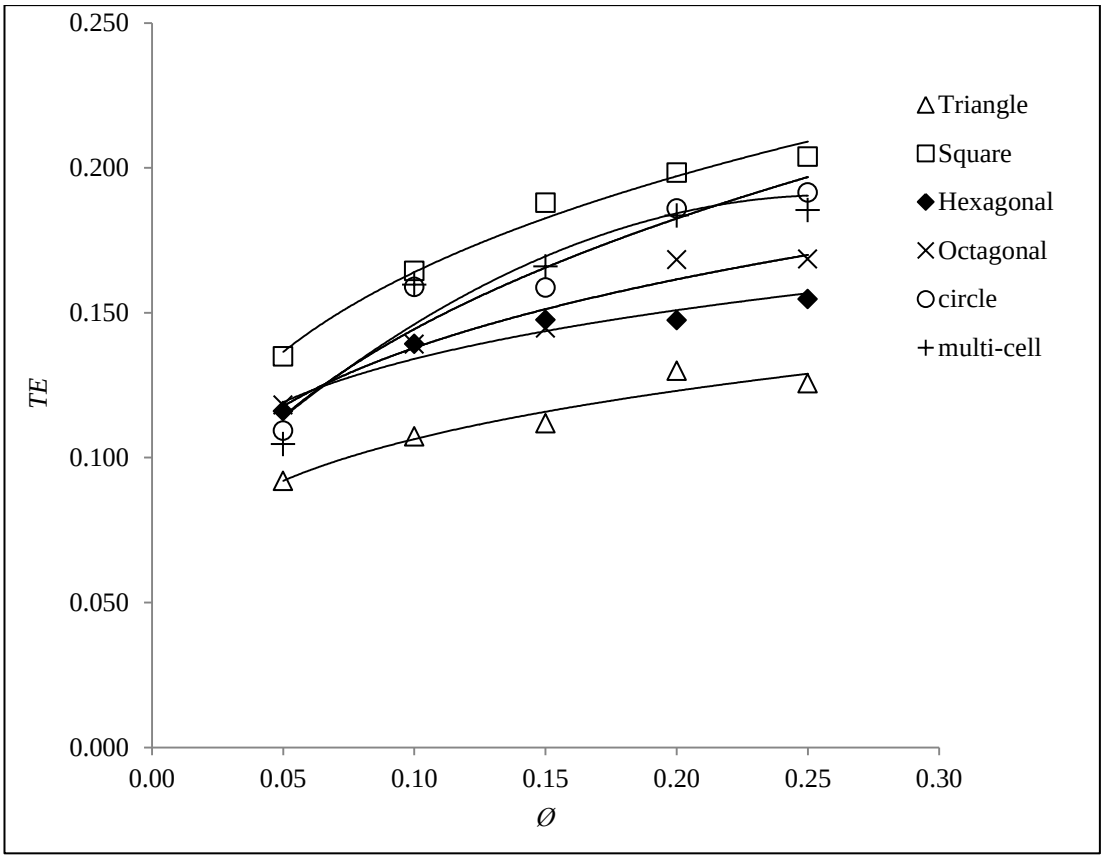

Figure 2.11 : Variations of TE with solidity for various cross-sectional shapes.

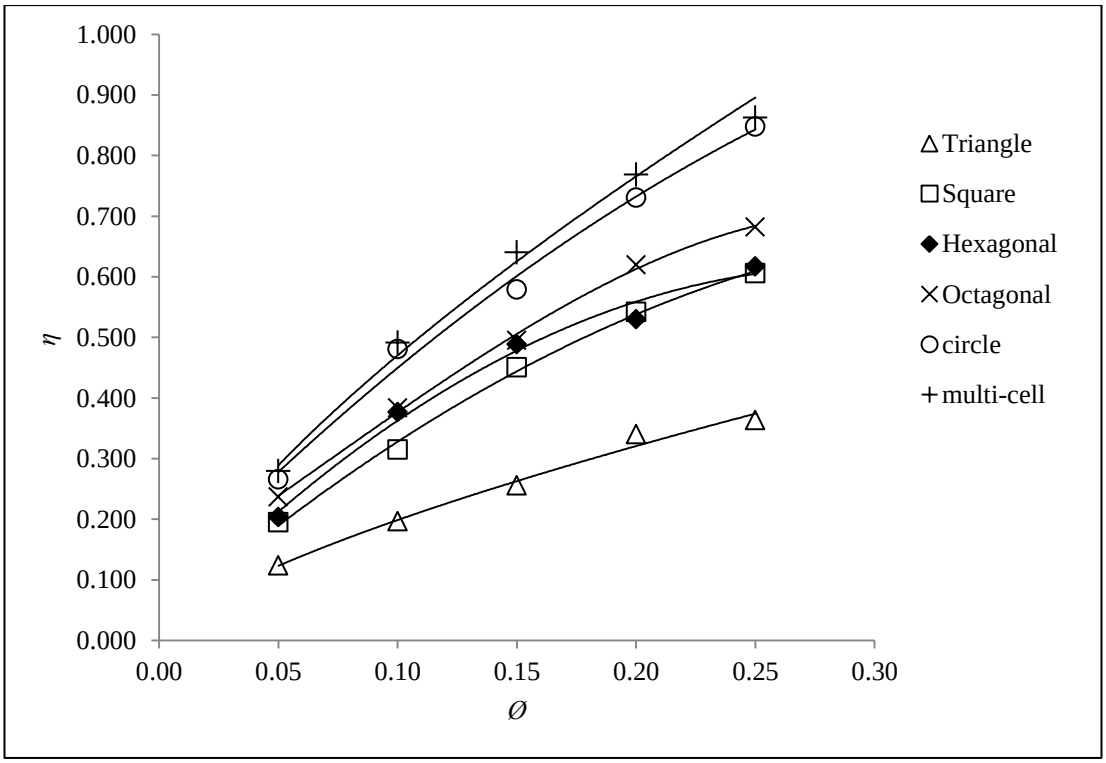

Figure 2.12 : Variations of η with solidity for various cross-sectional shapes.

Figure 2.14 presents the variation of dynamic energy-absorbing effectiveness factor ψ with $Ø$ parameter for various cross-sectional shapes. ψ is calculated by Eq. 2.8. It should be noted that G, V_0 , A and material remain unchanged, therefore variation of ψ is resulted by changing crushing distance as listed in Table 2.2. It is observed that cross-sectional shape and solidity have significant effect on ψ. It is indicated in Figure 2.13 that for $Ø$=0.05, ψ increases from 0.44 to 0.90 and multi-cell and triangular shapes have the highest and lowest value, respectively. For $0.15 \leq Ø \leq 0.25$, multi-cell (Figure 2.1 e) has the highest ψ value and triangular shape has the lowest value as shown in Figure 2.13. It is clear that when all parameters remain unchanged an increase in $Ø$ cause the increase of ψ for all shapes. It is remarkable to note that by an increase of $Ø$ for $Ø \geq 0.15$ the increasing intensity of ψ decrease slightly.

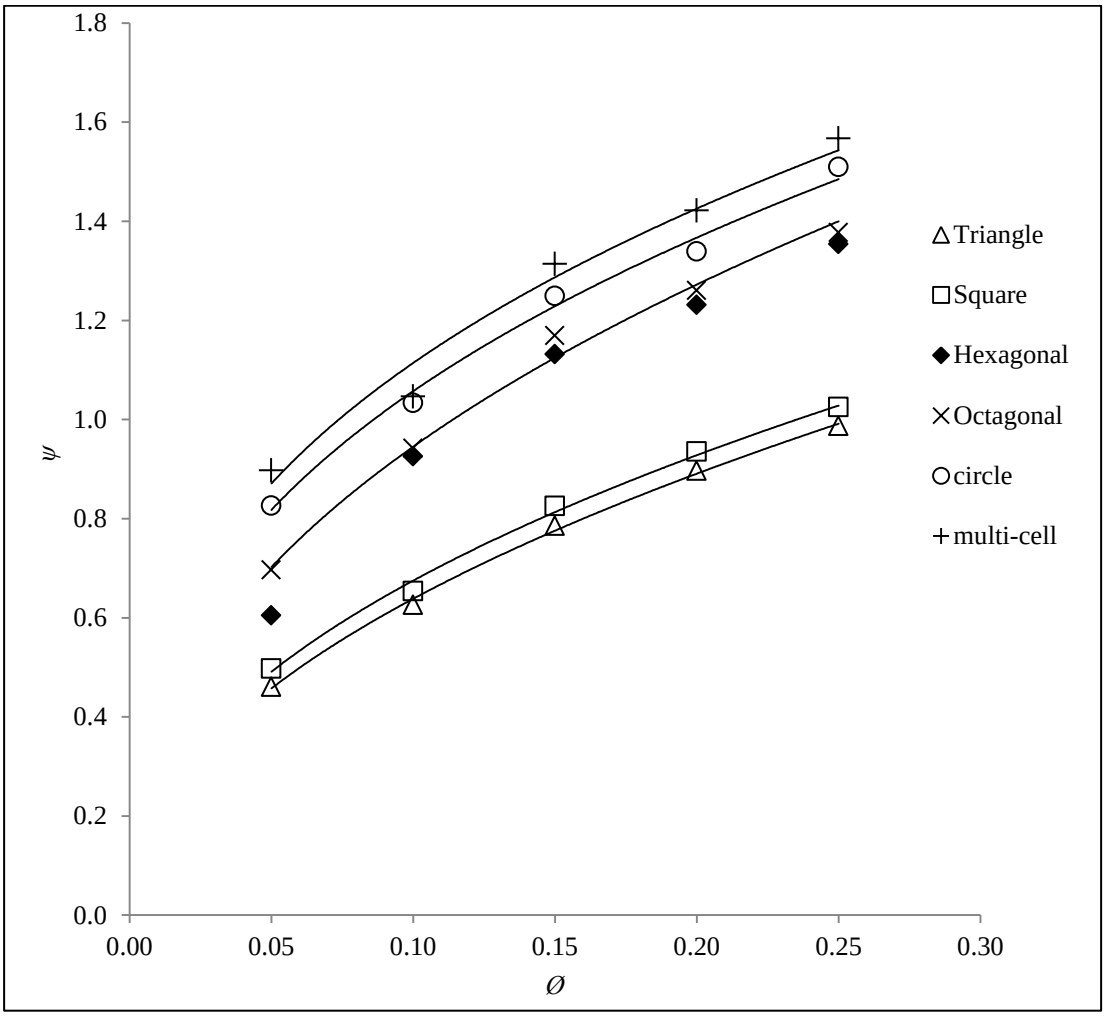

Figure 2.13 : Variations of ψ with solidity for variuos cross-sectional shapes.

In this chapter the crushing behavior of thin-walled tube under dynamic impact loading and crashworthiness characteristics of thin-walled tubes was determined. In

order to obtain the cross-section shape with high crashworthiness features, we investigated the influence of cross-sectional shape and solidity Ø, on crashworthiness characteristics of thin-walled tubes. For this purpose, numerical modeling was conducted for tubes with triangular, square, circular, hexagonal, octagonal, multi-cell cross-sectional shapes. The tubes had the same mass and length and crashworthiness performance comparison was carried out in identical solidity. The crush force efficiency (CFE) , crush strain (CS), total efficiency (TE) , structural efficiency (η) , dynamic energy absorbing effectiveness (ψ) parameters are obtained for tubes with respect to solidity parameter. The FE simulation result reveals that multi-cell cross-section is effective in increasing energy absorbing factor. But in order to achieve optimum design the cell number and configuration should be investigated. The comparison results indicate that the square tube with high total efficiency, stable deformation and reasonable energy absorption capacity is the favorable cross section geometry as energy absorption elements in crush zone system. The finding of this chapter will be used to design of primary energy absorber component in crush zone. In the next chapter with attention to that tubes with square cross-section has the high crashworthiness features by using RSM method optimization will be conducted. The variable of optimization problem are the thickness and the conical angle of tube with square cross-section shape. The objective function is total crashworthiness efficiency.

3. HONEYCOMB STRUCTURES: TEST AND NUMERICAL SIMULATION

3.1 Objectives

Honeycomb structures absorb energy by crushing with relatively fixed mean load. This characteristic has proven to be one of the most reliable and efficient methods of providing G limit protection. In order to achieve low acceleration rate when crush happens on passenger car, in suggested CEM system in this study the honeycomb structures are being used. In this chapter, crashworthiness characteristics of Aluminum hexagonal honeycomb structures under impact load are investigated numerically and experimentally. By changing the wall thickness, cell specifications and impacting velocity, dynamic behavior and crashworthiness parameters of honeycomb are extracted. Explicit nonlinear finite element method is used to simulate the dynamic behavior of honeycomb under out-of-plane impact. Numerical results are compared with experimental results. Under the light of numerical and experimental result, the best cell specification for hexagonal honeycomb structures for crashworthiness applications is presented.

Although computational and experimental analyses of honeycomb structures are investigated by many researchers in literature, crashworthiness characteristic and associated parameters are not studied. Motivated by this fact, this study is undertaken to examine crashworthiness parameters and energy absorption characteristics of honeycomb structures. The finding of this chapter will be used to design the honeycomb structure of crush zone system with optimum crashworthiness characteristics.

3.2 Honeycomb Structures Test

An experimental investigation on aluminum hexagonal honeycomb structures subjected to low velocity impact loading (i.e., velocities smaller than 20 m/s) is conducted. The dimension of test specimens used in the experiments has the height of 20 mm, square cross section of 30×30 mm, foil thickness of 0.025 mm and cell size of 3.175 mm. The geometric configuration of a cell and sample honeycomb

structure is shown in Figure 3.1. The honeycomb cores used in tests are known as 1/8-5052-4.5 which was produced by the company HexWeb. The material of foil is an aluminum alloy labeled as A5052. The MTS universal testing machine is used for the tests as shown in Figure 3.2. The crushing test is implemented by 0.1 mm/s striking speed in T-direction (i.e., see Figure 3.3c). The measured data are the compressive force and stroke during the tests.

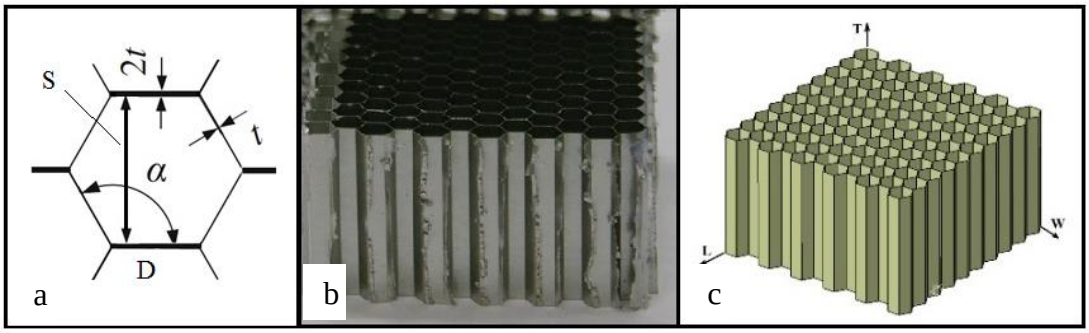

Figure 3.1 : (a) Geometric configuration, (b) a sample honeycomb (c) numerical model of honeycomb structure.

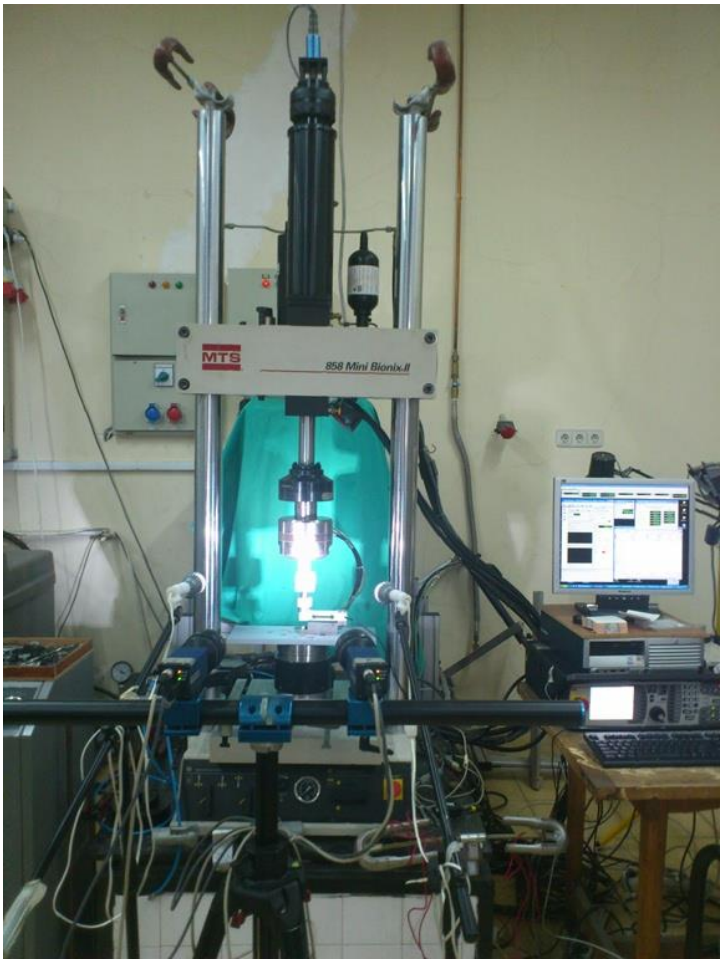

Figure 3.2 : MTS machine used for honeycomb structure in and out-of-plane test.

Figure 3.3 shows the deformed honeycomb structure and progressive folding deformation pattern. It is observed in Figure 3.3c that out-of-plane crushing mode (i.e., in T-direction) is a regular localized folding. In order to obtain stress-strain curves of the honeycomb structure during crushing, the nominal stress and crushing strain values are calculated by using the measured force and stroke data during experiments. Nominal stress is defined by Eq.(3.1) and crushing strain is defined by Eq.(3.2), where F is the compressive force, A is the gross cross-sectional area of the structure, is the stroke and L_0 is the initial length of the honeycomb structure. Furthermore, the crush strength is determined by averaging the oscillatory stress during cyclic collapse of the cells.

$$\sigma = \frac{F}{A} \tag{3.1}$$

The gross stress-strain curves measured during out-of-plane loading of four specimens are shown in Figure 3.4 where it is observed that the deviation between experimental measurements is very low; therefore, it is concluded that the reliability of experiment results is high.

$$\varepsilon = \frac{\Delta L}{L_0} \tag{3.2}$$

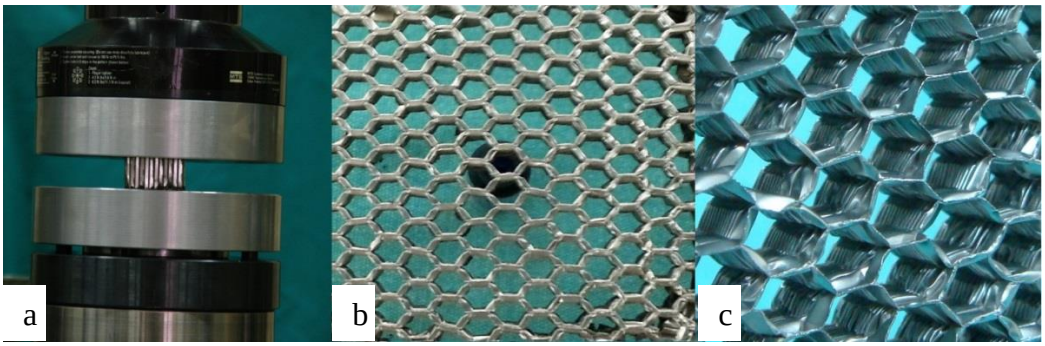

Figure 3.3 : (a) Specimen in MTS, (b) Top view and (c) Enlarged view of the honeycomb after the test.

The average crush strength is determined as 1.76 MPa by using experimental measurements which are shown in Figure 4. In the published data of the honeycomb manufacturer, it is listed as 1.79 MPa. On the other hand, Wierzbicki's theoretical solution for determining the crush strength is given by [86].

$$\sigma_m = 6.63\sigma_0\left(\frac{t}{D}\right)^{5/3} \quad \textbf{(3.3)}$$

where t is the thickness of honeycomb core foil and D is the side size of honeycomb cell as showed in Figure 3.1a. The proof stress of the honeycomb material is about 340 MPa and the crush strength determined by the Wierzbicki's theoretical solution is 1.76 MPa as well. In brief, there is a good agreement between the experimental results and theoretical solution of Wierzbicki [86].

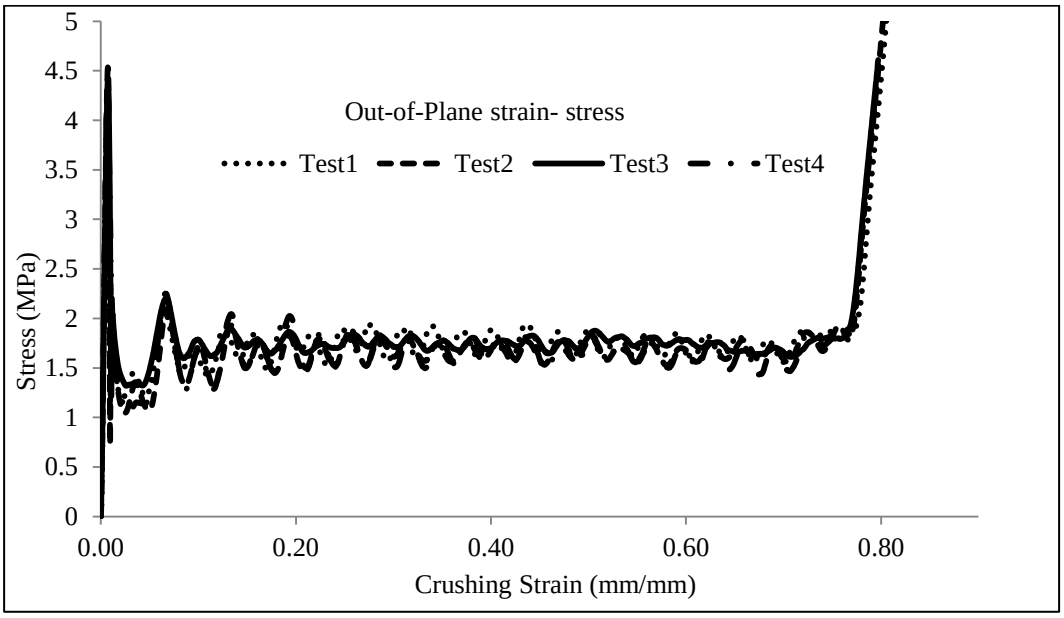

Figure 3.4 : Stress-strain curves of specimens during out-of-plane crushing.

3.3 Description of the FE Model

To generate the FE model, the geometrical model was drawn by using Catia R.19 and meshed by using the software HyperMesh; then, the FE mesh was imported to HyperCrash to set the material properties, element features and boundary conditions. The numerical solutions are obtained out by using the RADIOSS solver. HyperView and HyperGraph softwares are used for visualization of the results. The honeycomb structures used in numerical simulations are modeled by using the SHELL 4N element type in HyperCrash. The convergence analyses has been done to find the optimum mesh size by employing FE models having different mesh sizes. An element size of 1 mm is found to produce sufficiently accurate stress results.

For experimental studies, adjacent sides of aluminum honeycomb structures are glued together during fabrication. In parallel, to simulate the adhesive bonding

between the adjacent sides, a tied contact interface is defined between the adjoining elements and nodes in the FE model. In order to compare the FE solutions with experimental measurements, the geometry of the FE model is selected the same as the geometry of experimental specimen. Figure 3.5 shows the mesh and geometry used in the FE model. The nodes on the base of the FE models are fully fixed and self-contact between the walls of honeycomb cells are defined. Dynamic loading is simulated by modeling a moving rigid wall with a specified mass and initial velocity. The aluminum alloy of A5052 with elastic-plastic material model having density of 2860 kg/m^3, yield stress of 340 MPa, Young modulus of 75 GPa, Poisson ratio of 0.33 and rupture strain of 0.12 is used in FE analyses.

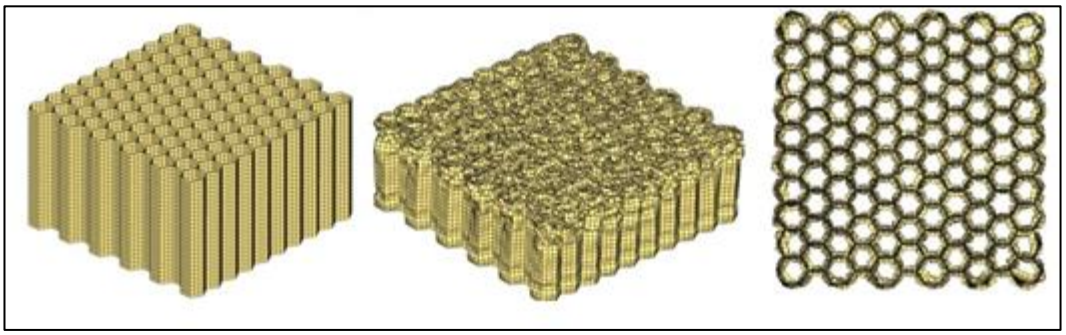

Figure 3.5 : The FE model with S= 3.175 mm, t= 0.025 mm with 0.1 mm/s impact.

To ensure that the FE model is reliable, the numerical results are compared with experimental measurements. Figure 3.6 shows the crushing strain-stress curves of the FE solutions and experimental measurements. The stress-strain curve of crushing process is a useful tool to evaluate the crashworthiness and crushing behavior of a thin walled structure which gives the crush strength, mean crush stress and crushing length of the structure. In a typical stress-strain curve during crushing (e. g., see Figure 3.6), it is observed that initially the structure behaves elastically and the load increases in a steady manner, then an initial peak stress (called the crush strength) occurs that is followed by a rapid decrease in stress values. Thereafter, the postbuckling phase develops with secondary peaks which are directly related to the formation of subsequent local buckling occurrences in honeycomb structures as the crushing progresses. The subsequent peaks in stress history have significantly lower magnitudes in comparison with the initial peak. It is observed that there is a good agreement between the FE solutions and experimental measurements.

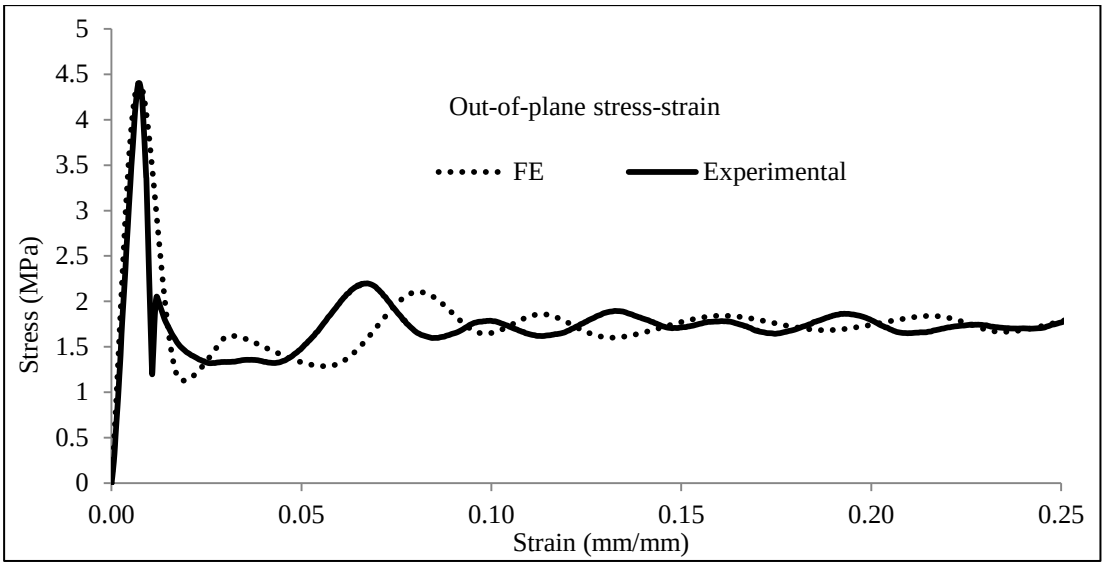

Figure 3.6 : Numerical and experimental stress-strain results.

3.4 Effect of Cell Expanding Angle on Crashworthiness Parameters

In order to study the expanding angle α effect on crashworthiness parameters of honeycomb structures, crushing of honeycomb structures is simulated by changing the expanding angle α between 90º and 150º. Figure 3.7 shows the impact load-deformation curves for the honeycomb structure with expanding angle α between 90º and 150º. Note that load-deformation curves are useful tool to determine the crashworthiness parameters. Figures 3.8, 3.9 and 3.10 show the crashworthiness parameters as the cell expanding angle α changes. By analyzing the load-deformation curves, in Figure 3.6, it is concluded that after the linear-elastic response of the structure, the cells buckle elastically or bend plastically; thus, a non-linear behavior develops.

Figure 3.8 and 3.9 show the collapse stress and crush force efficiency-cell expanding angle variation, respectively. It is observed that the cell configuration having the expanding angle α equals to 120º has the maximum collapse stress and crush force efficiency. For other values of α, these parameters are smaller. Based on the buckling failure mechanism, normal collapse stress of the honeycomb in the out-of-plane direction σ is expressed as follows [56].

$$\sigma = 4.26\cos^2(\alpha - \pi/2)\left[1+\sin(\alpha - \pi/2)\right]^2 E_s\left(\frac{\rho}{\rho_s}\right)^3 \qquad \textbf{(3.4)}$$

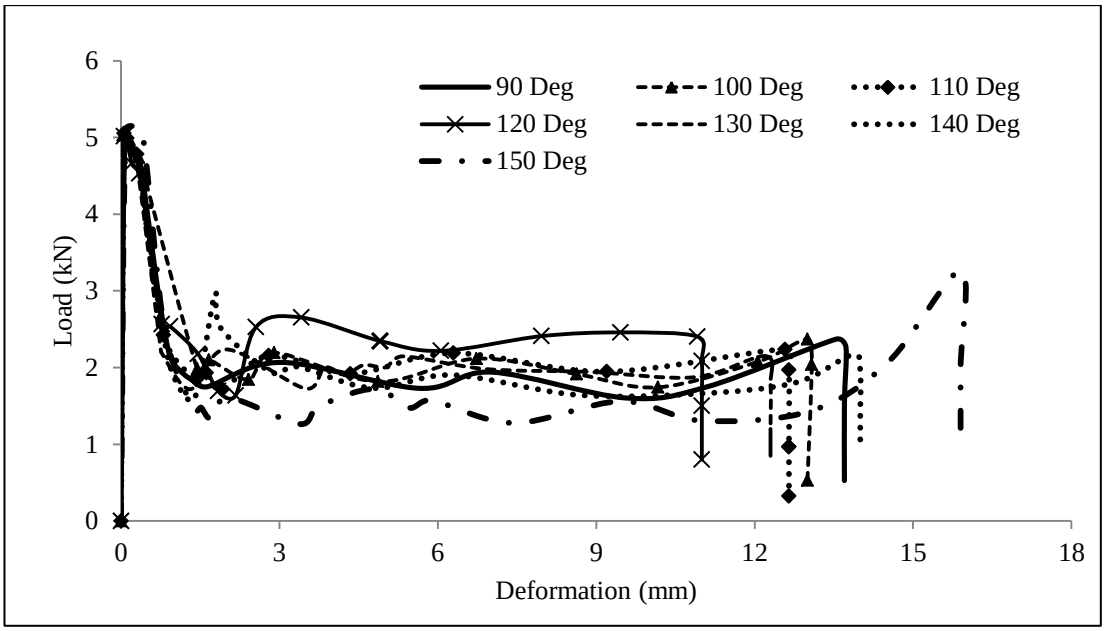

Figure 3.7 : Impact load-deformation curves as cell expanding angle α changes where v= 14 m/s and m= 0.21 kg, cell number 60.

where E_s is the Young's modulus of the solid cell wall material, ρ is the density of the honeycomb and ρ_s is the density of the solid cell wall material. According to the analytical solutions, normal collapse stress has the maximum value in expanding angle α equals to 120º as well. There is a direct relationship between normal collapse stress and crashworthiness parameters. By comparisons, it is observed that there is a good agreement between the trend of analytical calculations and numerical results both of which have the maximum value for α =120º.

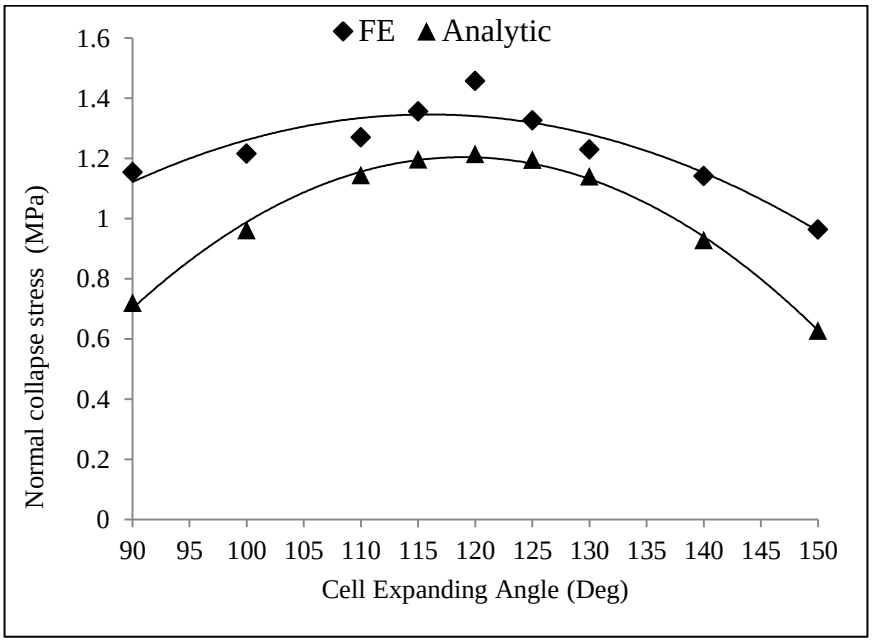

Figure 3.8 : Variation of normal collapse stress vs cell expanding angle.

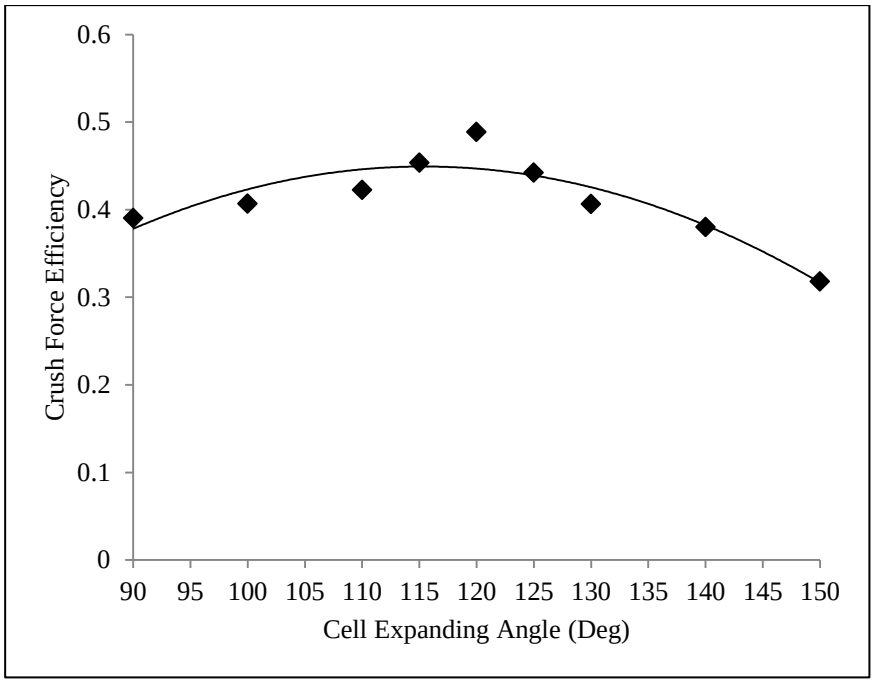

Figure 3.9 : Variation of crush force efficiency as the cell expanding angle changes.

Figure 3.10 shows the total energy absorption-cell expanding angle variation. It is observed that the model having the expanding angle α of 120º yields the largest total energy absorption as well.

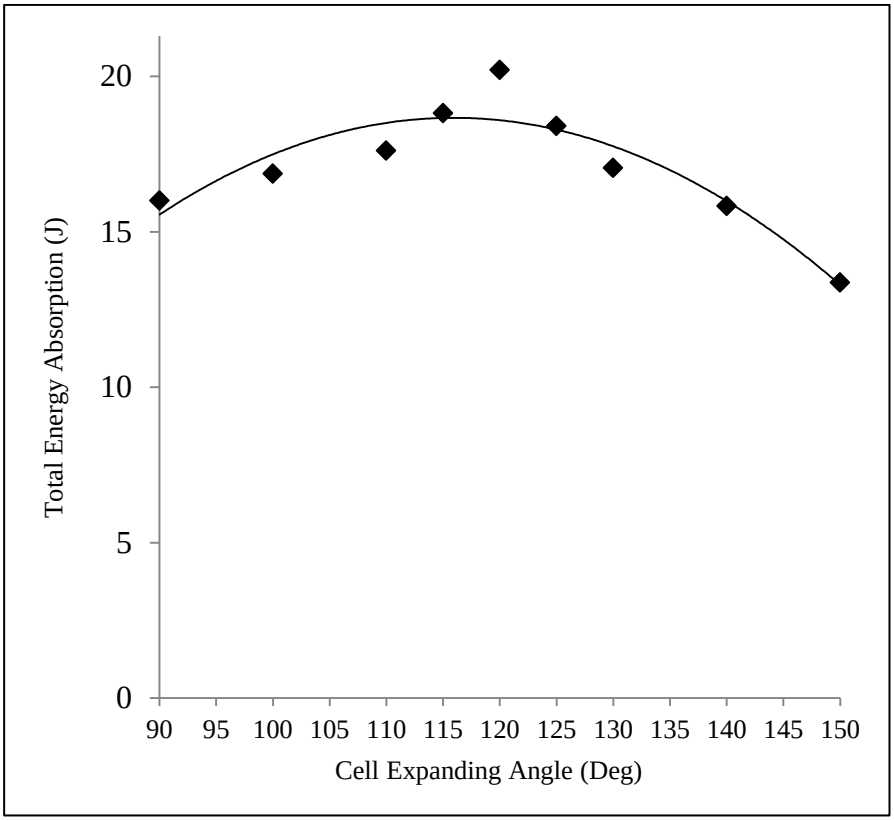

Figure 3.10 : Variation of total energy absorption vs cell expanding angle.

Figure 3.11 shows the variation of energy absorber effectiveness factor as the cell expanding angle changes. It is observed that the model having the expanding angle α of 120º yields the largest energy absorber effectiveness factor as well.

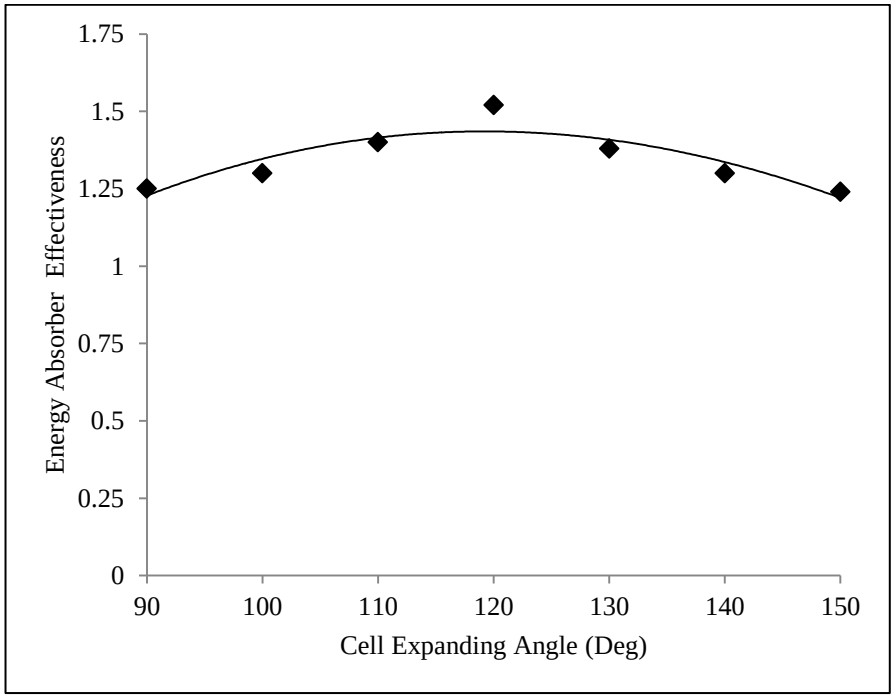

Figure 3.11 : Variation of crush force efficiency as the cell expanding angle change.

In sum, the honeycomb structure having α =120º has the optimum strength and energy absorption since it results in identical buckling strength in the L- and W-directions denoted in Figure 3.3.

3.5 Effect of Foil Thickness and Cell Size on Crashworthiness Parameters

To compare the results of different honeycomb structures on the same ground, a parametric study is conducted to investigate the effects of the foil thickness on crashworthiness properties of honeycomb structures by keeping the total mass of the model constant. By changing the foil thickness between 0.025 mm and 0.0603 mm, the cell sizes and numbers of cells are changed accordingly such that the total mass of the model is kept constant, e.g., see Figure 3.12.

Figures 3.13-3.16 show respectively the impact load-deformation, crush force efficiency, total energy absorption and energy absorber effectiveness factor curves for the honeycomb structure with constant mass, where the thickness changes between 0.025 mm and 0.0435 mm and the cell side size changes between 2 mm and 5 mm when the total mass is constant and impact velocity and mass are 14 m/s and 1

kg, respectively. It is observed in these figures that the honeycomb cores with thin foil thickness and small side size had the larger mean crush force, crush force efficiency, total energy absorption and energy absorber effectiveness factor since these cases correspond to relatively larger numbers of honeycomb cells in the test specimen

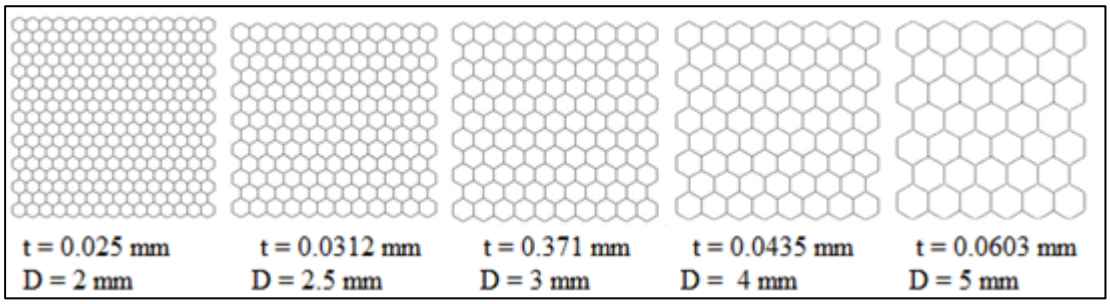

Figure 3.12 : The geometry of honeycomb when mass of the model is constant.

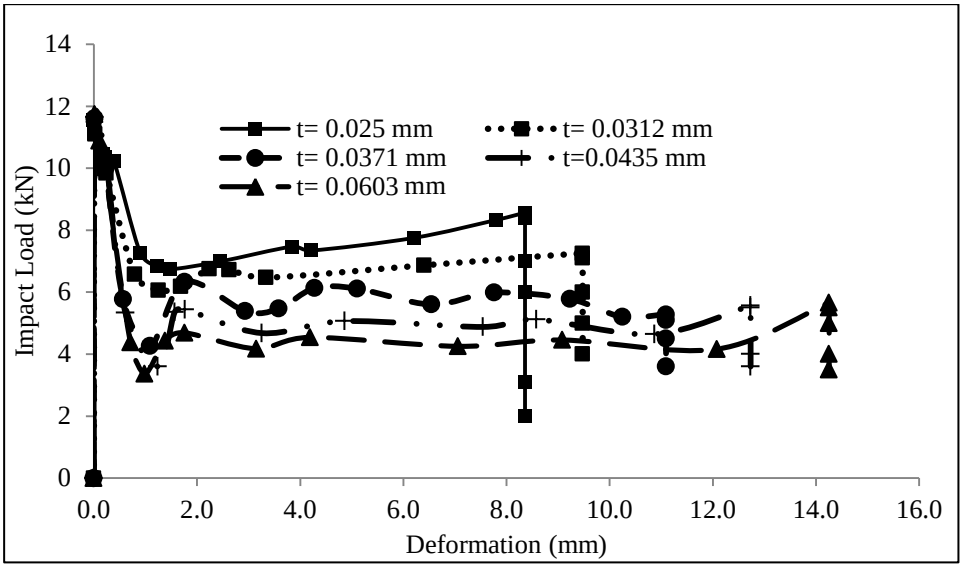

Figure 3.13 : Load-deformation curves for different foil thickness and cell size.

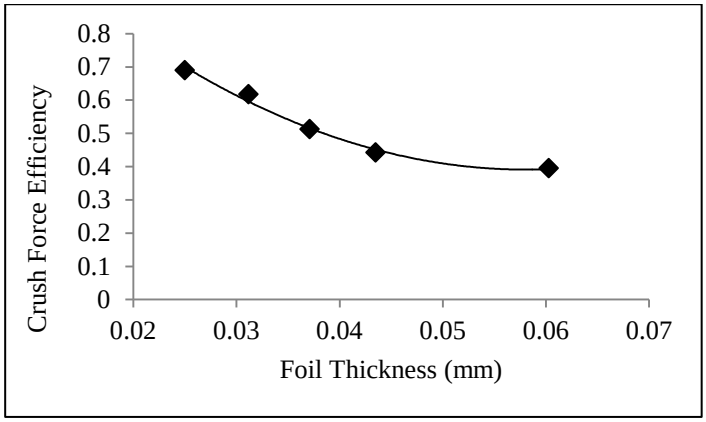

Figure 3.14 : The crush force efficiency-foil thickness curve while the total mass is constant.

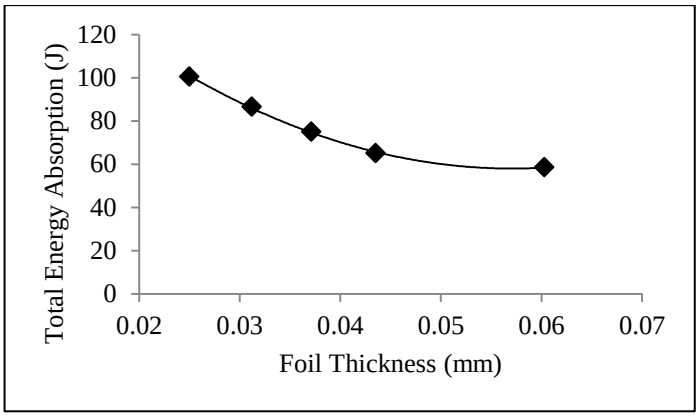

Figure 3.15 : Total energy absorption-foil thickness curve while the total mass is constant.

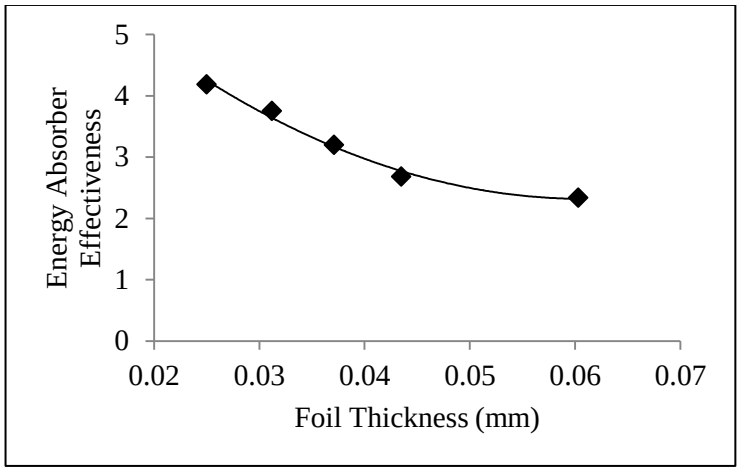

Figure 3.16 : Energy absorber effectiveness factor-foil thickness curve while the total mass is constant.

3.6 Effect of Foil Thickness and Cell Side Size on Crashworthiness Parameters

In order to investigate the effect of foil thickness on crashworthiness parameters, the crush force efficiency, specific energy absorption and energy absorber effectiveness factor curves are shown in Figures 3.17-3.19. The impact velocity, mass and cell number are 14 m/s, 1 kg and 90, respectively. It is observed that by changing the foil thickness between 0.01 mm and 0.05 mm the crashworthiness parameters change slightly.

According to simple compression failure mechanism, the buckling load is determined by the second moment of inertia of the wall and cell side size as follows [56].

$$P_{crit} = K\frac{E_s t^3}{(1-\upsilon^2)l} \qquad \textbf{(3.5)}$$

The constant, K , is an end constraint factor, E_s is the Young's modulus of the solid cell wall material, v is the Poisson's ratio of the solid cell wall material, t is the thickness of honeycomb material and l is the length of cell side. By increasing the foil thickness, critical buckling load increases and lead to larger energy absorption in the specified length of the structure.

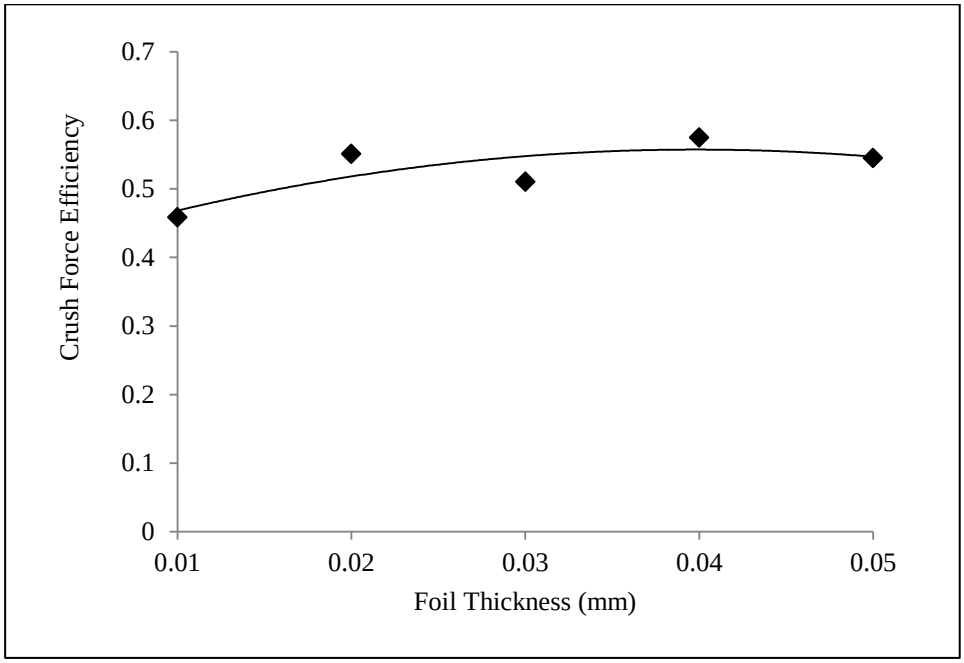

Figure 3.17 : Energy absorber effectiveness -foil thickness curve while the total mass is not constant.

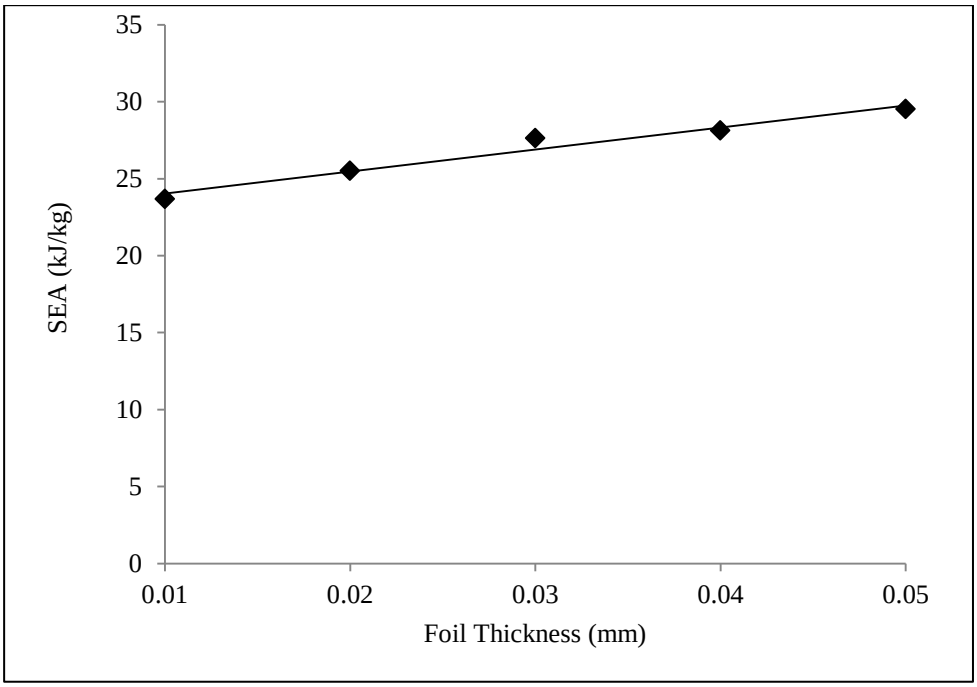

Figure 3.18 : Energy absorber effectiveness factor-foil thickness curve while the total mass is not constant.

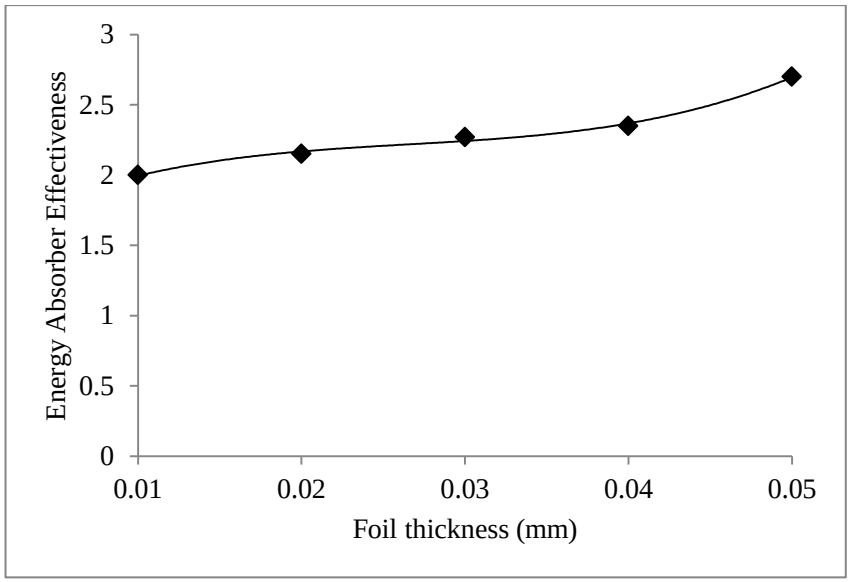

Figure 3.19 : Energy absorber effectiveness factor-foil thickness curve for the constant side size of 3 mm where the total mass is not constant.

In Figures 3.20, 3.21 and 3.22 the crush force efficiency, specific energy absorption parameters and energy absorber effectiveness factor are shown. Where it is clear that crashworthiness parameters are dependent on the cell side size. By changing the cell side size between 2 mm and 5 mm, the crush force efficiency and specific energy absorption decrease significantly and energy absorber effectiveness factor slightly. Based on Eq. (3.5), increasing the cell side size leads to decrease in bucking load. When local buckling of the structure is observed in relatively lower forces values, energy absorption capacity and crush force efficiency of the honeycomb structure decline.

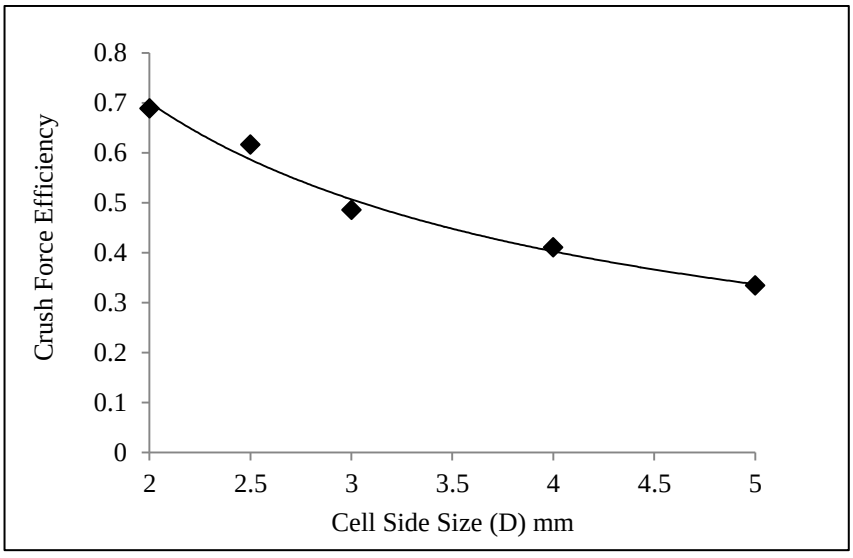

Figure 3.20 : Crush force efficiency-cell side size curve with constant foil thickness of 0.025 mm where the total mass is not constant.

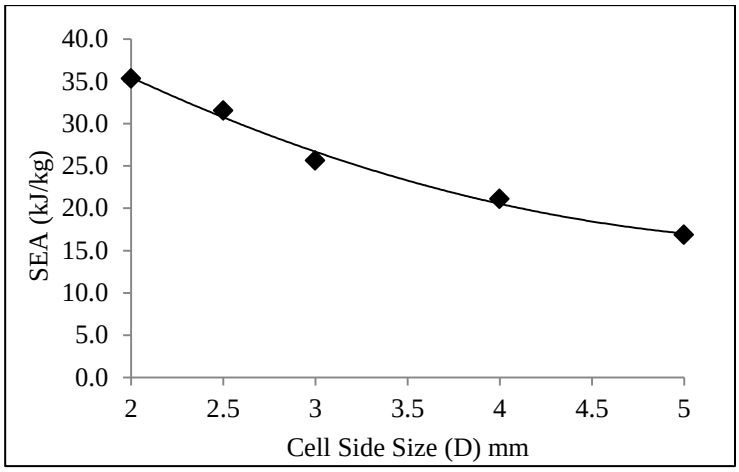

Figure 3.21 : Specific energy absorption-cell side size curve with constant foil thickness of 0.025 mm where the total mass is not constant.

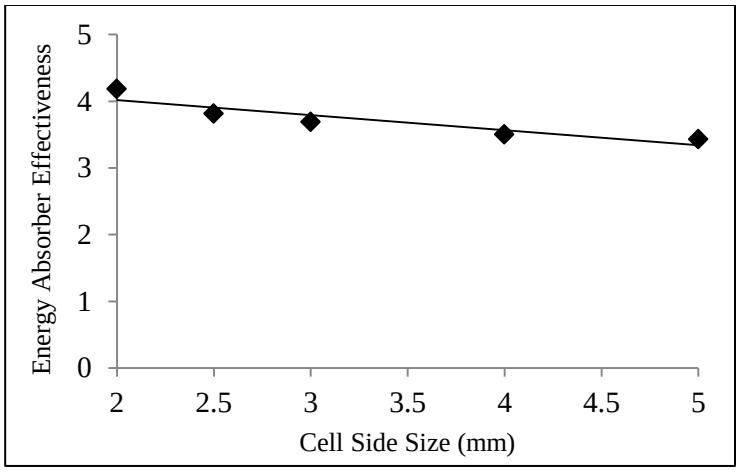

Figure 3.22 : Energy absorber effectiveness-cell side size curve for the constant foil thickness of 0.025 mm where the total mass is not constant.

In parallel to the conclusion in Section 3.4, as the cell side size and foil thickness reduces, relatively larger numbers of cells exist in the structure which result in increments in crashworthiness.

3.7 Effect of Impact Velocity and Mass on Crashworthiness Parameters

It is observed in literature that inertia effects may be influencing the dynamic response and crashworthiness properties In thin walled structures. To investigate this claim, the crushing behavior of a honeycomb structure made of the aluminum alloy of A5052 having the cell size of 3.175 mm and foil thickness of 0.0508 mm is examined for different impact mass and velocity values.

The effect of impact mass on the load-deformation curves is studied for a constant impact velocity of 5 m/s. Figure 3.23 shows the dynamic impact load-deformation

curves where the impact velocity is kept constant, while the impact mass is increasing from 0.6 kg to 4.6 kg. It is clear that the increases in the impact velocity do not significantly influence the characteristics of impact load-deformation curve up to a certain deformation value. On the other hand, higher impact mass results in increasing crushing distance, because the TEA and SEA values given respectively by Eqs. (2.9) and (2.10) increase as the impact mass increases.

Figure 3.24 shows the relationship between the energy absorber effectiveness factor and impact mass. It is observed that an increment in the impact mass causes an increment in the energy absorber effectiveness factor. Although it appears that the characteristics of crushing behavior and non-linear stiffness are independent of the impact mass, it is worth to remark that the energy absorber effectiveness of honeycomb structure is affected by impact mass value.

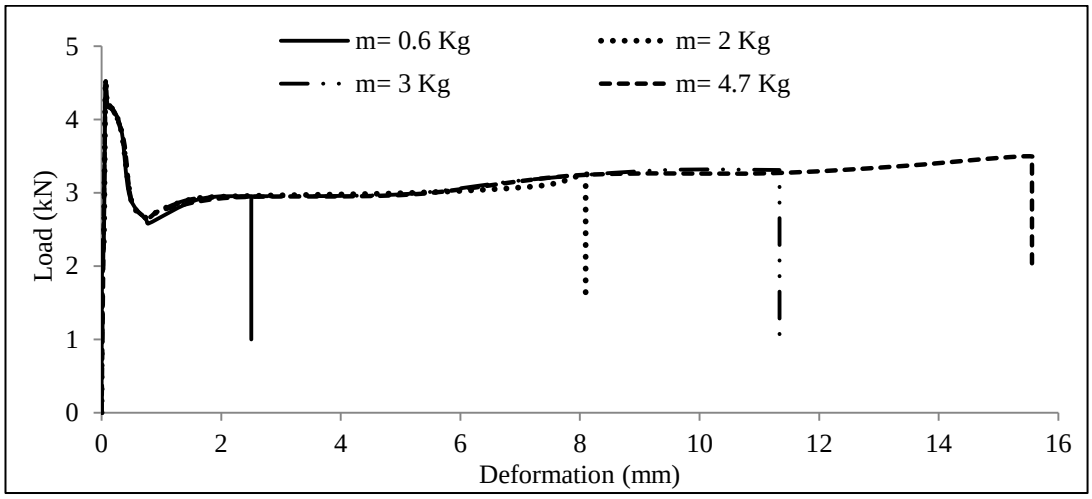

Figure 3.23 : Load-deformation curves for various impact mass values while the impact velocity is 5 m/s, cell number 100.

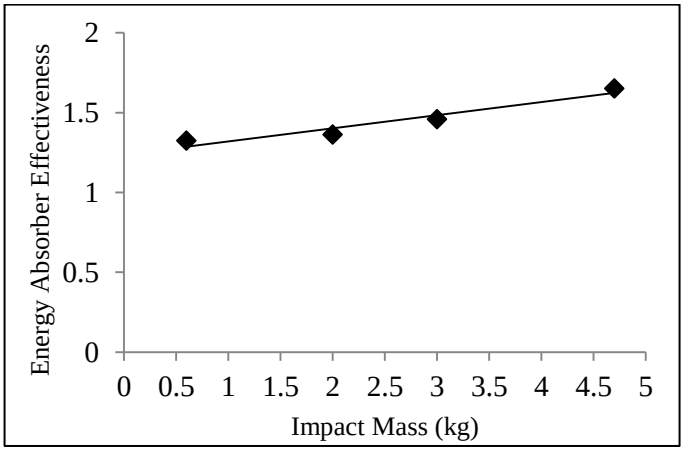

Figure 3.24 : Variation of energy absorber effectiveness factor as impact mass values change for the impact velocity of 5 m/s.

Following, effects of impact velocity on honeycomb crushing behavior and crashworthiness properties are studied for a constant impact mass of 0.6 kg. By changing the initial impact velocity from 5 m/s to 14 m/s, compressive load-deformation curves for all cases are plotted in Figure 3.25. It is observed that crushing strength of the honeycomb structure is almost invariant as the impact velocity increases. On the other hand, higher initial impact velocity results in increasing crushing distance, because the TEA and SEA values given by Eqs. (2.9) and (2.10) respectively, increase as the initial impact velocity increases. This observation is in agreement with the experimental observation that the crushing strength is not affected significantly for impact velocities between 2 to 28 m/s [1]. Figure 3.26 shows the relationship between the energy absorber effectiveness factor and impact velocity, where it is observed that an increment in the impact velocity causes an increment in the energy absorber effectiveness factor. This observation is in agreement with the results reported in [40].

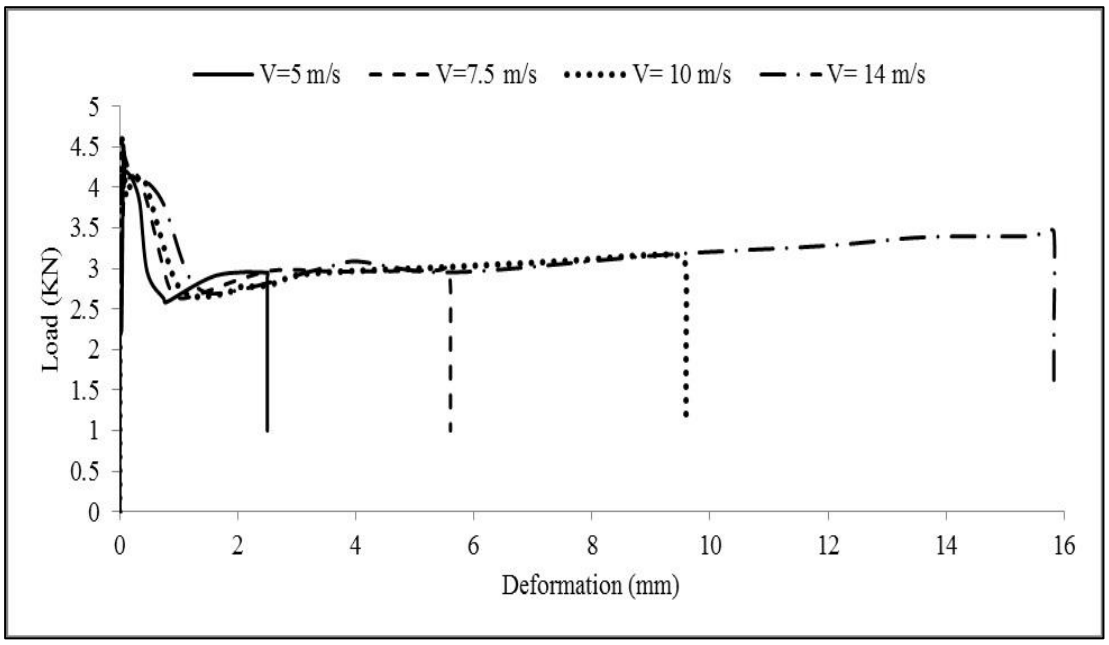

Figure 3.25 : Load-deformation curves for different impact velocities while the impact mass is 0.6 kg, cell number 100.

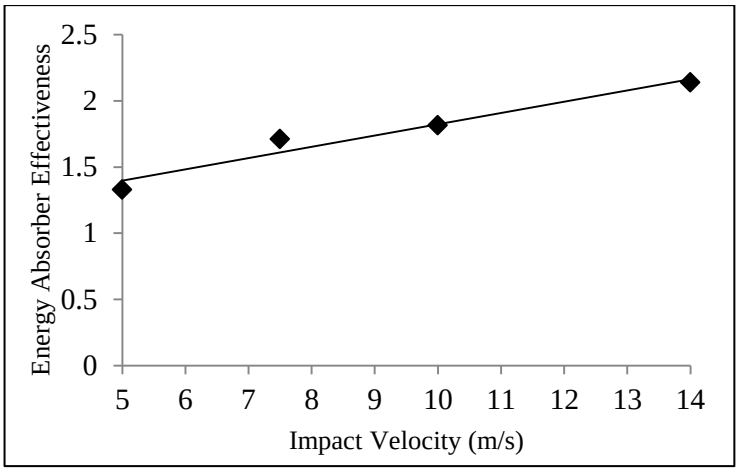

Figure 3.26 : Variation of energy absorber effectiveness factor as impact velocity changes for the impact mass of 0.6 kg.

Crashworthiness parameters of hexagonal honeycomb structures made of aluminum alloy A5052 under out-of-plane impact loads are numerically investigated. To verify the results of explicit nonlinear finite element models, the mean crush strength and stress-strain curve obtained from numerical solution are compared with experimental measurements and theoretical results reported in literature. It is observed that there are good agreements between numerical, experimental and theoretical results.

A parametric study is conducted to investigate the effect of foil thickness, cell side size, cell expanding angle, impact velocity and mass on crashworthiness parameters of the honeycomb structures. It is observed that by changing the expanding angle α between 90º and 150º with constant total mass, the crush force efficiency, total energy absorption and energy absorber effectiveness parameters increase up to 120º, thereafter these parameters decrease. The honeycomb structure with 120º expanding angle yields the largest crashworthiness parameters. By changing the foil thickness between 0.025 mm and 0.0435 mm and the cell side size between 2 mm and 5 mm simultaneously where the total mass of model is constant, it is concluded that the crush force efficiency, total energy absorption and energy absorber effectiveness parameters decrease by increasing the foil thickness and cell side size. Therefore, the honeycomb structure with small cell size and thin foil thickness has relatively larger crashworthiness parameters.

When the cell side size is constant, by changing the foil thickness between 0.01 mm and 0.05 mm, the crush force efficiency, specific energy absorption and energy absorber effectiveness factor increase slightly. On the other hand, when the foil

thickness is constant, by changing the cell side size between the 2 mm and 5 mm, the crush force efficiency and specific energy absorption decrease sharply and energy absorber effectiveness factor slightly. In order to study the effect of impact inertia on crashworthiness parameter values, the load-deformation curves for different impact mass and velocity are obtained. It is observed that by changing the impact mass between 0.6 kg and 4.7 kg while the impact velocity is constant; higher impact mass results in increasing crushing distance, because the TEA and SEA values increase as the impact mass increases. Also an increment in the impact mass causes an increment in the energy absorber effectiveness factor. Variation of the initial impact velocity from 5 m/s to 14 m/s with constant impact mass results in increasing crushing distance, because the TEA and SEA values increase as the impact initial velocity increases. Also it is observed that there is a tendency of energy absorber effectiveness factor to increase with an increase in the initial impact velocity [87]. Low energy absorber component in crush zone system is honeycomb structure. Honeycomb structures collide with low and mainly constant average force and provide low acceleration/deceleration in crush patterns. Fabricated honeycomb structures geometry and configuration is limited. Therefore, it is necessary to investigate the optimum configuration of hexagonal honeycomb with high crashworthiness characteristics The finding of this chapter will be used to design the honeycomb structure of crush zone system with optimum crashworthiness characteristics.

4. DESIGN AND OPTIMIZATION OF PRIMARY ENERGY ABSORBER ELEMENTS

4.1 Objective

The objectives of this chapter is to obtain the pyramidal tube dimension with high crashworthiness characteristics, by using response surface methodology (RSM) and MATLAB optimization tool. Also it is aimed to design the primary energy absorbers for crush zone system.

4.2 Response Surface Methodology Usage for Crashworthiness Optimization

Structural optimization often uses gradients of the objective and constraints to find a search direction of the optimal solution. Gradient-based optimization methods require the determination of first order derivatives of the underlying equations with respect to the design variables. These gradients could be computed either analytically or numerically. Unfortunately, analytical gradients in simulation-based optimization methods are difficult to obtain or even not available, due to the high non-linearity of the underlying problem, especially when friction and contact is present. For dynamic problems, like impact problems, the responses are often noisy and it is hard to find these gradients. Direct optimization methods without approximations or evolutionary algorithms like the genetic algorithm are not applicable due to the large number of function evaluations they require. Therefore, a different approach called as RMS is necessary [64-72]. Approximation methods will overcome the aforementioned problems, especially in case of crashworthiness design optimization. Approximations are constructed by using statistical model building techniques. One of those approximation methods is the so-called response surface methodology (RSM) [88,89].

Generally, RSM consists of three steps. First, a series of experiments, i.e., DOE (Design-Of-Experiment), which will yield adequate and reliable measurements of the response of interest are obtained. Then, a mathematical model that best fits the data

collected from the execution of DOE is determined. Using enough number of those values, which depends on the number of design variables and the type of function used in curve fitting, the RSM defines a surface that approximates the behavior of the objective function inside a certain design domain. Finally, the optimum setting of the experimental factors that produces the maximum (or minimum) value of the response will be found [73-78].

Generally, response surface method use statistical methods and mathematical technics to model and analyze the problems with more than one variable. For instance when response y depends on independent two variables of ζ_1, ζ_2 Then, the relationship between the response and independent variables is expressed as [88, 89],

$$y = f(\zeta_1, \zeta_2) + \varepsilon \tag{4.1}$$

where, ε is an error which represents nondependable variables, f is the response objective function. Then response function E is rearranged as,

$$E(y) = E[f(\zeta_1, \zeta_2)] + E(\varepsilon) \tag{4.2}$$

The response function η is given in terms of independent variables as,

$$\eta = f(\zeta_1, \zeta_2) \tag{4.3}$$

Note that natural variables in above equations are expressed in the units of measurement. The response function must transformed into the coded variables (x_1, x_2,… x_k) which are dimensionless with a mean of zero and with the same standard deviation. A coded variable is given by the following relation,

$$x_{ii} = \frac{\zeta_{ii} + (\max(\zeta_{ii}) + \min(\zeta_{ii}))/2}{(\max(\zeta_{ii}) - \min(\zeta_{ii}))/2} \tag{4.4}$$

with coded variables function (η) is expressed as follows,

$$\eta = f(x_1, x_2, \ldots x_k) \tag{4.5}$$

when the objective function of response function is a n order polynomial, response function is rewritten as,

$$y_1 = \beta_0 + \sum_{i=1}^{k} \beta_i x_i \ + \sum_{i=1}^{k} \beta_{ii} x_i^2 + \sum_{i<j} \beta_i x_i \, x_j + \ \varepsilon_1 \qquad \textbf{(4.6)}$$

For instance, If the objective function of response function is a second order polynomial, response function is rewritten as,

$$y = \beta_0 + \ \beta_1 x_1 + \beta_2 x_2 + \beta_3 x_1^2 + \beta_4 x_2^2 + \beta_5 x_1 x_2 + \ \varepsilon \qquad \textbf{(4.7)}$$

For n observations, the response equation becomes

$$\begin{aligned} y_1 &= \beta_0 + \ \beta_1 x_{11} + \beta_2 x_{12} + \beta_3 x_{11}^2 + \beta_4 x_{12}^2 + \beta_5 x_{11} x_{12} + \ \varepsilon_1 \\ y_2 &= \beta_0 + \ \beta_1 x_{21} + \beta_2 x_{22} + \beta_3 x_{21}^2 + \beta_4 x_{22}^2 + \beta_5 x_{21} x_{22} + \ \varepsilon_2 \\ y_n &= \beta_0 + \ \beta_1 x_{n1} + \beta_2 x_{n2} + \beta_3 x_{n1}^2 + \beta_4 x_{n2}^2 + \beta_5 x_{n1} x_{n2} + \ \varepsilon_n \end{aligned} \qquad \textbf{(4.8)}$$

Equation 4.8 can be written in the matrix form as following,

$$y = X\beta + \varepsilon \qquad \textbf{(4.9)}$$

$$y = \begin{bmatrix} y_1 \\ y_2 \\ . \\ . \\ y_n \end{bmatrix} \qquad \textbf{(4.10)}$$

$$X = \begin{bmatrix} 1 & x_{11} & x_{12} & \dots & x_{1k} \\ 1 & x_{21} & x_{22} & \dots & x_{2k} \\ \vdots & \vdots & \vdots & \vdots & \vdots \\ 1 & x_{n1} & x_{n2} & \dots & x_{nk} \end{bmatrix} \qquad \textbf{(4.11)}$$

$$\beta = \begin{bmatrix} \beta_0 \\ \beta_1 \\ . \\ . \\ \beta_n \end{bmatrix} \qquad \textbf{(4.12)}$$

$$\varepsilon = \begin{bmatrix} \varepsilon_1 \\ \varepsilon_2 \\ \vdots \\ \vdots \\ \varepsilon_n \end{bmatrix} \quad \textbf{(4.13)}$$

where, y is an n×1 vector of observation, x is an n×6 matrix of independent variables, β is a 6×1 regression vector and ε is an n×1 vector of random errors. For n observations and k number of regressor,

The sum of the square of errors is

$$L = \sum_{i=1}^{n} \varepsilon_i^2 = \sum_{i=1}^{n} \left(y_i - \beta_0 - \sum_{j=1}^{k} \beta_j X_{ij} \right)^2 \quad \textbf{(4.14)}$$

Based on the least square estimators, the function *L* must be minimized with respect to $\beta_0, \beta_1, \beta_2, \ldots \beta_k$. The least square estimator can be calculated as,

$$\hat{\beta} = (\acute{X}X)^{-1}\acute{X}y \quad \textbf{(4.15)}$$

The fitted regression model can be obtained as;

$$\hat{y} = X\hat{\beta} \quad \textbf{(4.16)}$$

In addition, the error between the observed data and fitted regression data is calculated using the following equation,

$$e = y - \hat{y} \quad \textbf{(4.17)}$$

The error sum of square (SS_E), the total sum of square (SS_T), root mean square (R_2) adjusted root mean square (R_{adj}^2), are sequentially given by the following relations, the error equations are used to validate the constructed response surface. The details of RSM can be found in references [88,89]

$$SS_E = \sum_{i=1}^{n} (y_i - \hat{y}_i)^2 \quad \textbf{(4.18)}$$

$$SS_T = \acute{y}y - \frac{\sum_{i=1}^{n}(y_i)^2}{n} \quad \textbf{(4.19)}$$

$$R^2 = 1 - SS_E/SS_T \quad \textbf{(4.20)}$$

$$R^2_{adj} = 1 - \frac{\frac{SS_E}{n-p}}{\frac{SS_T}{n-p}} = 1\text{-}(\frac{n-1}{n-p})(1\text{-}R^2) \quad \textbf{(4.21)}$$

4.3 Crashworthiness Optimization of Thin-Walled Tube by RSM

In order to obtain the pyramidal tube dimension with high crashworthiness characteristics, response surface methodology (RSM) and MATLAB optimization tool is used. By changing the thickness of the tube between 4 mm to 10 mm, pyramidal angle between 0º to 4.5º and keeping the weight constant, it is attempted to maximize total crushing efficiency function. It is noteworthy that for pyramidal angle over 3.75° and thickness over 8 mm a transition takes place from the axial progressive collapse mode to the global bending collapse mode as showed in Figure 4.1 for tube with 4.5 conical degree and 10 mm thickness.

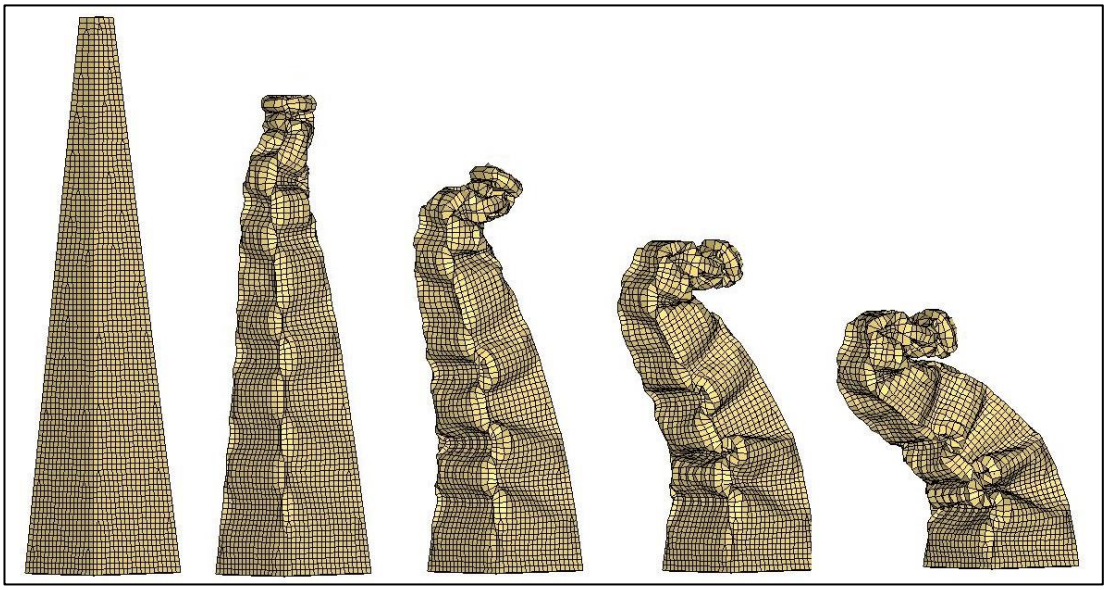

Figure 4.1 : Bending buckling of pyramidal.

In order to investigate the crush behavior and energy absorption characteristics of thin-walled tube, based on the RSM methodology surrogate RS models for F_m , F_{max} CS and TE prediction of the pyramidal tubes under axial impact loading with respect to design variables t and α are constructed.

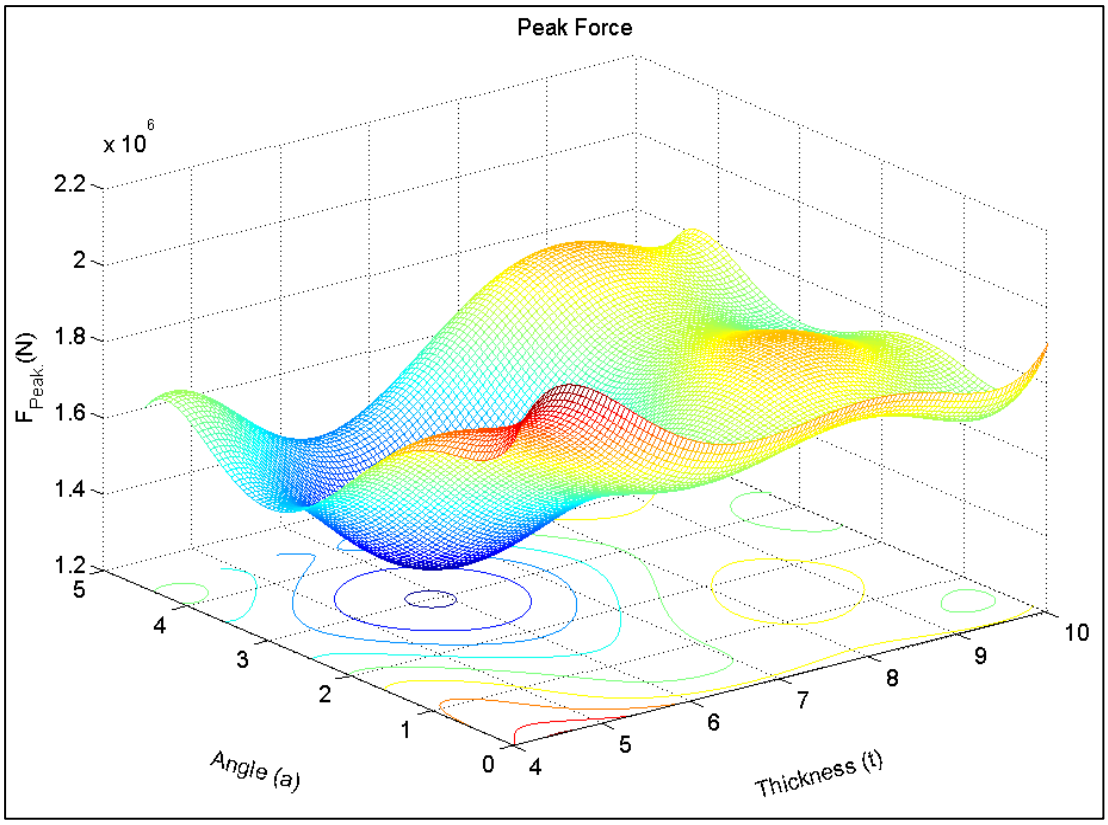

Figure 4.2 : Peak force of tube respect to thickness and conical angle by using RSM.

$$F_{max} = -4.6e7 + 3.72e7t + 4.596e6\alpha - 1.117e7t^2 - 2.526e6t\alpha - 2.484e5\alpha^2 + 1.63e6t^3 + 4.158e5t^2\alpha + 3.75e5\alpha^2 - 3.896e5\alpha^3 - 1.161e5t^4 - 2.583e4t^3\alpha - 4.828e4\alpha^2t^2 - 1.69e4t\alpha^3 + 1.214e5\alpha^4 + 3239t^5 + 418t^4\alpha + 2360t^3\alpha^2 - 283.4t^2\alpha^3 + 2005t\alpha^4 - 1.207e4\alpha^5 \quad \textbf{(4.1)}$$

R-square: 0.948

Adjusted R-square: 0.9109

$$F_m = -3.856e7 + 3.205e7t + 3.676e5\alpha - 1.024e7t^2 - 2.019e5t\alpha + 1.53e56\alpha^2 + 1.591e6t^3 + 2111t^2\alpha + 6.265e4t\alpha^2 - 1.464e5\alpha^3 - 1.198e5t^4 + 5184t^3\alpha - 1.474e4\alpha^2t^2 + 9610t\alpha^3 + 2.655e4\alpha^4 + 3497t^5 - 377.3t^4\alpha + 888.3t^3\alpha^2 - 791.6t^2\alpha^3 + 394.4t\alpha^4 - 2394\alpha^5 \quad \textbf{(4.2)}$$

R-square: 0.9753

Adjusted R-square: 0.9577

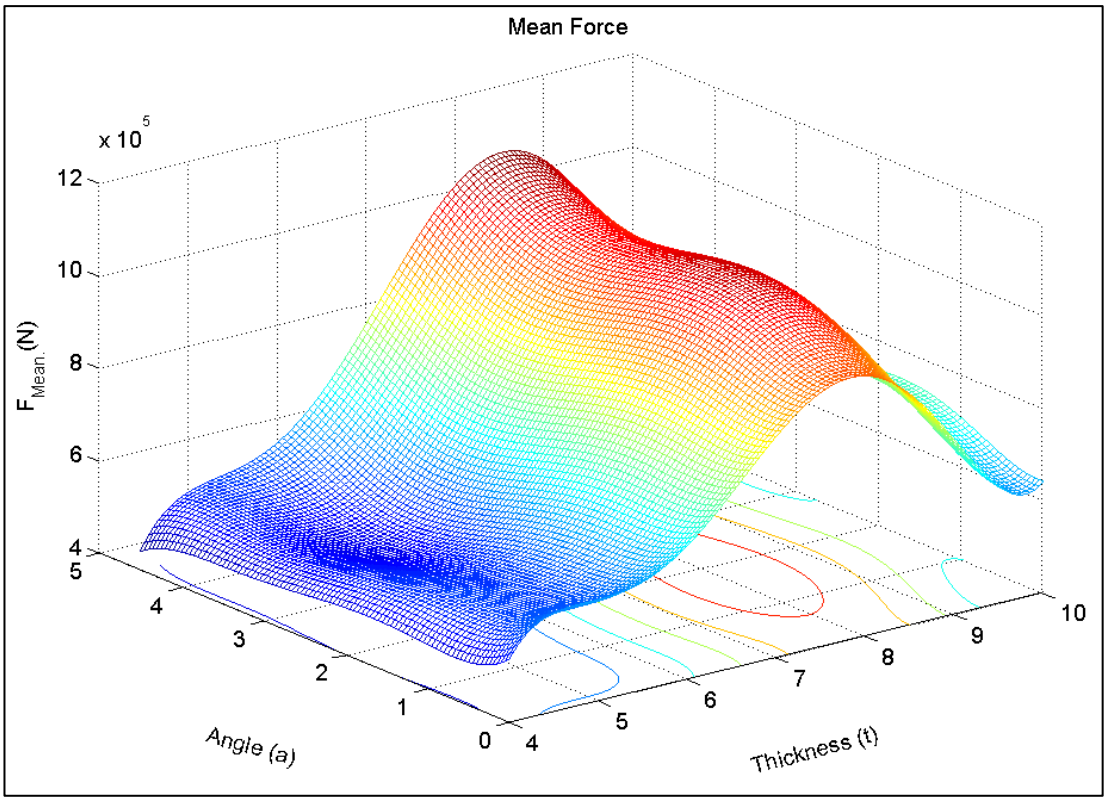

Figure 4.3 : Mean force of tube respect to thickness and conical angle, using RSM.

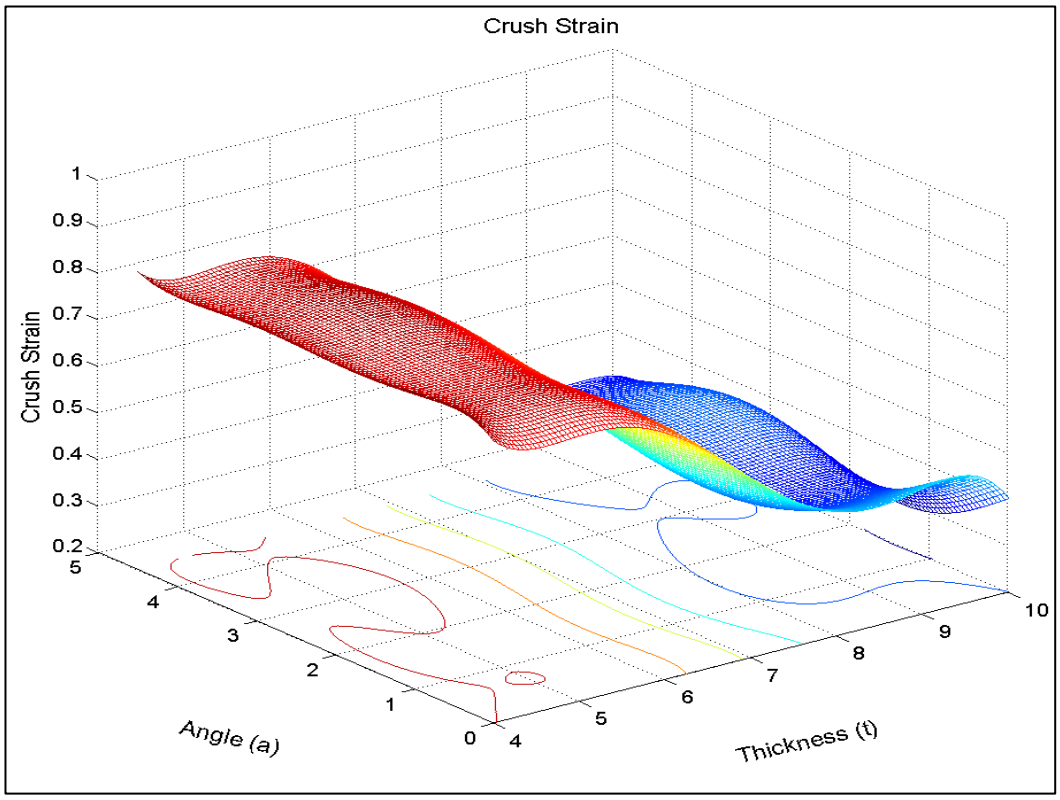

Figure 4.4 : Crush strain of tube respect to thickness and conical angle, using RSM.

$$\begin{aligned}\mathrm{CS} = {} & 25.3 - 20.06t + 0.05924\alpha + 6.389t^2 + 0.01859t\alpha \\ & - 0.1976\alpha^2 - 09875t^3 + 0.01129t^2\alpha - 0.0236t\alpha^2 \\ & + 0.1274\alpha^3 + 0.07391t^4 - 0.003407t^3\alpha \\ & + 0.007064\alpha^2t^2 - 0.004917t\alpha^3 - 0.02635\alpha^4 \\ & - 0.002148t^5 + 0.0001907t^4\alpha - 0.0002974t^3\alpha^2 \\ & - 9.767e - 5t^2\alpha^3 + 0.0004091t\alpha^4 + 0.002086\alpha^5 \end{aligned} \quad \textbf{(4.3)}$$

R-square: 0.992

Adjusted R-square: 0.9862

The objective function and constraints of the pyramidal thin-walled tube design optimization are defined as follows:

Objective function is total efficiency that is determined by multiplying the crush strain and crush force efficiency. The surface diagram of total efficiency respect to conical angle and wall thickness is shown in Figure 4.5.

$$\begin{aligned}\mathrm{TE} = {} & 15.88 - 12.18t - 0.808\alpha + 3.66t^2 + 0.4602t\alpha \\ & - 0.06338\alpha^2 - 0.5317t^3 - 0.07724t^2\alpha \\ & - 0.05369t\alpha^2 + 0.1194\alpha^3 + 0.03758t^4 \\ & + 0.004823t^3\alpha + 0.008607\alpha^2t^2 - 0.00116t\alpha^3 \\ & - 0.03106\alpha^4 - 0.001039t^5 - 8.33e5t^4\alpha \\ & - 0.0004265t^3\alpha^2 + .0001072t^2\alpha^3 - 5.661e \\ & - 5t\alpha^4 + 0.002841\alpha^5 \end{aligned} \quad \textbf{(4.4)}$$

R-square: 0.9586

Adjusted R-square: 0.9291

Constraints:

Equality constraint: W= ρ[8D+ 8Lsin(α)]t

Inequality constraints:

g_1: $4 \leq t \leq 10$

g_2 : $0 \leq \alpha \leq 4.5$

where ρ is the density of material, L is the length of tube and D is the side length of small cross-section of pyramidal tube.

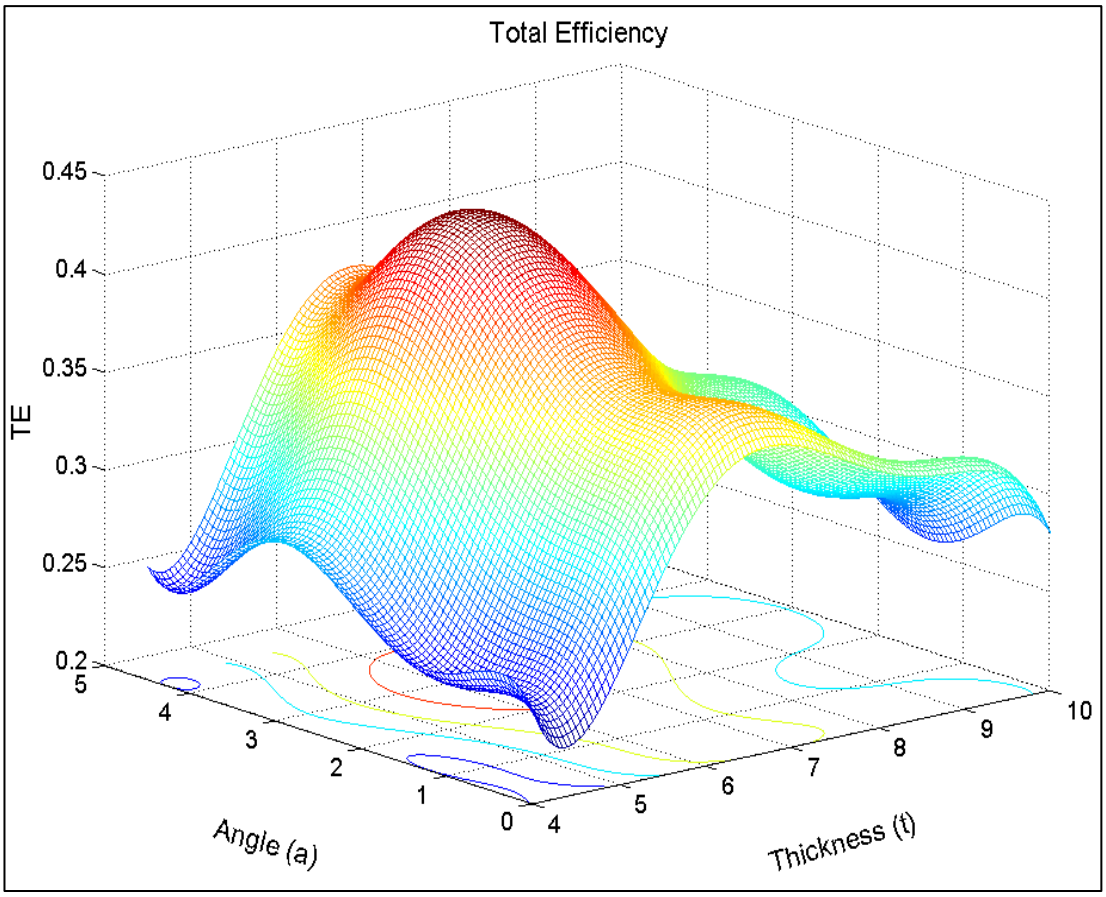

Figure 4.5 : Total efficiency of tube respect to thickness and conical angle, RSM.

4.4 Design and Verification of Energy Absorber Element Response

The design requirement for primary energy absorbers is 2.2 MJ energy absorption within 80 cm stroke. By using Equations 2 and 3, the average force is determined as 2.5 MN.

The relation between the side length and thickness with the average force of square thin walled tube is expressed as follow [6]:

$$P_m/M_0 = 52.42(\frac{c}{h})^{1/3}[1 + (0.33v_0/cD)^{\frac{1}{q}}] \quad \textbf{(4.5)}$$

where

$$M_0 = \sigma_y h^2/4 \quad \textbf{(4.6)}$$

And P_m is the average load, c is the side length, h is the thickness of tube and M_0 is the fully plastic bending moment per unit width.

For mild steel, Cowper-Symonds constant is D = 6844 s^{-1} and Cowper-Symonds exponent is q=3.91 [30].

With four tubes, the average load P_m becomes 0.625 MN for each tube. By taking h=6 mm and substituting of the average load value P_m, dimensions of pyramidal tube are determined as shown in Figure 4.6.

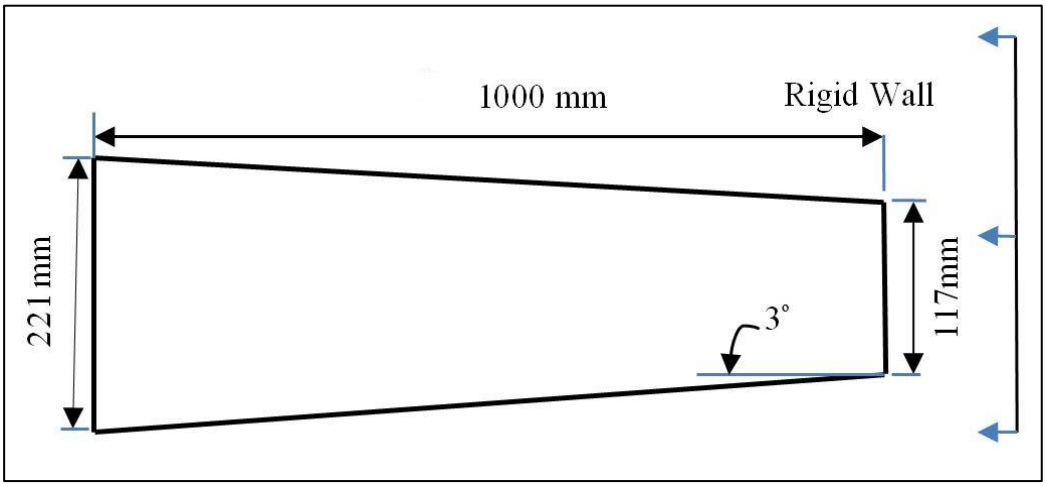

Figure 4.6 : Pyramidal tube dimensions designed for usage in crush zone of CEM.

In order to evaluate the crush zone performance, the first step is the verification of energy absorber element response. In practice, it has advantages of including the reinforcements, diaphragm and localized deformation to reduce the initial collapse load and to ensure that crush occurs in a similar manner for various collision speeds and load combinations. Tubes are modeled as a 3D deformable shell with the element type of S4R type in ABAQUS software. The tubes have the lengths of 1,000 mm and thicknesses of 6 mm. Material properties assigned to the model are those of the mild steel A350. For simulation of the dynamic axial crushing, the fixed rigid plate is constrained in all degrees of freedom. The support is tied to the end of the tube, and the mass of 8 tons is attached to the reference point of the support. To assure stability in tube plastic deformation, different length to section size ratio has been examined. In addition, tubes attached to each other by webs in longitude in crush zone integration. In model analysis, in order to obtain a smooth post-buckling response of the deformed tube; the first 10 buckling modes that obtained by running an eigenvalue buckling analysis of the tube using ABAQUS/Standard. Then, the *IMPERFECTION option in ABAQUS/Explicit has been introduced to read the buckling modes, and to perturb the nodal coordinates [81]. Both the tube and support

are impacted to the fixed rigid plate with the downward initial velocity of 50 km/h. The progressive deformation mode of thin-walled tube in different time steps are shown in Figure 4.6. Also Figure 4.7 shows the force-crush behavior of a single thin walled tube impact to a rigid plate.

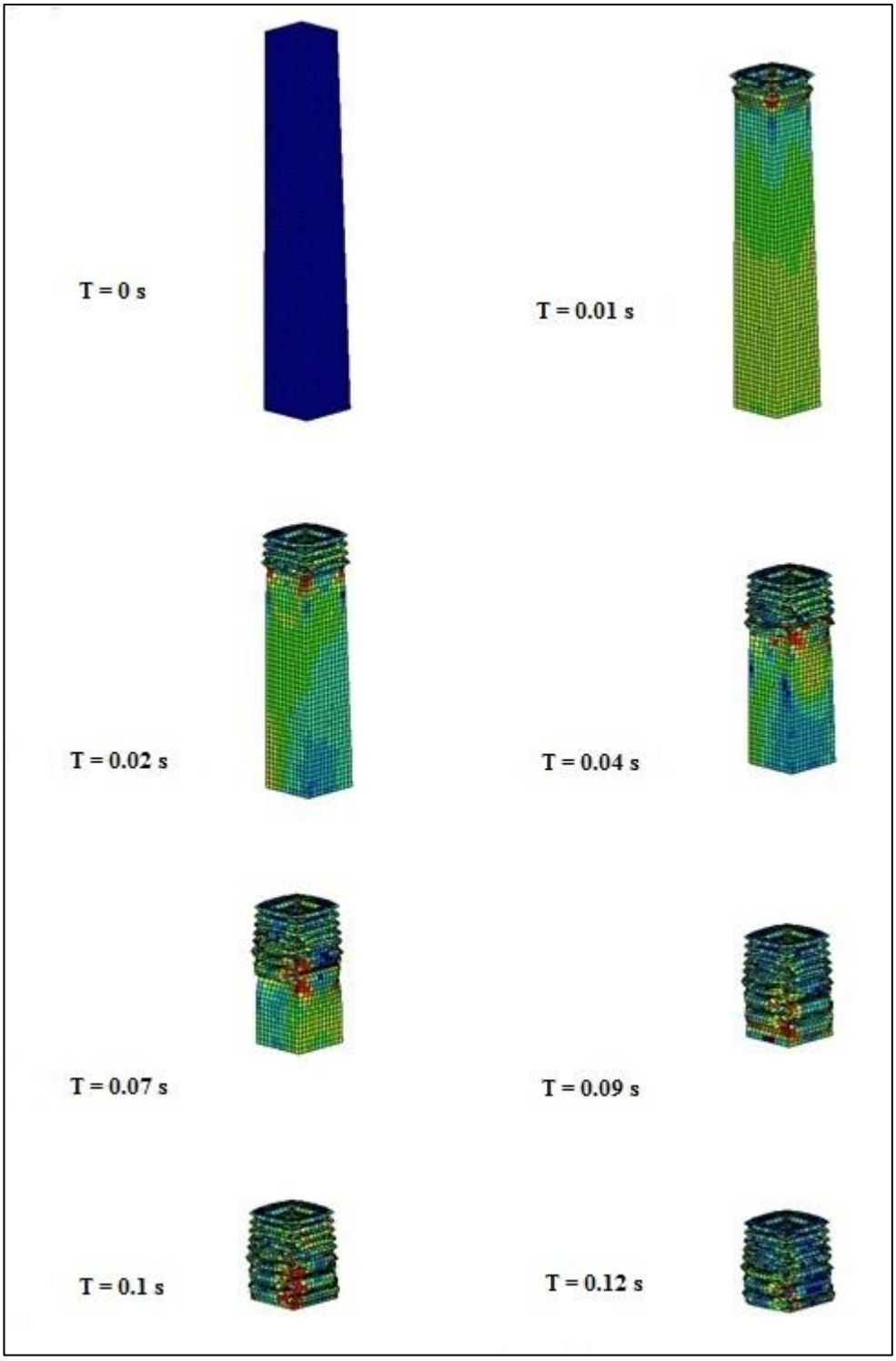

Figure 4.7 : Deformation of thin-walled tube designed for usage in crush zone.

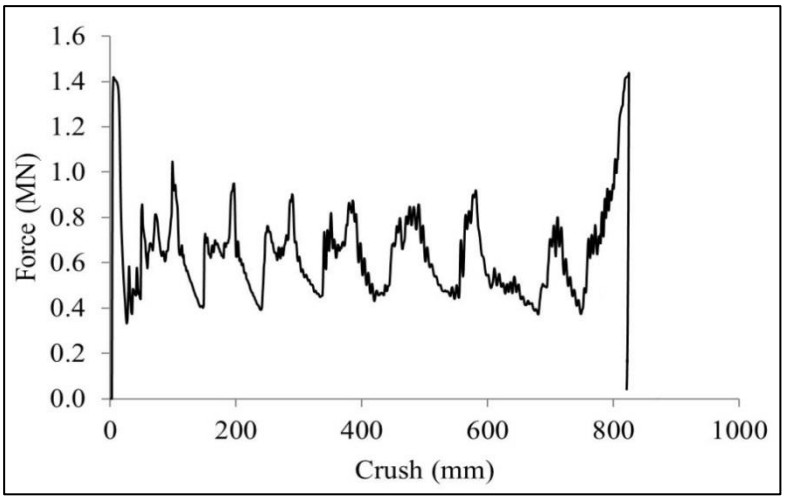

Figure 4.8 : Force-Crush behavior of a thin walled tube impact to a rigid plate.

The pyramidal tube collapse asymmetrically and in stable manner. The axial force reaches an initial peak about 1.4 MN magnitude, followed by a sharp drop and then fluctuations. These fluctuations are a result of formation of the successive folding. Each subsequent peak corresponds to the onset of a folding process. The energy absorbed is simply the area under this curve. For practical purposes, the average force is often worked out as an indication of energy absorption capacity. The tube wall undergoes sever inward and outward plastic bending, with possible stretching. The FE results approved that the thin walled tube provides the energy absorption and progressive deformation parameters as it is designed.

In next the chaper, in order to design primary energy absorbers the pyramidal tube dimension will be used. Two primary energy absorbers exist on the car, one on each side of the centerline of the car and consist of four pyramidal thin walled tubes having 1,000 mm lengths. Each absorber is welded to and supported by the passenger car structure that is not intended to deform. The load on the outboard ends of the primary energy absorbers is applied to the back of the support plate. An initial gap exists between the outboard end of the absorber and the back of the buffer beam before activation of the crush zone (so that the absorbers do not carry any operational loads). The energy absorption capacity of primary energy absorber is 2.2 MJ within 80 cm stroke.

5. CRASH ENERGY MANAGEMENT DESIGN OF RAILWAY PASSENGER CAR

5.1 Objective

In this chapter a design approach for crash energy management (CEM) system of railway passenger car has been developed. In order to investigate the benefits provided by the CEM system, designed crush zone is applied a N13-type used by the Turkish State Railway Company. A full-scale railway passenger car collision with a rigid wall is simulated by using dynamic/explicit finite element (FE) methods. The crushing force, secondary impact velocity, acceleration and velocity time-history, and deformation modes are computed to allow a comparison of the crashworthiness performance of a passenger car equipped with the proposed CEM system with that of a conventional passenger car.

5.2 Modeling of Conventional Passenger Car

The railroad passenger car model used in this study was initially designed with a stiff underframe and developed to withstand very large buff and draft forces. The car has approximately the width of 2800 mm, length of 26000 mm, height of 3300 mm and weight of 12.5 tons except for bogies, passengers and auxiliary equipment. The total weight of passenger car is approximately 24 tons.

Altair HyperWorks 11.4/Hypermesh [90] is used in the construction of passenger car's full scale FE model and ABAQUS/Explicit 6.10 is used as the solver and to view the numerical results. The FE model of conventional passenger car contains approximately 1,650,000 elements. Approximately 95 percent of the elements are linear quadrilateral shell elements, 3 percent of the elements are rigid connection elements to represent welding and the rest of the elements are linear triangular shell elements and linear 3-D solid elements. The element size is variant between 15 mm and 20 mm. Discrete parts are attached to one another via rigid bars, which simulate perfectly welded connection between the corresponding nodes of adjacent parts.

Bogies are represented by lumped masses. Rail track effects are simulated by applying appropriate boundary conditions to the FE model.

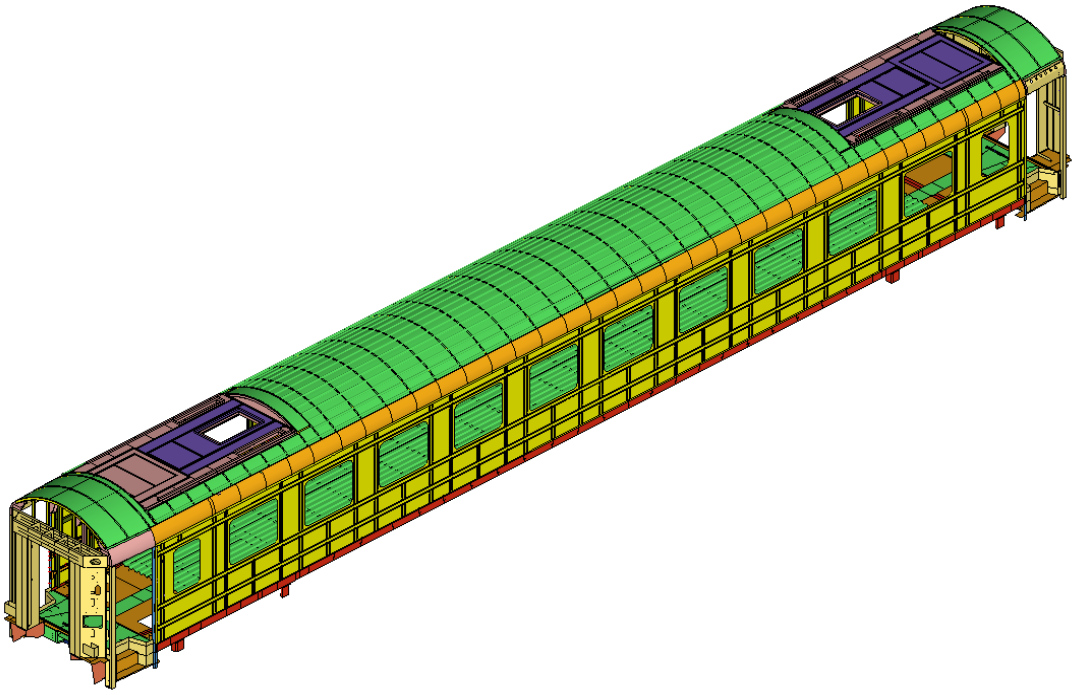

Figure 5.1 : Solid model of convetional passenger car N13 Type used by TCDD.

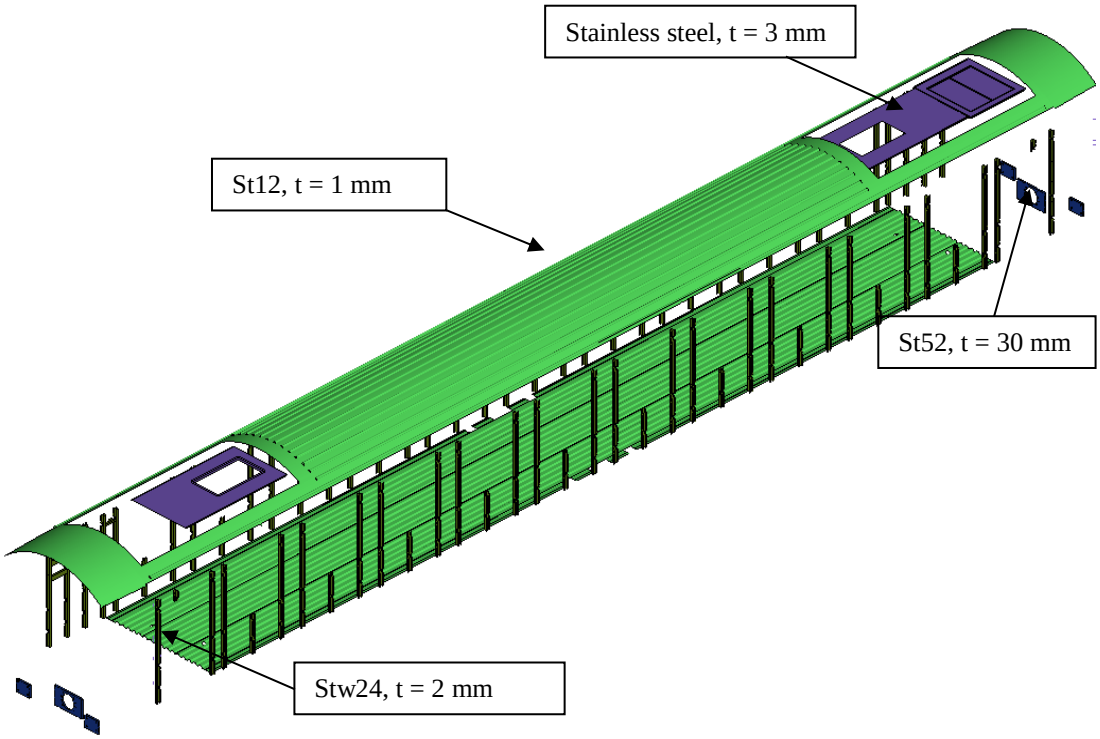

Figure 5.2 : The dismantled view of N13 type made from St12, Stw24, St52 and SS.

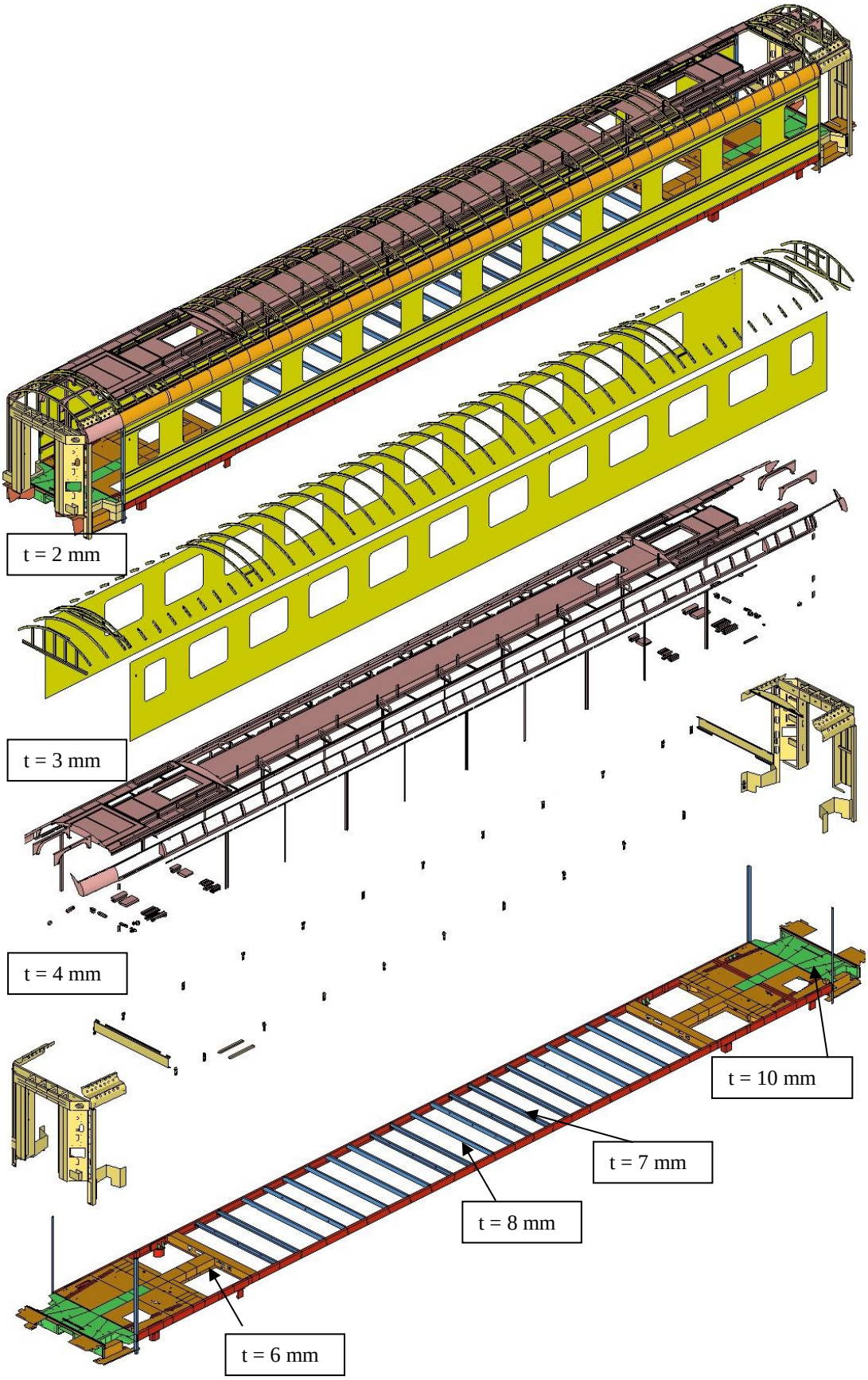

Figure 5.3 : The dismantled parts of passenger car N13 model fabricated by St372.

The materials used in the conventional passenger car are stainless steel, St12, Stw24, St 372 and St 52. Main parts of the car body and underframe fabricated with St372 material. Vertical beams on the car body fabricated form Stw24. Roof cover plate and underframe plate fabricted from St12. The parts classifications of car body with respect to fabricated material plate thickness have been demonstrated in Figures 5.2 and 5.3.

Since the FE model is subject to large plastic deformations under the impact load, elastic-plastic behavior of the materials is defined in the FE model. In addition, the gravitational acceleration is considered in the FE model. The rigid wall is defined as discrete planer shell and assigned a reference point to the geometric center of rigid wall. To model the fixed rigid wall boundary condition, reference point all degrees of freedom are restricted. The velocity is applied to every node. The time step and the total simulation time period is 1×10^{-6} seconds and 120 milliseconds respectively. To validate the FE model, static FE simulation studies results of test that were completed according to the International Standard UIC CODE OR 577. The same tests were also been applied to a prototype passenger car located at TUVASAS (Turkish Wagon Industry Inc.) in Adapazari, Turkey. A total of 30 strain gauge rosettes were applied to a quarter of the car body to capture the plane-stress behavior of the structure, and the simulation results were compared with experimental measurements. Figure 5.4 shows the experimental car setup and some strain gauges' positions. Figure 5.5 shows the comparisons of the measurements with FE stress results obtained for a symmetrical compression force of 200 tons at the strain gauge points. Based on the studies in Ref. 91, in brief, 27 gauge locations demonstrate less than 10% error in von Mise stress values. The numerical model is validated with static experimental measurements before running dynamic/explicit analyses of the railroad passenger car. Good agreement is observed between measurements and FE results, which indicate that the numerical model accurately represents the real structure [91].

a)

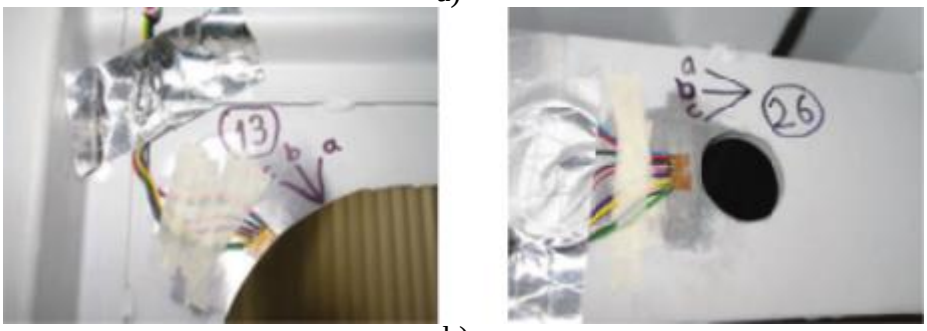

b)

Figure 5.4 : a) Setup for passenger car test, (b) and some strain gauges.

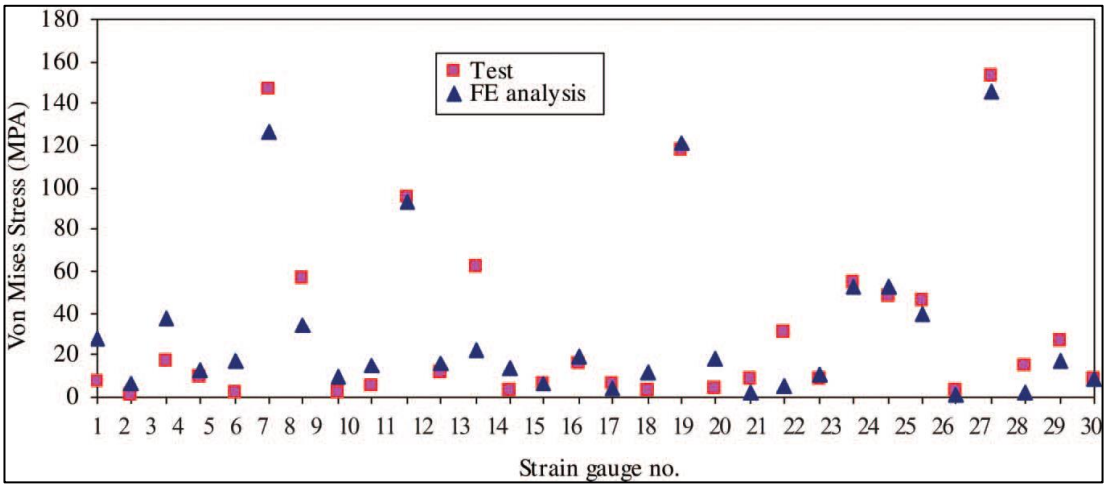

Figure 5.5 : The comparisons of the measurements with FE stress results for of 200 tons compression force.

Figure 5.6 and 5.7 show the progress of conventional passenger car crash deformations in the underframe during 50 km/h impact to a rigid wall. In order to increase the visibility, some elements of the underframe were hidden. Plastic deformation of the passenger car initiated with local plastic deformation in the roof, walls and head of underframe. When progressive local buckling reaches to the stiffer shell elements about 40 ms after the impact, large stress values are observed in the occupant area of passenger car. Then, 50 ms after the impact, large buckling in structural elements occurred in the occupant area both in the underframe and side walls.

The force-crush curve extracted for the conventional passenger car is plotted in Figure 5.8. The plastic deformation of conventional passenger car is characterized by a high initial force peak followed by a relatively constant low force in the first zone. In the second zone, the deformation is initiated with a high peak force followed by a rapid force reduction. Note that the conventional passenger car underframe in the second zone consists of stiff shell elements. Longitudinal damage in the second zone is followed by lateral buckling in the occupied area of passenger car as shown in Figure 5.7.

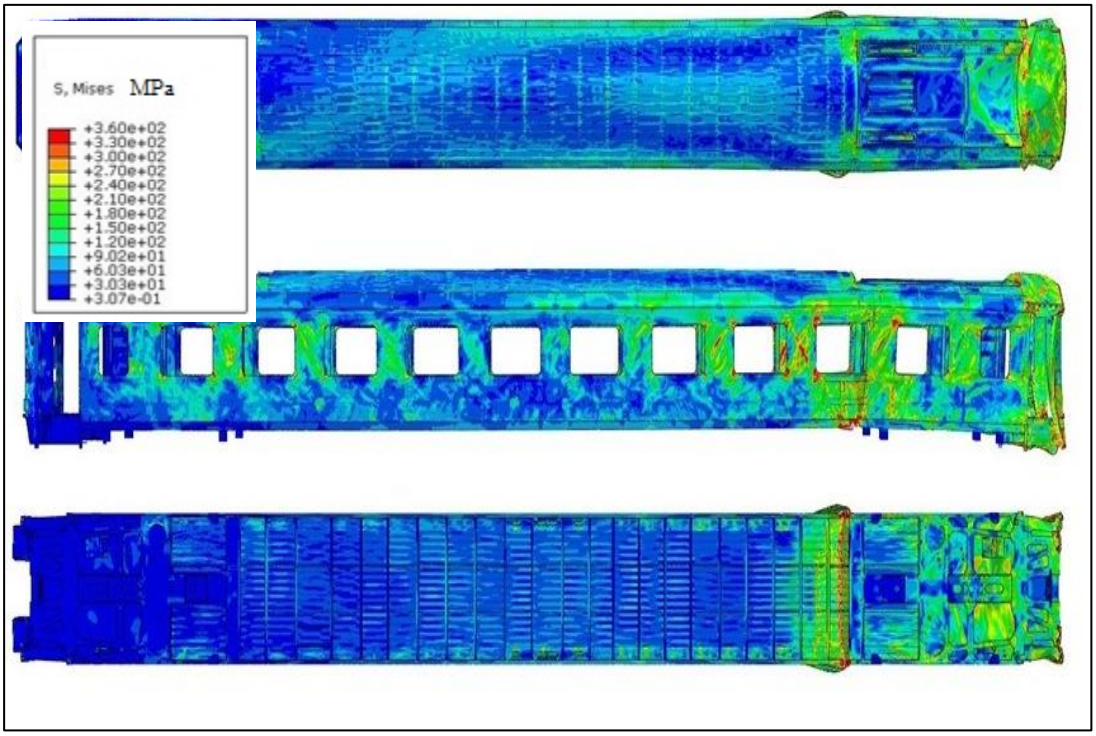

Figure 5.6 : The stress distribution in conventional passenger car impact, 50 km/h.

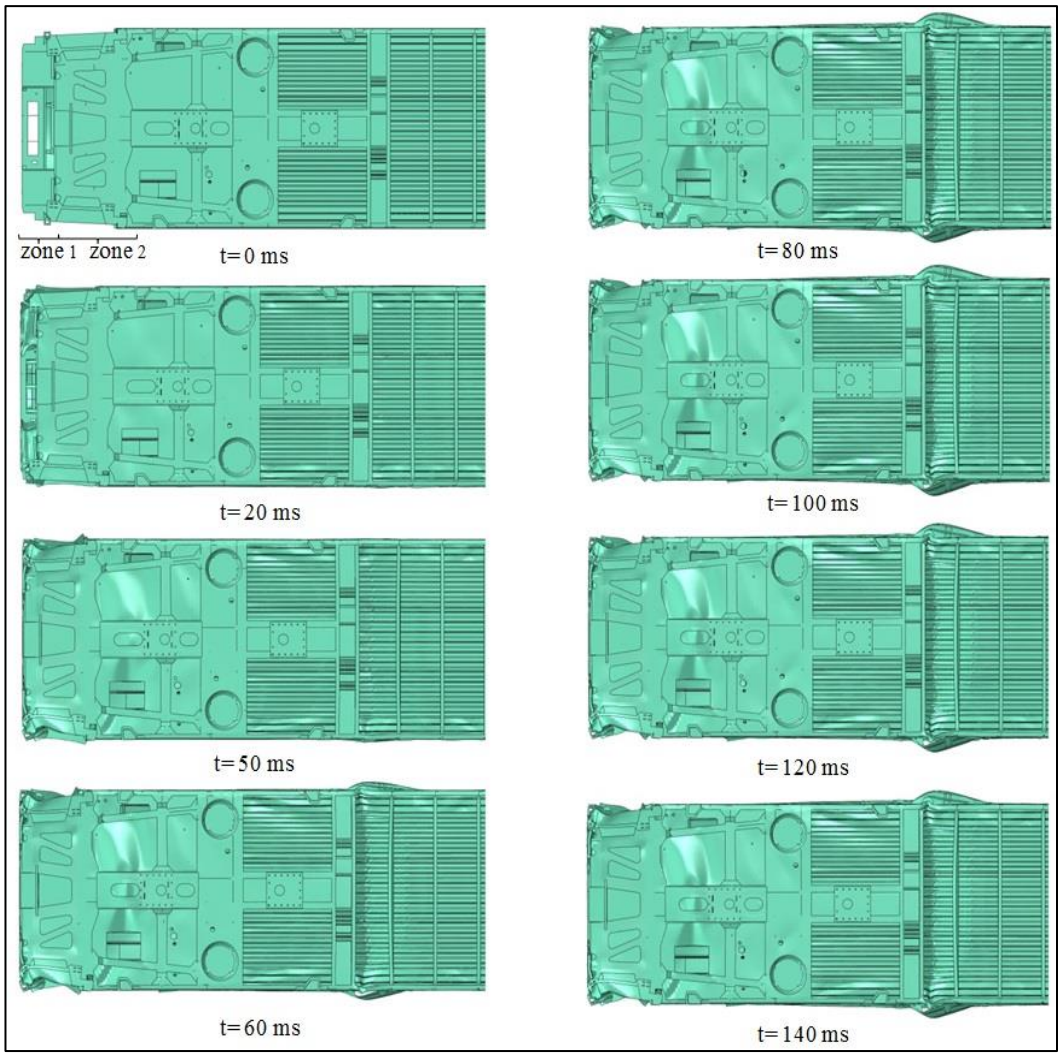

Figure 5.7 : The progress of deformation in conventional car crash with 50 km/h.

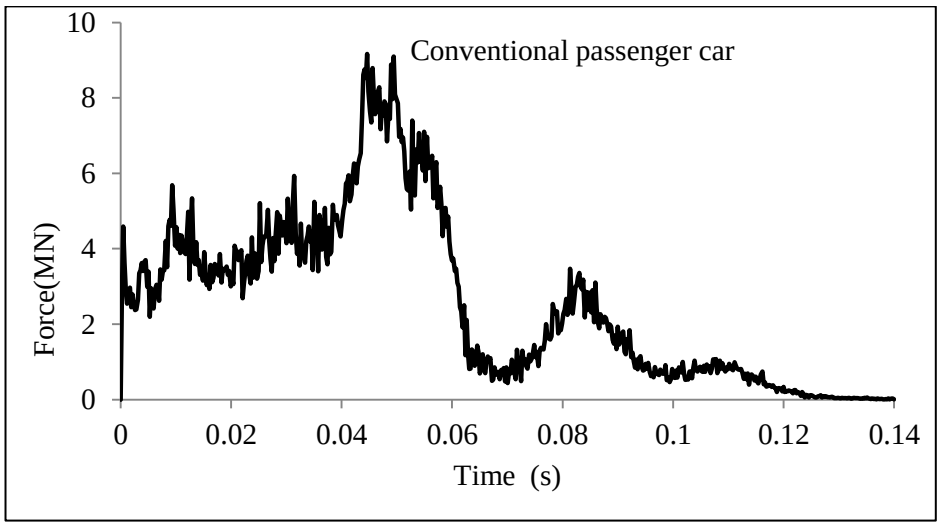

Figure 5.8 : The force v.s. time variation of the conventional car in 50 km/h impact.

5.3 New Crush Zone Design

Several regulations and standards have been established to improve the crashworthiness of railway equipment. In the US, the principal design standard for railway equipment crashworthiness is the Federal static end strength regulation, 49 Code of Federal Regulations (CFR), paragraph 238.203 [35]. Related European standard (EN 15227– Railway applications, crashworthiness requirements for railway vehicle bodies) defines some collision scenarios and passive safety requirements [36].

5.3.1 One car collision with rigid wall

Based on accident statistics and traveling velocity in Turkey, the railway passenger car crush zone is designed for an identical passenger car having an average mass of 24 tons and crash velocity of 50 km/h. One of the principles of crashworthiness design is to absorb kinetic energy of passenger cars. The crash scenario considered in this study is as follows: one passenger car impacts into a rigid standing wall, the collision energy is obtained by using the law of conservation of impulse.

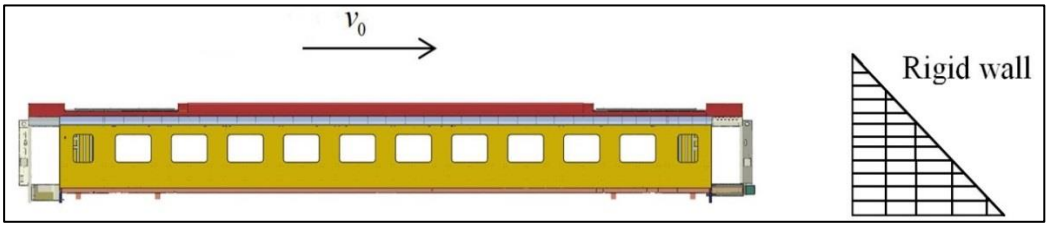

Figure 5.9 : The schematic impact of one passenger car into a rigid standing wall.

The total kinetic energy is given by following expression:

$$E_t = \frac{1}{2} m v_0^2 \qquad \textbf{(5.1)}$$

where v_0 is the initial velocity of passenger car and m is the mass of passenger car plus CEM system. The deformation length l of the passenger car is given by the following expression:

$$l = \frac{v_0^2}{2a_{av}} \qquad \textbf{(5.2)}$$

where a_{av} is the average acceleration of passenger car. Then, total energy absorbed by the passenger car structure can be expressed by

$$E_{abs} = F_{av} l = m a_{av} l \quad \textbf{(5.3)}$$

F_{av} is the magnitude of the average force acting on the passenger car during crash.

5.3.2 Crush zone components

The CEM system design is intended to concentrate the structural deformation to the unoccupied space of passenger car. The requirement for the total energy absorption in the design stage is 2.7 MJ in about 1.1 m of crush. The crush zone that is developed for a passenger car includes the honeycomb structure boxes, the sliding sill mechanism, the fixed sill mechanism, primary energy absorbers and shear bolts. These components are briefly explained below.

Honeycomb structure box: In order to reduce the accelerations during collision and provide a smooth crush, honeycomb structures are used in front of the buffer beam. The honeycomb box is designed to be activated in a prescribed impact force range and absorbs certain kinetic energy of the passenger car. Two honeycomb boxes are placed on the passenger car, one on each side of the centerline of the car. When the impact force pushes back the coupling and the ends of coupling come into contact, the shear bolts between the buffer beam and honeycomb structure box will be cut at a predefined load and the buffer beam will crush the honeycomb block. The energy absorption capacity of the honeycomb box is designed to be 0.5 MJ within 30 cm stroke, e.g., see Figure 5.10.

The sliding sill mechanism: The sliding sill provides a guide for the end crush zone of the passenger car. It consists of the U-shaped beams sliding within the guide channels. The material of sliding sill is St52. It is attached to the fixed sill through the shear bolts. After the honeycomb box is activated, the load at the end frame rises, and when the impact load reaches to a prescribed load, the sliding sill shear bolts fracture and the buffer beam crash to the primary energy absorber elements, e.g., see Figure 5.10.

Primary energy absorber: Two primary energy absorbers exist on the car, one on each side of the centerline of the car and consist of four pyramidal thin walled tubes

having 1,000 mm lengths with HSLA 350 material. Each absorber is welded to and supported by the passenger car structure that is not intended to deform. The load on the outboard ends of the primary energy absorbers is applied to the back of the support plate. An initial gap exists between the outboard end of the absorber and the back of the buffer beam before activation of the crush zone (so that the absorbers do not carry any operational loads). The energy absorption capacity of primary energy absorber is 2.2 MJ within 80 cm stroke, e.g., see Figure 5.10.

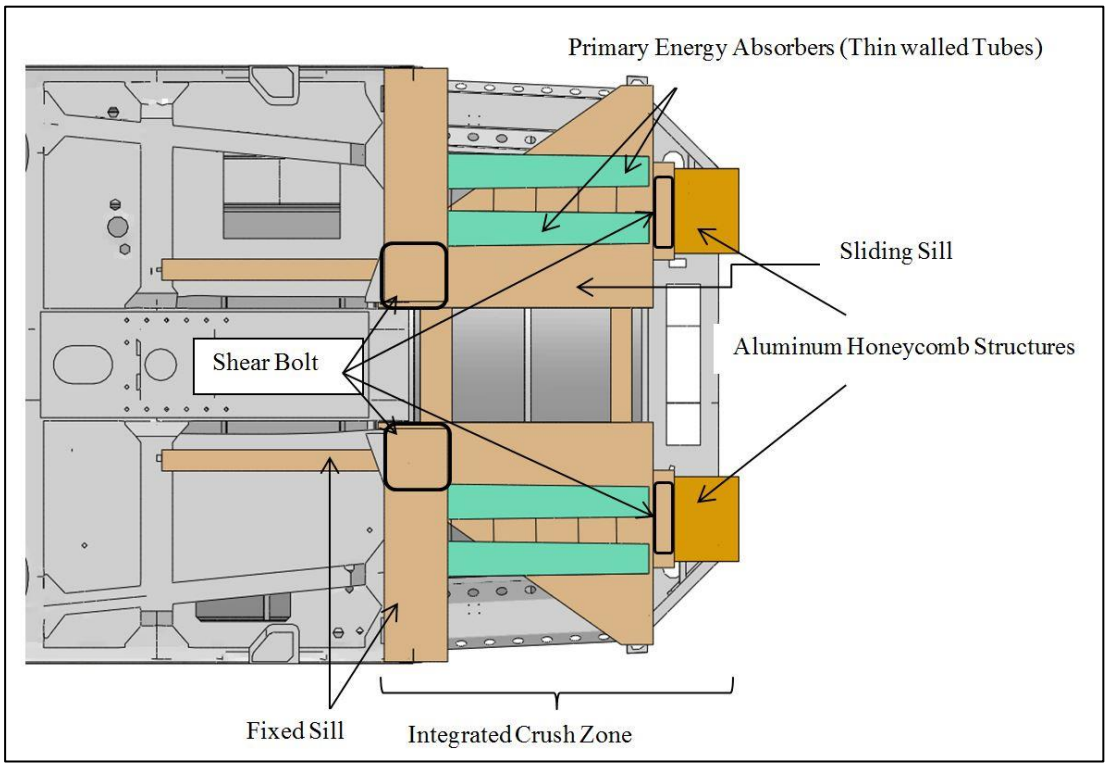

Figure 5.10 : The view of crush zone system attached to the end of passenger car.

5.3.3 Orthotropic material modeling of honeycomb structures

Simulation of honeycomb structures in crush zone by using shell element resulted by large amount of elements and nodes. Beside of being so complicated geometric model, required CPU time to run the program is not feasible. Therefore orthotropic material model in hyperwork software has been employed to simulate the crush behavior of honeycomb structures of crush zone. As shown in Figure 5.11 there is good agreement between shell element and orthotropic material modeling.

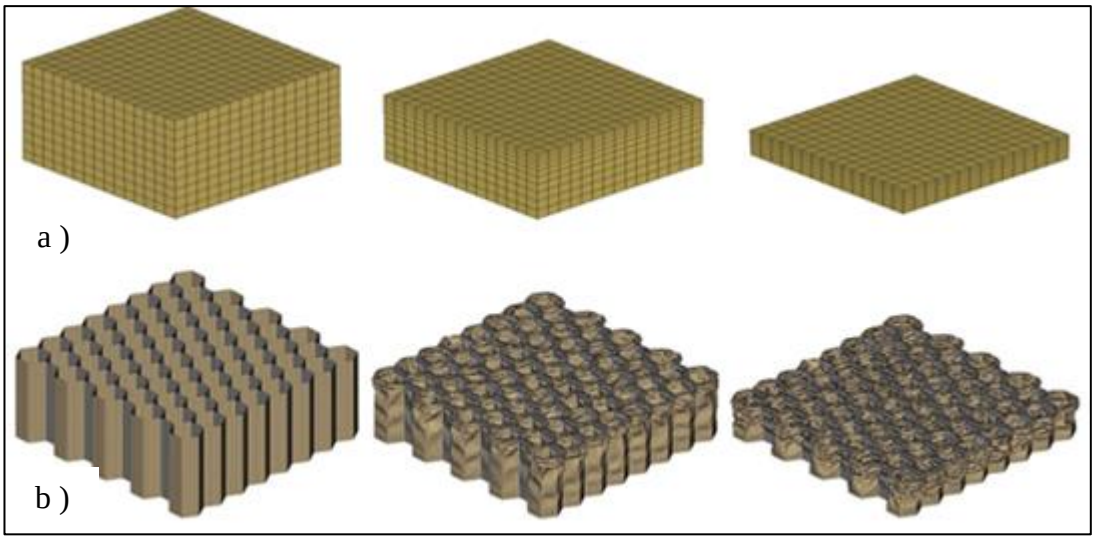

Figure 5.11 : a) Orthotropic material modeling b) Shell element modeling.

Elastic constants of orthotropic honeycombs with double thickness cell walls [92] are as follow. The geometric configuration of honeycomb structure is shown in Figure 5.12.

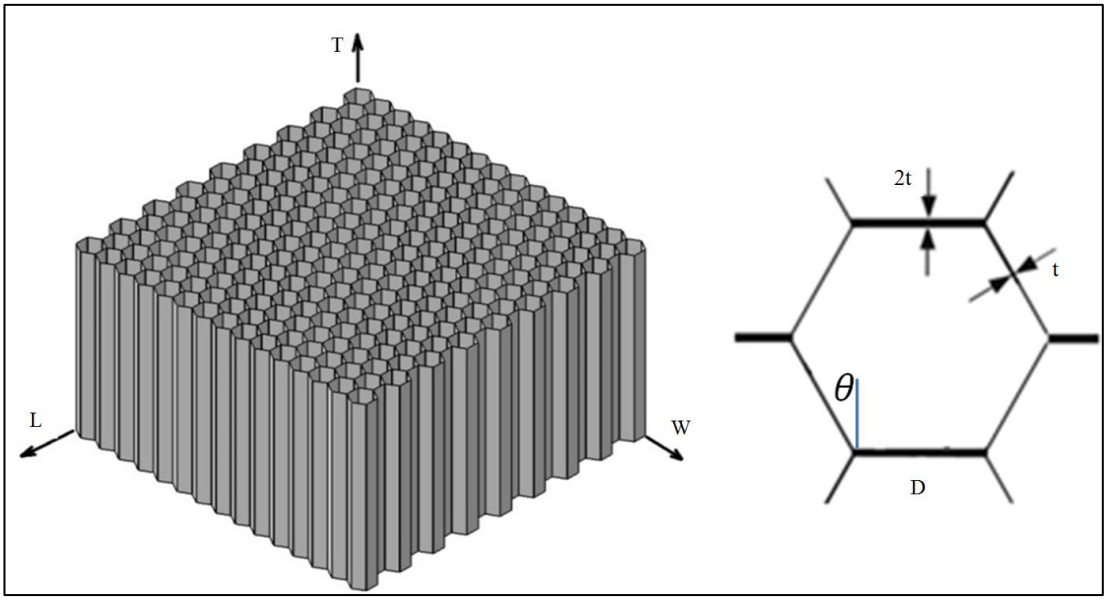

Figure 5.12 : A honeycomb specimen with coordinate systems.

Young's modulus

$$E_{11} = E_s(\frac{t}{D})^3 \frac{1+sin\theta}{cos^3\theta} \quad \textbf{(5.4)}$$

$$E_{22} = E_s(\frac{t}{D})^3 \frac{cos\theta}{(1+sin\theta)sin^2\theta} \quad \textbf{(5.5)}$$

$$E_{33} = E_s(\frac{t}{D}) \quad \frac{2}{(1+sin\theta)cos\theta} \tag{5.6}$$

Shear modulus

$$G_{23} = G_s(\frac{t}{D}) \quad \frac{cos\theta}{1+sin\theta} \tag{5.7}$$

$$(\frac{t}{D}) \quad \frac{1+sin\theta}{2cos\theta} \leq \frac{G_{31}}{G_s} \leq (\frac{t}{D}) \quad \frac{1+sin^2\theta}{1+sin\theta cos\theta} \tag{5.8}$$

$$G_{21} = E_s(\frac{t}{D})^3 \frac{1+sin\theta}{17cos \quad \theta} \tag{5.9}$$

$$G_{31} \cong G_{31\,lower} + \frac{0.787}{\frac{t}{D}}(G_{31\,upper} - G_{31\,lower}) \tag{5.10}$$

Poisson's ratio

$$\nu_{21} = \frac{cos^2\theta}{(1+sin\theta)sin\theta} \tag{5.11}$$

$$\nu_{31} = \nu_{32} = \nu_s \tag{5.12}$$

$$\nu_{12} = \frac{(1+sin\theta)sin\theta}{cos^2\theta} \tag{5.13}$$

$$\nu_{13} = \nu_{23} \approx 0 \tag{5.14}$$

where, E_s, G_s are the Young's modulus, shear modulus of honeycomb material, respectively (see section 3.3) .

In the honeycomb box, two aluminum honeycomb blocks with the dimensions of 360 mm width, 360 length and 440 mm height are positioned. These blocks absorb the energy of 0.5 MJ in 30 cm stroke which was the design goal.

5.3.4 Simulation of shearing bolts

The shear bolts in crush zone are modeled by using spot welds. The spot weld is modeled by *BOND keyword in ABAQUS software. The failure criterion for a spot weld is defined as:

$$\left(\frac{max(F^n, 0)}{F_f^n}\right)^2 + \left(\frac{F^s}{F_f^{ns}}\right)^2 \leq 1.0 \qquad \textbf{(5.15)}$$

where, F_f^n is the force required to cause failure in tension, F_f^s is the force required to cause failure in pure shear, and F^n and F^s are normal and tangent forces carried by spot weld respectively. Figure 5.13 shows the finite element model of spot weld failure step.

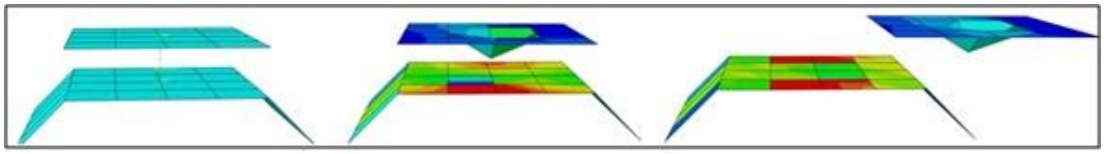

Figure 5.13 : The finite element model of spot weld failure step done in ABAQUS.

BOND is not supported module therefor by using Keywords Editor toolset added to the model. To specify spot welds, a contact pair that contains spot welds must be a pure master-slave contact pair; because the contact pair consists of two deformable surfaces, ABAQUS/Explicit would normally use a balanced master-slave contact pair. In such situation to define a pure master-slave contact pair it is necessary to specify a weighting factor. Contact pairs containing spot welds must be defined in the first step of a simulation. The spot welds are located at the nodes of the slave surface of the contact pair [82]. The shear bolts designed to be cut in about 5MN force. 16 numbers of A490 grade, bolts with 25.4 mm diameter satisfied the requirements. Shear strength of bolts is 680MPa.

5.3.5 Working mechanism of crush zone system

The first step to verify the crush zone performance is the analysis of crush zone response individually in impact with rigid wall. To simulate the crush zone working mechanism, by using lumped mass method the inertia and velocity (50 km/h) of passenger car modeled in hypercrash. As it is shown in Figure 5.14 when the crush zone with 50 km/h impact with rigid wall in first step the honeycomb box is activated (see Fig 5.14 a and b), the honeycomb structure collapse under the kinetic energy of car and absorbs an amount of energy. After the completion of effective crash length of honeycomb structure the cutting loads on the shear bolts of sliding sill reach the prescribed shear loads of bolts. In this step the shear bolts fracture and the primary

energy absorbers activated (see Fig 5.14 c). after starting of thin-walled tube crash pattern the fixed proceed to inside of crush zone.

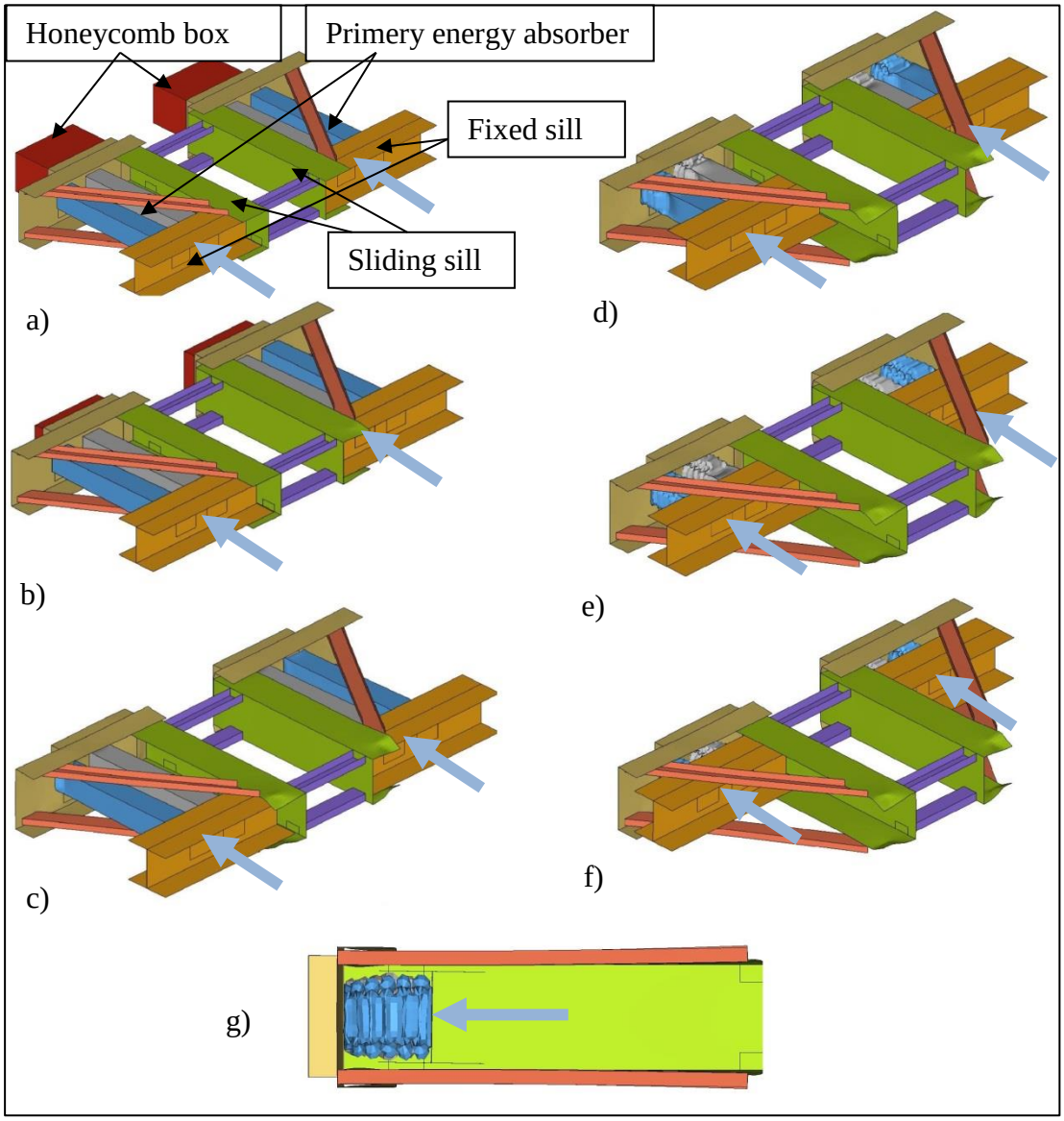

Figure 5.14 : Working mechanism of crush zone system before installing to car.

During tube crushing it is necessary that sliding sill work as a guide channel and provide appropriate space to slide over the fixed sill. The simulation result prove that all trigger and guidance mechanism work properly. When the thin-walled tube crushed progressively kinetic energy of car absorbed by primary energy absorbers as shown in Figure 5.14 d, e and f , velocity of system reached to zero.

5.4 Crush Zone Integration to the Conventional Passenger Car

To integrate the crush zone to the conventional passenger car model, the end of the car is modified, the fixed sill is attached by rigid beam elements to the main underframe beams at the unoccupied end of the passenger car model. The underframe of conventional passenger car is designed as very stiff to carry the high draft forces. The stiff end of passenger cars withstands to high acceleration/deceleration rates and lateral buckling during collisions. The CEM system is designed to collapse in a controlled manner and with prescribed forces during collisions. Distributing the crush load and absorbing the kinetic energy at the unoccupied ends of passenger cars minimize the passenger injuries and unpredicted damages (see Figure 5.15).

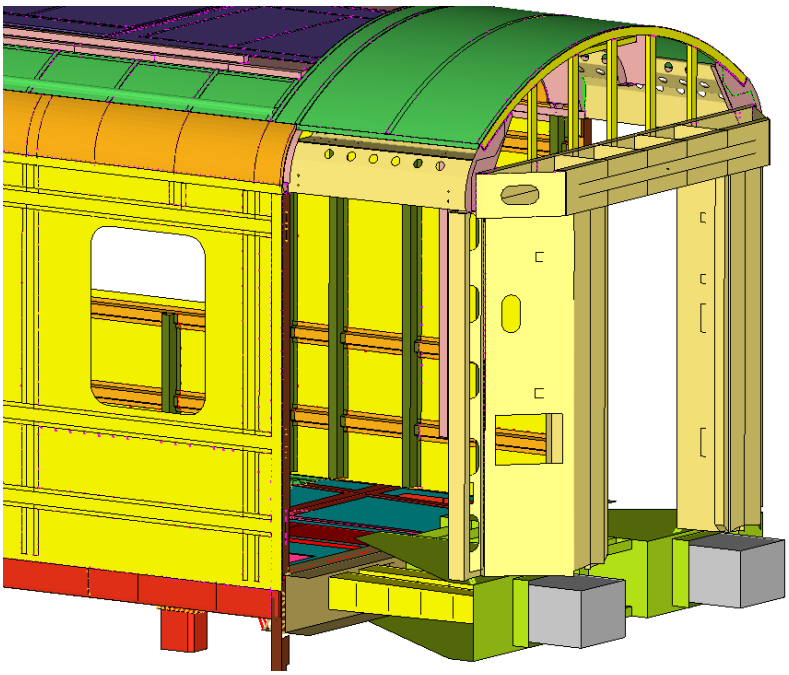

Figure 5.15 : The end part of the passenger car with an integrated crush zone.

5.5 Stress Analysis of Passenger Car Integrated with CEM System Under Static Loading

Before the railway car was allow to circulate, a series of static tests had to be carried out. According to following international standards stress analysis has been conducted.

- EN 12663- Structural requirements of railway vehicle body
- UIC leaflet 577
- ERRI B12/RP17 report (European Rail Research Institute

Based on the above mentioned standards railway car must resist three loading cases which are 1970 kN compression force, 481 kN diagonal compression force and 1472 kN tensile force. Figure 5.16 shows loading cases schematically. After the finite element model has been developed, the weight of passengers and additional equipment weight about 18 tons have been added to the model with lumped mass method. The gravity field applied to all elements that have mass. In an actual railcar, motion in the lateral direction is prevented by the flanges of the wheel contacting the rail. The boundary conditions are applied to the model as closely match the condition applied to the railcar during an actual compressive strength test. The motion of railway car restricted in vertical direction from the bogies location.

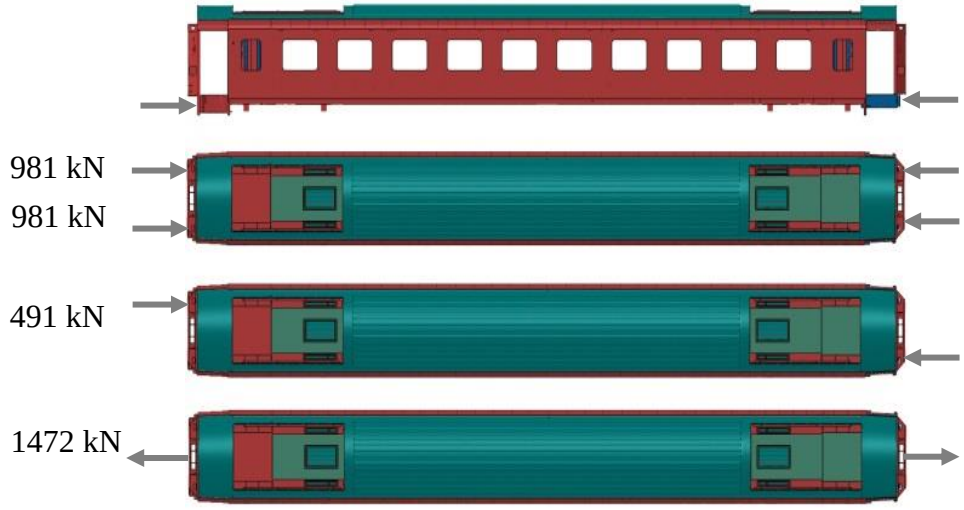

Figure 5.16 : Schematic loading in static simulation [94].

The von Mises stress distribution of CEM car under gravity load and 1962 kN longitudinal compression load has been showed in Figure 5.17, the compression load acts entirely in the longitudinal direction in the model. The carbody can be treated as a single beam with two single supports on the bogies. Gravity is a uniformly distributed transverse load. In a simple beam subject to a transverse load, the transition from positive longitudinal stress to negative longitudinal stress occurs at the neutral axis. The longitudinal displacement is investigated along the height of the car wall for various distances. The average neutral axis height is found to be

approximately 70 cm above the floor. When the car compressed longitudinally, because the buff stops on passenger car are located below the effective neutral axis, a compressive load at this location induces a bending moment within the carbody. The longitudinal compressive load will contribute to the stress state in the car during only under gravity load. As shown in Figure 5.17 the maximum von Mises stress occur in elements which simulate shear bolt connection between sliding sill and fixed sill. Node to node connection in FE model causes the stress concentration in this element. In real bolt connections this high stress state does not happen. In other area of carbody the maximum von Mises stress is around 278 MPa. This prove that passenger car design integrated with crush zone system stands the compressive load (see Figure 5.18).

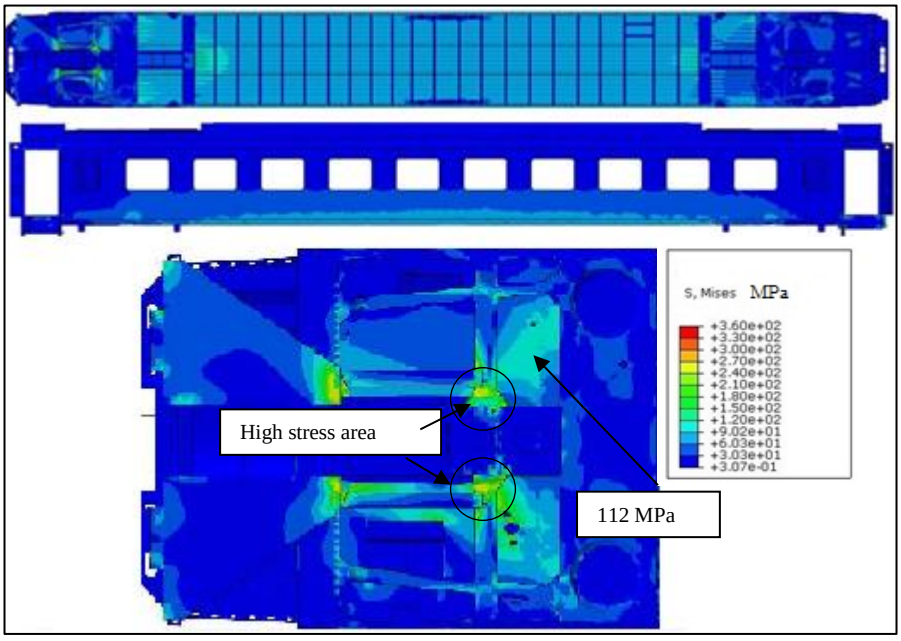

Figure 5.17 : Von Mises stress distribution for compression force of 1970 kN.

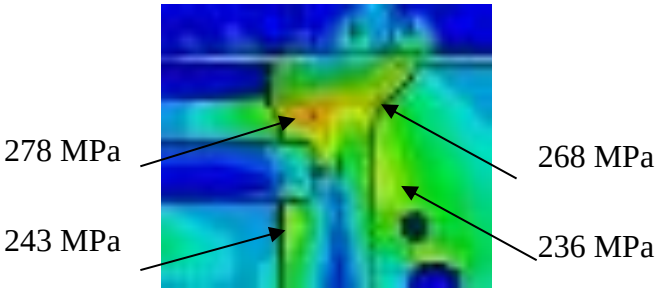

Figure 5.18 : Von Mises stress distribution, compression force in high stress area.

In diagonal compressive loading of passenger car, the car body loaded diagonally from buff stops with 491 kN. When the car is under gravity load and diagonally

compressed on longitudinal, the carbody undergo compression, bending and twisting simultaneously. The von Mises stress distribution is shown in Fig. 5.19. the high stress distribution occur on half portion of car, where the car is loaded. In this loading system the maximum stress happen in shear bolt connecting elements and other area the maximum von Mises stress is around 268 MPa (see Figure 5.20). This prove that passenger car design integrated with crush zone system stands the diagonally compressive load.

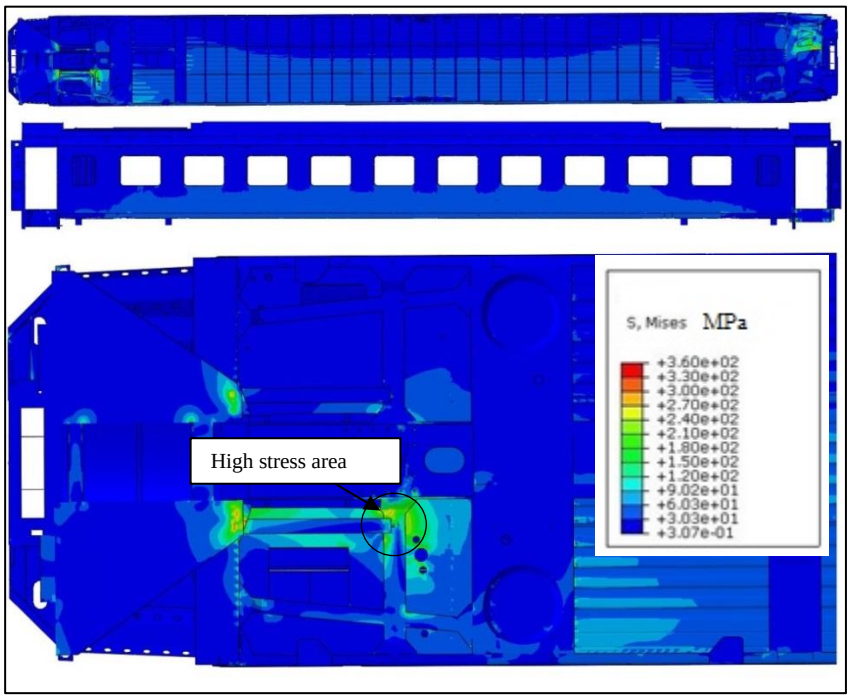

Figure 5.19 : Von Mises stress distribution, diagonal compression force of 491 kN.

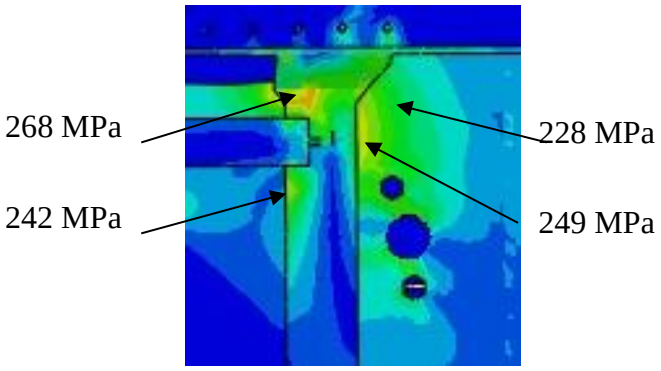

Figure 5.20 : Von Mises stress distribution, diagonal force in high stress area.

Once the tensile load acts entirely in the longitudinal direction in the model. The carbody is subjected to transverse gravity load and longitudinal tensile load. The tensile force acts on the center of underframe on the head of car. By considering the car as single beam, under the uniformly distributed transverse gravity force, positive

stress occurs under the neutral axis and negative stress above the neutral axis. When the car tension longitudinally, because the loading area on passenger car are located below the effective neutral axis, a tensile load at this location induces a bending moment within the carbody. The longitudinal tensile load contributes to the stress state in the car when it was only under gravity load. As shown in Fig. 5.21 the maximum Von Mises stress occur in elements which simulate shear bolt connection between sliding sill and fixed sill. Node to node connection in FE model causes the stress concentration in this element. In real bolt connections this high stress state does not happen. In other area of carbody the maximum Von Mises stress is around 304 MPa (see Figure 5.22). This prove that passenger car design integrated with crush zone system stands the tensile load.

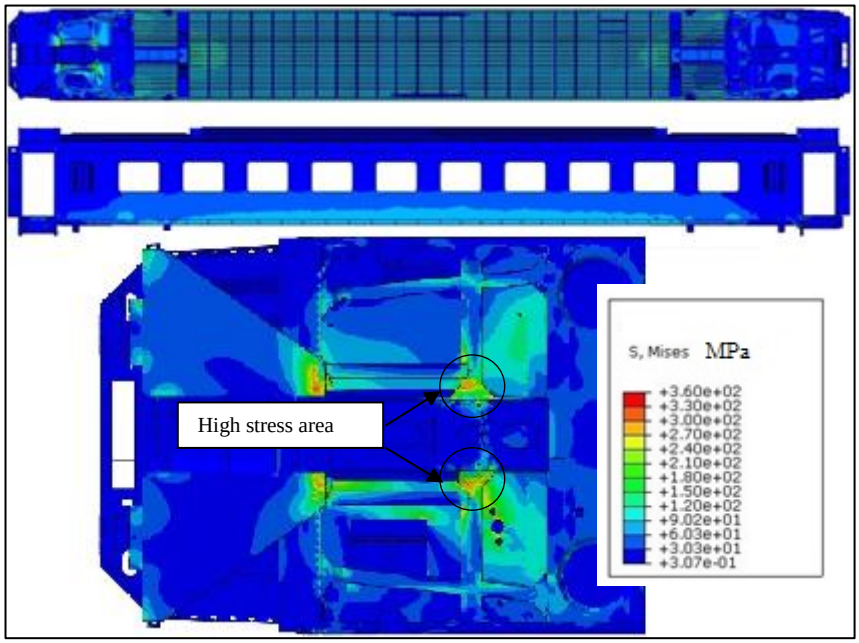

Figure 5.21 : von Mises stress distribution for tensile force about 1470 kN.

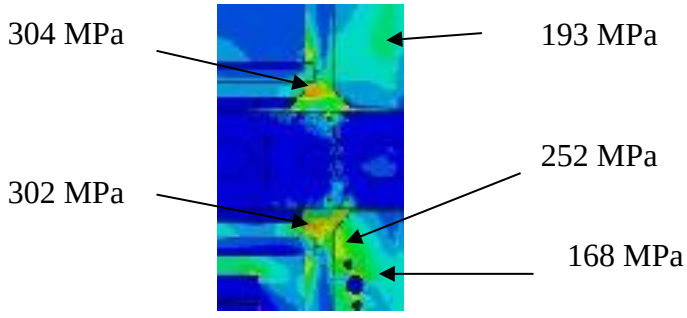

Figure 5.22 : Von Mises stress distribution for tensile force in high stress area.

In sum, the FE results of static loading are demonstrated that the passenger car with integrated CEM system is durable under static loading. In some local area on the car

Von Mises stress reaches to the yield stress of the material. These area are the nodal connections of Bond elements which are employed to simulate the bolts connections.

5.6 Dynamic Analysis of Passenger Car Integrated with CEM System Under Impact Loading for 50 km/h

During this simulation, the passenger cars having the CEM system is impacted to a fixed rigid wall at 50 km/h. The kinetic energy of the passenger car is approximately 2.35 MJ in 50 km/h velocity. The specific objectives for this collision simulation, in order to evaluate the improvement of crashworthiness, are as follows: a) measure the force-crush behavior of the end structure, b) measure the acceleration-time history of the passenger car, c) measure the gross motions of the passenger car, d) verify that triggers and crushable elements perform as designed and e) observe the primary modes of the deformation.

In the collision simulation of the passenger car having the CEM system, the crush zone is activated in the impact with a rigid wall and crushed in a progressive and controlled manner, as it is designed. Figure 5.23 shows the stress distribution in passenger car having CEM for 50 km/h impact into a rigid wall. Figure 5.24 shows the passenger car having the CEM system as end crash deformation progresses via underframe views. As can be seen, the crush is constrained to the crush zone. Figure 5.25 shows the half of primary energy absorber elements inside of crush zone. It is clear that the pyramidal tubes crashed in progressive stabile manner under impact.

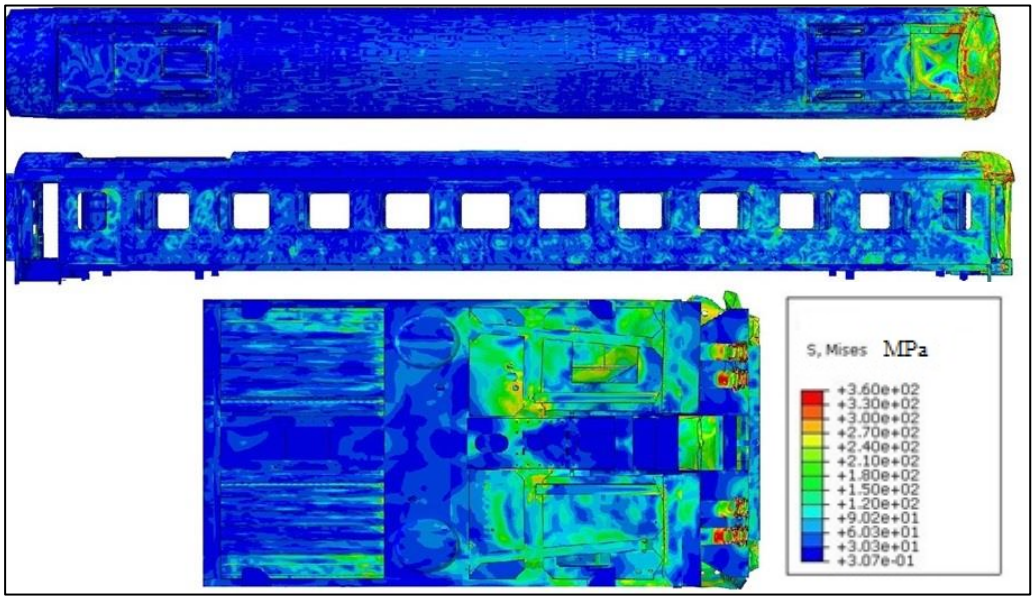

Figure 5.23 : The stress distribution in passenger car with CEM for 50 km/h impact.

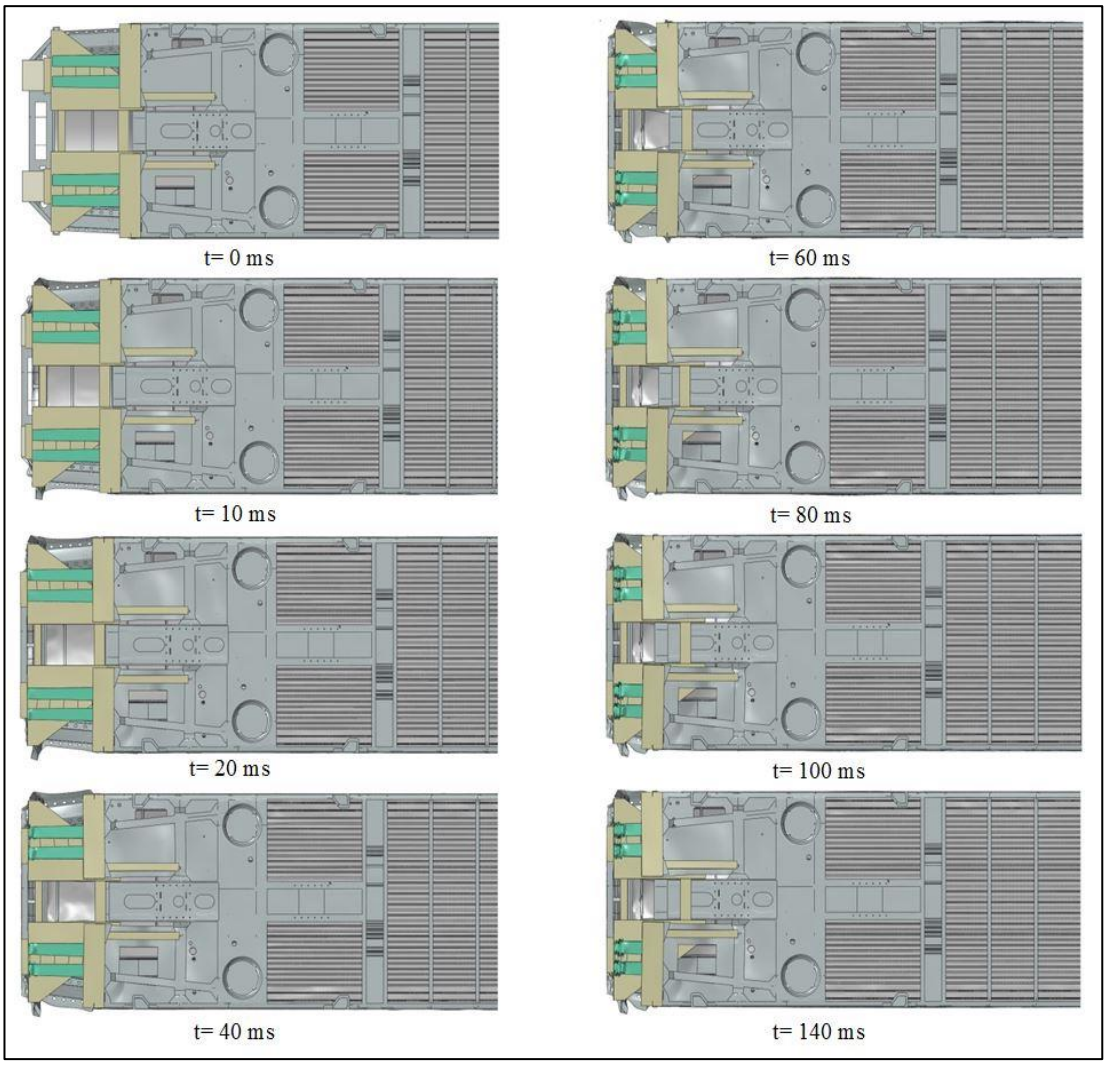

Figure 5.24 : Under-frame views of the CEM passenger car with 50 km/h.

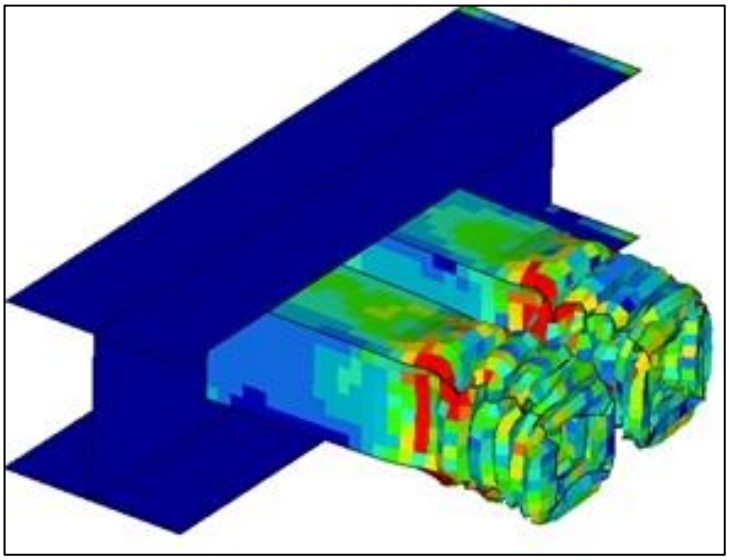

Figure 5.25 : The deformation of tubes in the crush zone (50 km/h).

Figure 5.26 shows the force-crush behavior of the passenger car having the CEM system during impact with 50 km/h to a rigid wall. The load path moved through the crush zone as predicted and triggered the crush of the each energy absorbing components. Upon impact of the passenger car to the rigid wall, the load path initially triggered the shear bolts of the honeycomb structure box. The honeycomb structure is crushed with a constant force until the body and roof of the car comes into contact with the wall. When the density of the honeycomb structure reaches over 70-80%, the impact load is transferred to the sliding sill shear bolts. Before failing of the shear bolts, the impact load reached to the initial high peak; then, primary energy absorber elements (i.e., thin walled tubes) are activated. As can be seen, one element of primary energy absorber that consists of two thin walled tubes is attached together. In sum, the tubes crush in a progressive manner. For full collapse of the energy absorbers, about 2.2 MJ energy must be dissipated.

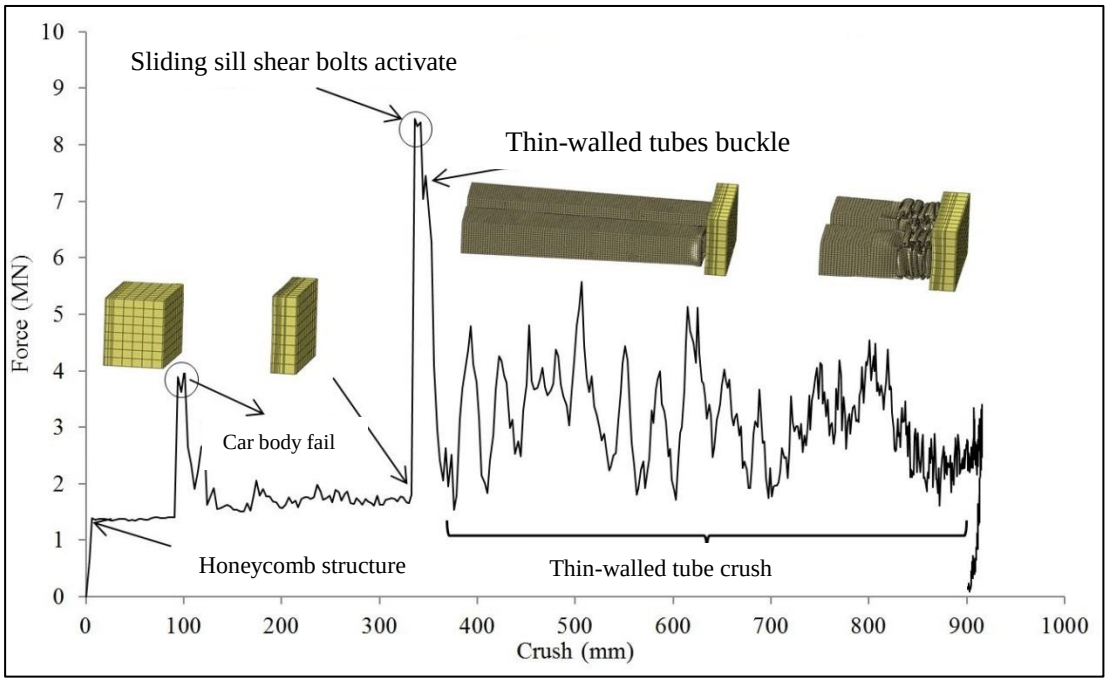

Figure 5.26 : Force-crush behavior of the CEM passenger car (50 km/h).

5.7 Investigation of the Accuracy of Numerical Simulation of Collision

To investigate the accuracy of numerical simulation of collision, it is necessary to determine the energy balance of the numerical simulation [93]. The following energy balance equation is used in collision simulations

$$E_I + E_{KE} + E_{FD} + E_V - E_{SW} = E_{TOT} \quad \textbf{(5.16)}$$

where E_I is the internal energy including the sum of the recoverable elastic strain energy, energy dissipated through plasticity, artificial strain energy and energy dissipated through distortion control; E_{KE} is the kinetic energy; E_{FD} is the dissipated frictional energy; E_V is the dissipated viscous energy and E_{SW} is the sum of the work done by the external loads (i.e., the gravity load), contact penalties, constraint penalties and propelling added mass.

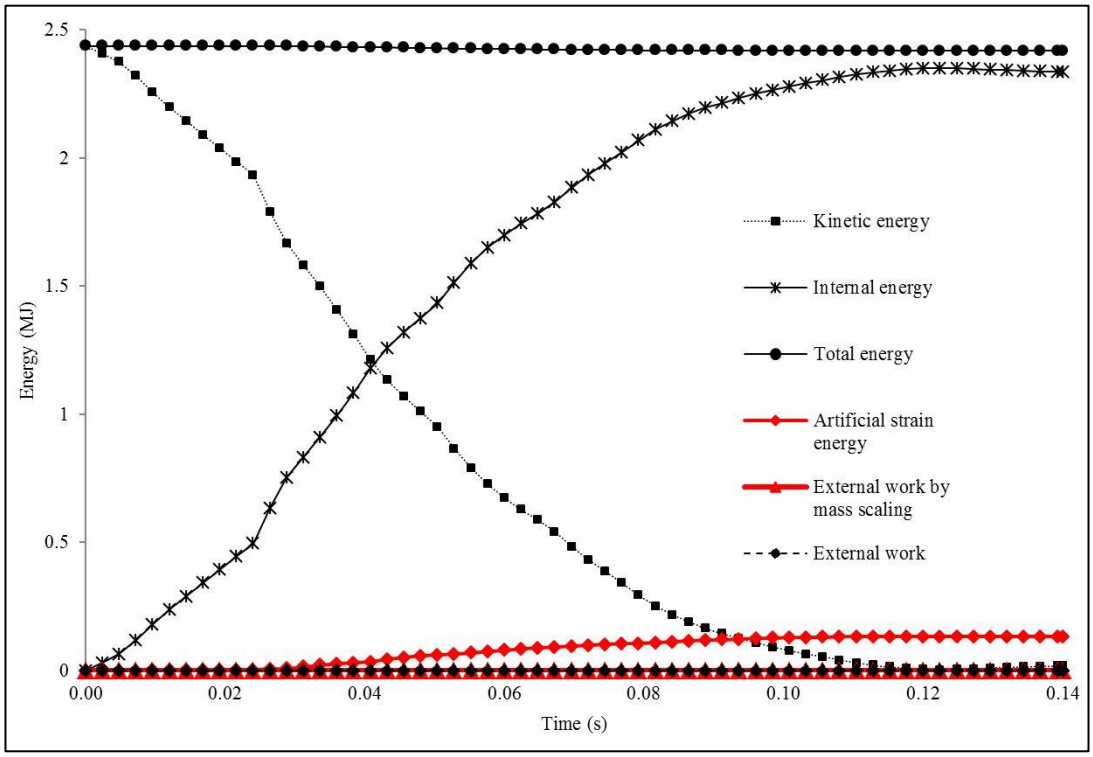

Figure 5.27 : Analysis of the energy balance for CEM passenger car simulation (50 km/h).

As a result of analyses, all energy components including the change in total mass due to artificial mass scaling are examined. Figure 5.27 shows the sum of all energy components E_{TOT} which is calculated by using Equation (5.16) and some selected important energy components such as the kinetic energy E_{KE}, internal energy E_I, artificial strain energy, external work by mass scaling and work done by the external loads during the collision analysis. In FE explicit models, if total energy is approximately constant, the total numerical error is generally less than 1% [82, 94]. As can be seen in Figure 5.27, the total energy remains constant, that is the verification of the collision analysis results and indication of that the kinetic energy

transforms into the internal strain energy during the simulation interval. According to the ECE R66 standard, the permissible amount of nonphysical energy components (i.e., hourglass energy) should be maximum 5% of the total energy [94]. Hence, it is also observed that the artificial strain energy, which includes the stored energy in hourglass resistances and transverse shear in shell elements is very small in comparison with the total energy and in the acceptable range. In addition, it is controlled by changing the mass scaling values such that the total mass due to artificial mass scaling is not altered more than 0.3% and the external work by mass scaling is negligible (i.e., see Figure 5.27).

5.8 Comparison of Impact Results for CEM and Conventional Car for 50 Km/h

5.8.1 Force-crush characteristics for 50 km/h impact velocity

The comparison between the crashworthiness results of two types of passenger car on a solid ground will prove the effectiveness of the CEM system. To this end, Figure 5.28 shows the post-impact views of the passenger cars with and without the CEM system. In the corresponding collision simulation of the conventional passenger car, large lateral buckling is observed on the occupied volume of the passenger car as seen in Figure 5.28 (c) and (d). The conventional passenger car has significant vertical motion which is as a result of the deformation by the side sills. The photographs in Figure 5.28 (a) and (b) show the passenger car having the CEM system in which the damage is limited to the unoccupied volume and would not laterally buckle under collision forces. The CEM system's collision energy is absorbed in a more efficient manner through the controlled collapse of primary energy absorbers and triggers to provide improved occupant protection. The FE results demonstrate that the CEM design approach has superior crashworthiness performance over the conventional passenger car design. There is no damage out of the crush zone area that is the first one meter of the car. By employing longitudinally crushable elements in the CEM system, the crush is engineered to remain in-line and reduces the vertical motion.

The distinctions between the conventional passenger car and the one having the CEM system are also demonstrated in force-crush diagrams, which are shown in Figure 5.29. The conventional passenger car structure is constructed by a strong under-frame. As shown in the diagram, this structure requires a high peak force to

initiate the damage. This high peak force causes a high level of deceleration on passengers. When 500 mm crush happened, there is a little resistance to further deformation.

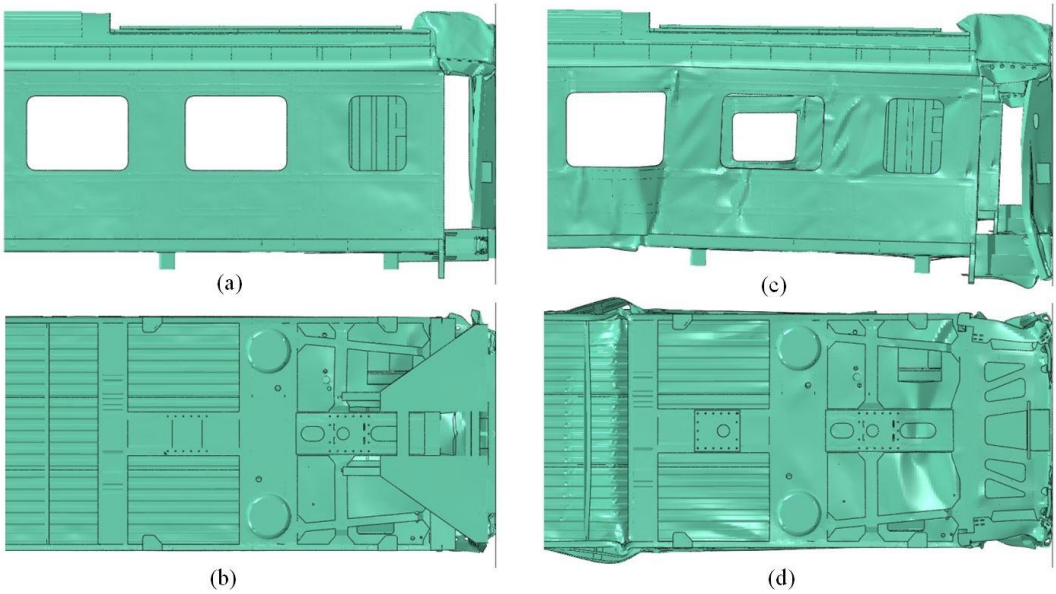

Figure 5.28 : Post-impact views: (a) side view of CEM car (b) underframe view of CEM car, (c) side view of conventional car, (d) underframe view of conventional car for 50 km/h impact velocity.

The passenger car having the CEM system is engineered to have structures out of the occupied volume that crush at lower force levels than the underframe.

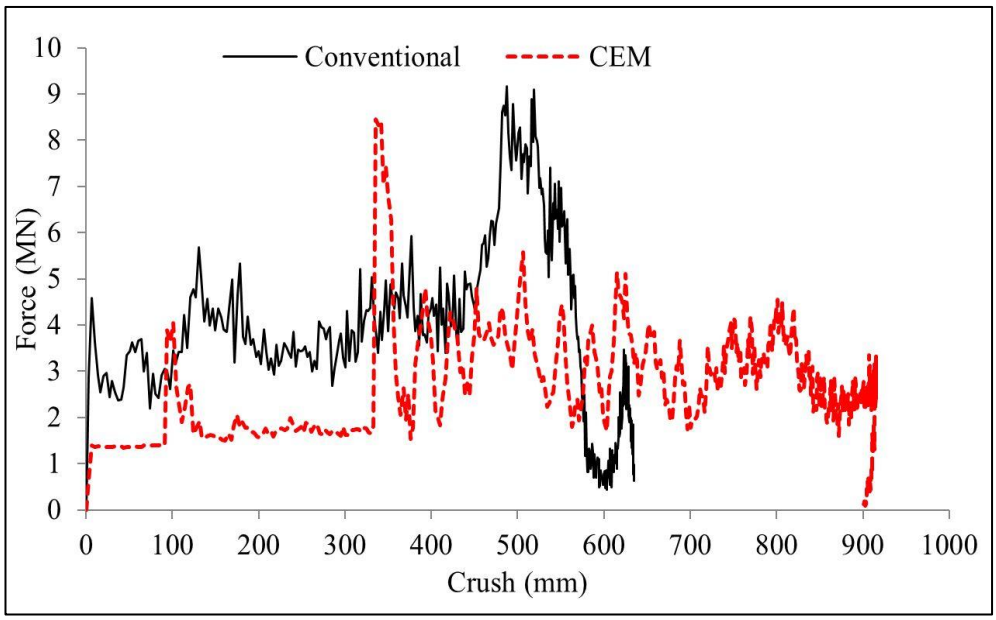

Figure 5.29 : Comparison of the force-crush characteristics for 50 km/h impact.

Then, the damage initiates in low force values, the first force peak indicates the initiation of failure for passenger car walls and roof, and the second force peak indicates the failure of shearing bolts and primary energy absorbers' activation. The primary energy absorber elements crush with an average crush load during the progressive collapse.

5.8.2 Shock tolerance of the human body

Acceleration history of occupant volume of passenger car is an important data to evaluate the crashworthiness performance of CEM system on railway passenger car. In crashworthiness studies it is necessary to investigate the occupant response to mechanical shocks. From crashworthiness point of view, in order to reduce the damage to occupants in a collision beside dissipation of kinetic energy; the acceleration of the striker must be taken account. Transitional acceleration and the duration of impulse influence directly the injury intensity of occupants. Low accelerations are desired to avoid chest and head injuries in vehicle accidents. In this study the acceleration-time history of the passenger car is considered to evaluate the crashworthiness features of cars. In order to reduce the acceleration level for a typical impact velocity .the structure must be significantly flexible. By reducing the acceleration, it is prevented to transfer the excessive acceleration loads to the occupant.

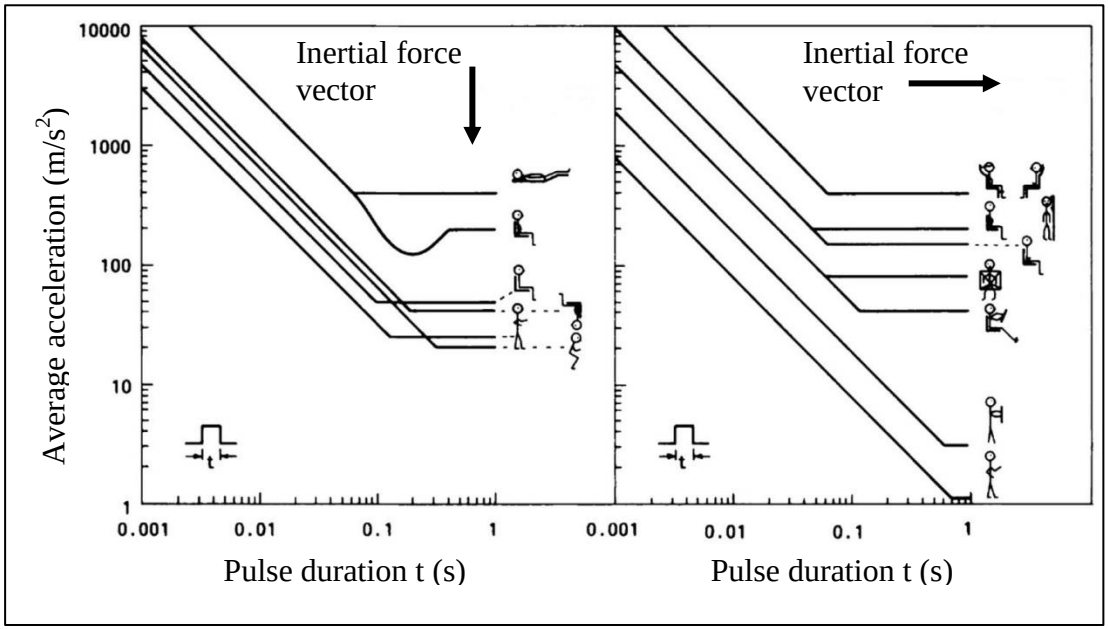

Figure 5.30 : Shock tolerance of the human body [95].

A mechanical shock occurs if the force, position, velocity or acceleration experienced by the human body changes in a time shorter than the natural response period of the body so as to cuase transient disturbances.

Studies of human tolerance to rapid increases in acceleration have been largely stimulated by occurrence of automobile accidents and the need to eject pilots from fast-flying aircraft. Many different approaches to assessing shocks have been proposed. Eiband (1959) by reviewing some early literature concluded that tolerance depended on the shock direction, magnitude, onset rate, duration and the restraints provided for the body. Griffin reproduced some examples of human body tolerance limits as figure and table. Limits of this type generally indicate that response is dependent on the peak, or average acceleration when the duration exceeds some critical value. At shorter durations the limit corresponds to the peak, or average, velocity (i.e. the acceptable peak, or average, acceleration increases in proportion to decreases in the shock duration). The magnitudes of the limits and the critical durations depends on the assumed shock shape as well as on the direction of the shock and the posture of the subject [95].

Realistic shocks causing injury never have simple shapes. The peak acceleration of the shock may be determined by very high frequency movement which may have little injury potential and will be greatly affected by the frequency response of the accelerometer mounting, the transducer and the signal conditioning. In some fields, standardized filtering has been defined to reduce these problems. The duration of the shock may also the difficult to determine, especially if there is not a single dominant peak in the acceleration record [95].

5.8.3 Acceleration-time histories for 50 Km/h impact velocity

Figure 5.31 shows the time history of the longitudinal deceleration of the geometric center of occupant volume. In order to produce meaningful comparisons, SAE filtering is done within the ABAQUS/Viewers post-processing program. The average deceleration, which is more closely related to occupant response is approximately 10.88 g for the passenger car having the CEM system and 15.5 g for the conventional passenger car. High level of acceleration influences the SIV of occupants. The larger average acceleration or the longer acceleration peak causes the faster train velocity reduction and higher SIV is generated, consequently, more serious injuries arise.

According to EN12663, a general acceleration/deceleration level which an unrestrained passenger can be expected to survive is limited to around 5g, but not more than 8g. in this acceleration/deceleration level the integrity of the attachment of equipment and fittings is preserved [93]. Based on curves showed on Figure 5.30, shock tolerance of the human body in standing posture and without restraint, with pulse duration near to 0.1 s is 7 m/s^2. The average acceleration in car with CEM system, is about 15 times higher than safe shock. The average acceleration for conventional car is 22 times higher than safe acceleration for standing passenger without restraints. The safe acceleration limit for seating posture without restraints with pulse duration near to 0.1 s is 110 m/s^2. The average acceleration in car with CEM system, is safe area but the average acceleration for conventional car is 14% higher than safe acceleration limit. The safe acceleration limit for seating posture with restraints with pulse duration near to 0.1 s is 140 m/s^2. The average acceleration of car with CEM system, is in safe area but the average acceleration for conventional car is 1.5 g higher than safe acceleration limit.

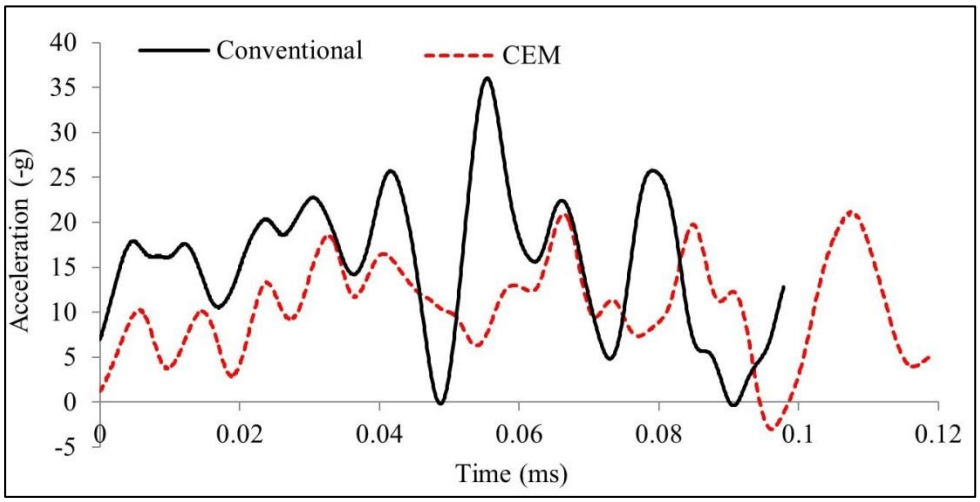

Figure 5.31 : Acceleration-time histories of the conventional passenger car and the passenger car having the CEM system for 50 km/h impact velocity.

5.8.4 Secondary impact velocity (SIV) for 50 Km/h impact velocity

The secondary impact velocity (SIV) is another factor that is investigated here to compare crashworthiness features of conventional passenger car with the passenger car having the CEM system. When an accident occurs, the passenger car deceleration causes the unrestrained passengers to impact to interior parts of passenger car or other obstacles. The secondary impact is due to these passengers who strike to interior parts of the passenger car. The SIV is the passenger's velocity relative to the

passenger car when the secondary collision occurs. The SIV is calculated from the acceleration-time history of a given passenger car's center of gravity. Integrating this data once with respect to time gives the relative velocity, and integrating twice gives the displacement used in the SIV [97, 98]. Figure 5.32 demonstrates the SIV values for the passenger car having CEM system and conventional one with 14 m/s impact velocity.

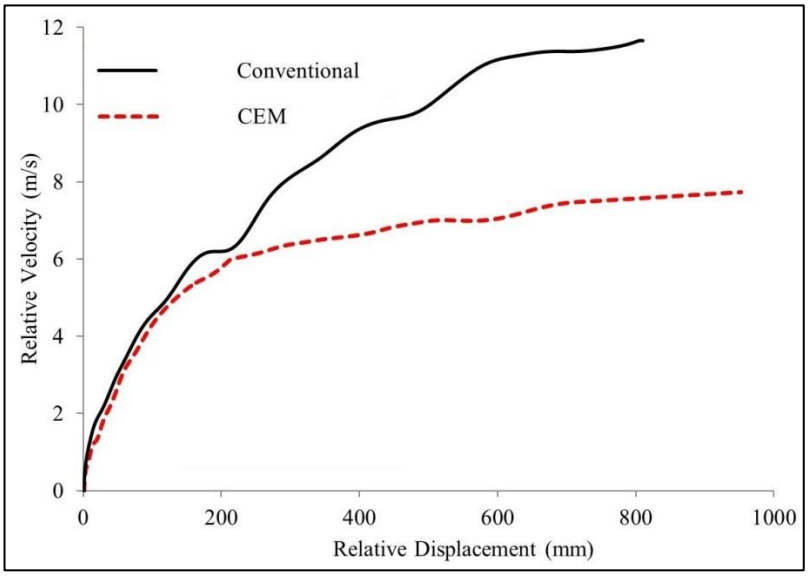

Figure 5.32 : Acceleration-time histories of the conventional passenger car and the passenger car having the CEM system 50 km/h impact velocity.

By analyzing the SIV curves for both cars it is obtained that in distances from 150mm to 200 mm (the typical distance for knees impact for seated occupants) there is little improvement in terms of SIV. In addition SIV value is important to consider in distances over 600 mm due to occupants impact with luggage and obstacles inside of compartment. In distances over 600 mm for the conventional passenger car is found to be approximately 11.2 m/s where this value for the passenger car having the CEM system is approximately 7.1 m/s. Therefore CEM system has contributed in reduction of injuries happening in distances over 600 mm.

5.8.5 Velocity-time histories for 50 Km/h impact velocity

Figure 5.3 shows the time history of the longitudinal velocities of the passenger car having the CEM system and conventional passenger car after the impact. The slope of the velocity plot shows the intensity and the timing of the collision. The conventional passenger car comes to rest in less than 100 milliseconds, whereas this time for the passenger car having the CEM system is more than 120 milliseconds.

These plots are an indication of the higher level of deceleration in the conventional passenger car in comparison with the longer deceleration time and low level of deceleration in the passenger car having the CEM system.

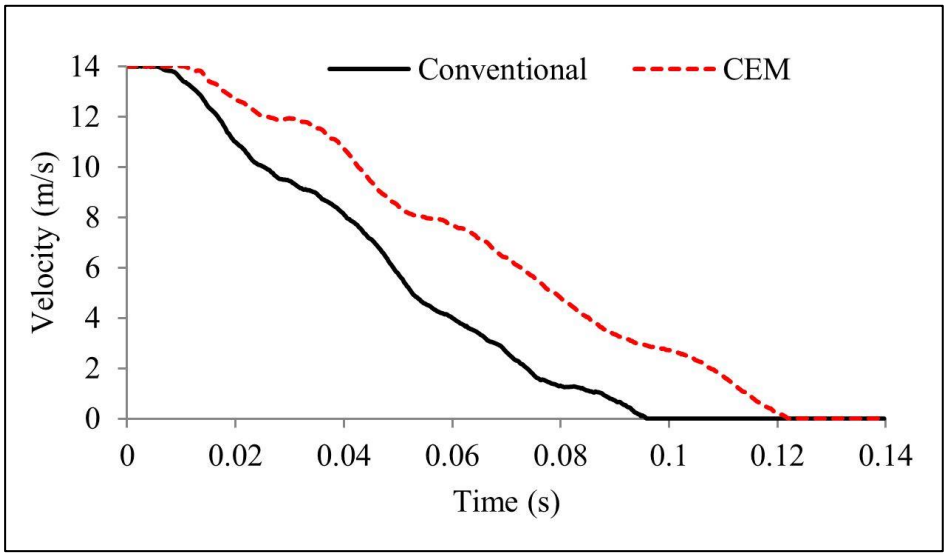

Figure 5.33 : Velocity-time histories of conventional passenger car and the passenger car having the CEM system.

5.9 Comparison of Impact Results for CEM and Conventional Car for 10 and 15 km/h

To investigate the effectiveness of CEM system on crashworthiness characteristics of passenger car on low velocities, nonlinear explicit analysis of conventional passenger car and car having CEM system have been conducted with 10 and 15 km/h initial velocities. The comparison between the crashworthiness results of two types of passenger car on a solid ground will prove the effectiveness of the CEM system. To this end, stress distribution, velocity-time and acceleration-time histories of cars have been extracted.

5.9.1 Stress distribution for CEM and conventional car for 10 Km/h velocity

Figure 5.34 and 5.35 demonstrate the post-impact views of the passenger cars with and without the CEM system for 10 km/h impact in different time steps. In the corresponding collision simulation of the conventional passenger car, high stress distribution is observed on the occupied volume of the passenger car as seen in Figure 5.34. In comparison with the conventional, passenger car with CEM has low stress distribution in carbody. Figure 5.36, shows von Mises stress changes respect to

time after 10 km/h impact with a rigid wall. To understand the stress distribution and energy absorption of passenger car structure under impact loading, it is necessary to focus on stress wave propagation and its effect on energy absorption on structure. By application of dynamic loading, the suddenly gained stress or the suddenly gained particle velocity at the points on the loaded surface will be propagated away from the surface in the form of stress waves. If the normal stress applied is smaller than the yield stress of the material, the stress wave is elastic. If the stress created by the dynamic loading is beyond the yield stress of the material, in addition to the elastic stress wave propagating , plastic stress waves will be initiated and propagate away from the loaded region. Elastic and plastic waves may affect the energy absorption of materials and structures in various complex ways, depending on the dynamic loads, the structure's configuration and the material's properties. At the dynamically loaded region, the high stress brought about by the strong plastic compression waves may cause a local plastic collapse, for example, some parts on head of passenger car plastically collapsed. After some energy has been dissipated in this localized zone, the rest of the car may experience only elastic deformation. When a compressive elastic wave produced by a dynamic load or impact reaches the distal surface, it will reflect from that surface. If the surface is free (i.e. with no constraint to its displacement), the reflected wave will a tensile one which propagate. When a compressive elastic wave produced by a dynamic load or impact reaches the distal surface where no displacement is allowed, the reflected wave will also be compressive and it will result in the magnitude of the compressive stress being doubled. The increase in the stress magnitude may create a plastic compressive wave, so plastic deformation and energy dissipation would first occur in the region close to the distal fixed surface rather than in the loading region. All the above cases usually occur when the dynamic loading is along the longitudinal direction of the structural components, if the slender structural component (e.g. a thin plate) is subjected to a dynamic loading in its transverse direction, then the stress waves along that direction will disappear in the brief time period as a result of the frequent wave reflection between two close surfaces of the plate along its thickness direction [6].

Von Mises stress changes with time has been showed in Figure 5.36 for conventional and car with CEM system. These stresses selected from the high stress region of the both car. As it is clear from the figure, after the impact during the 2.5 ms elastic

wave reaches to the element about 12ms plastic wave propagation is observed in the element. In the passenegr car with CEM system, elastic wave reaches to the element with delay in comparison with conventional one, because energy dissipated in the crush zone area. Plastic wave has not propagated in the selected element of CEM system.

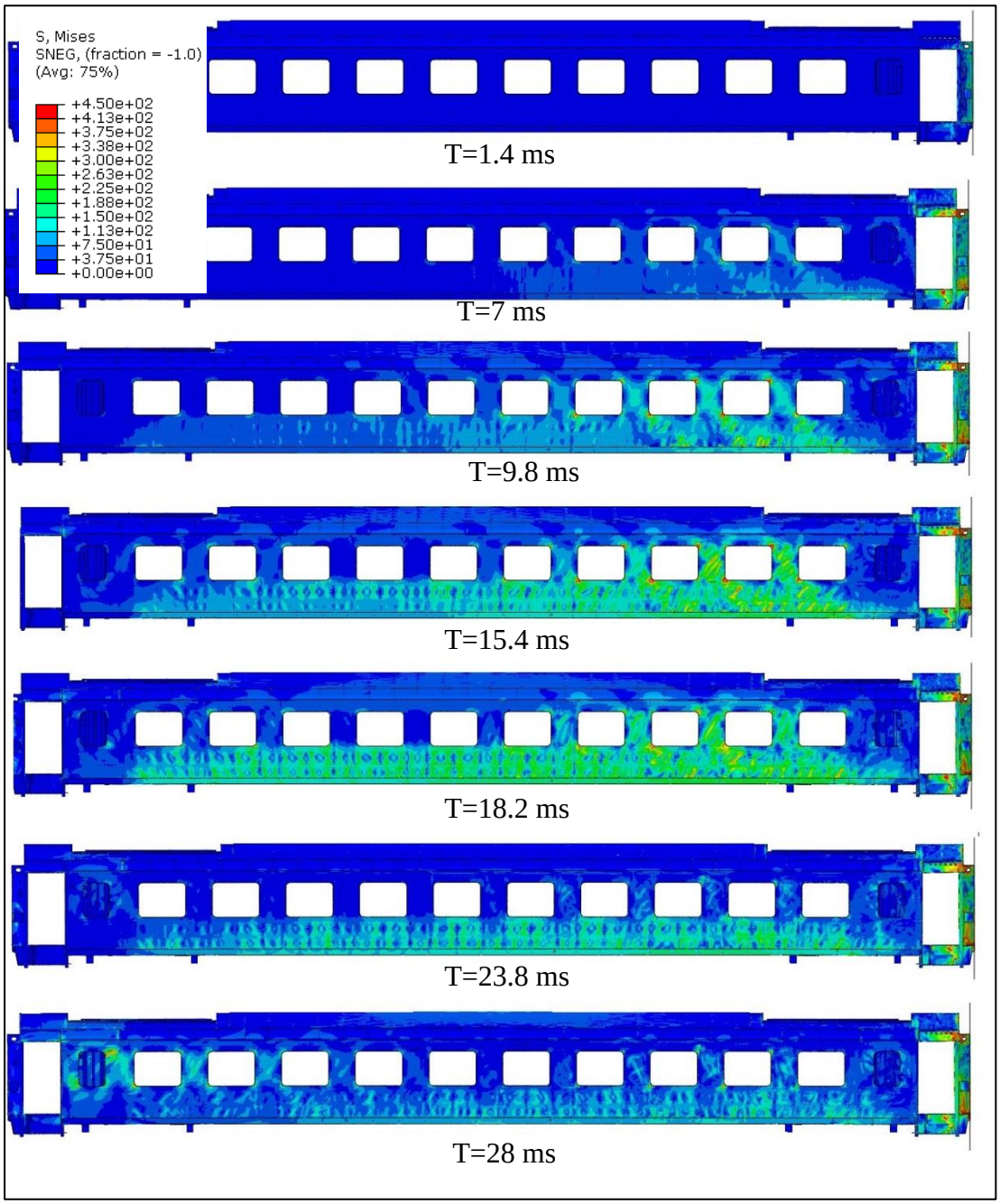

Figure 5.34 : The stress distribution in the conventional car after 10 km/h impact.

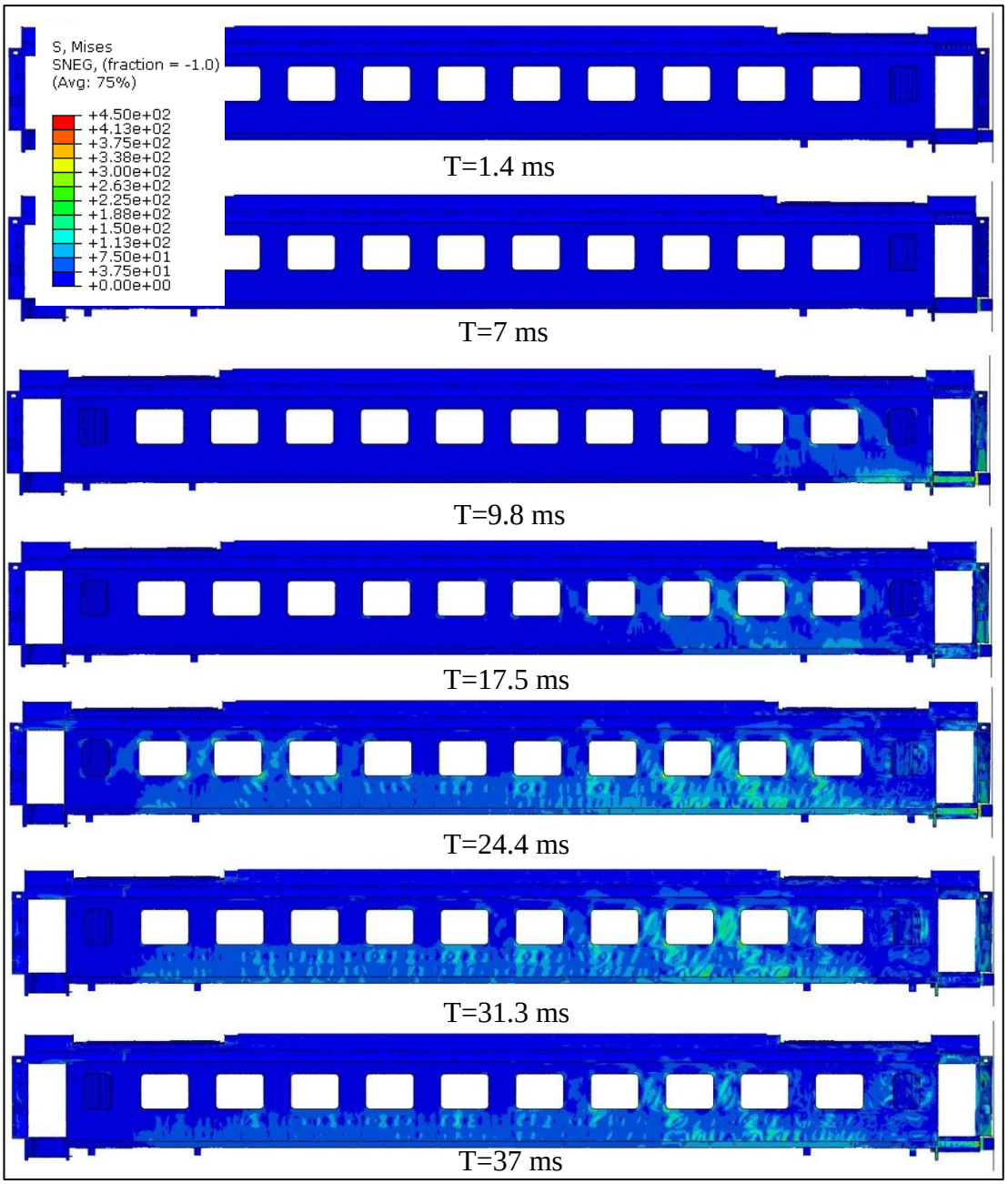

Figure 5.35 : The stress distribution in the passenger car with an installed CEM system after 10 km/h impact with a rigid wall.

Elastic wave fluctuated around 175 MPa and after 25 ms, stress drop by time. The remained stress on conventional passenger when came to rest in 28 ms is 149 MPa. The remained stress on passenger equiped with CEM when came to rest in 37 ms is 70.5 MPa.

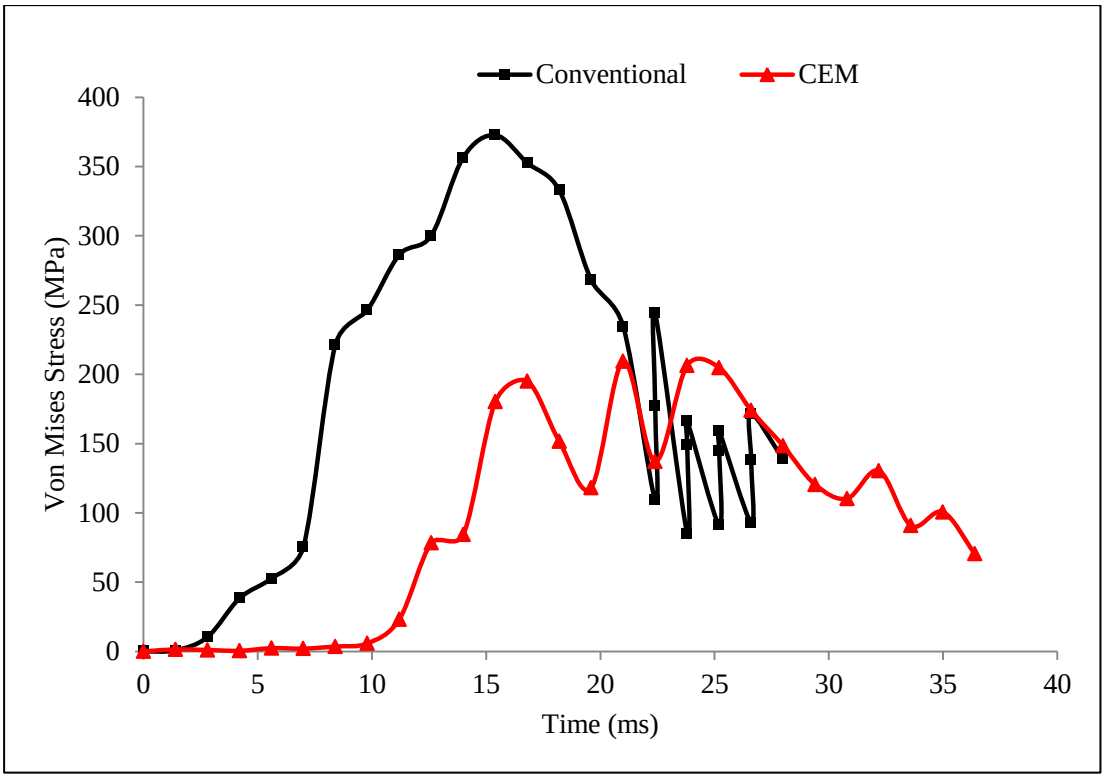

Figure 5.36 : Von Mises Stress changes respect to the time after 10 km/h impact velocity.

5.9.2 Velocity and acceleration-time histories for 10 Km/h impact velocity

Figure 5.37 shows the time history of the longitudinal velocities of the passenger car having the CEM system and conventional passenger car after the impact for 10 km/h impact respectively. The slope of the velocity plots show the intensity and the timing of the collision. The conventional passenger car comes to rest in less than 0.02 seconds in 10-km/h impact. These plots are an indication of the higher level of deceleration in the conventional passenger car in comparison with the longer deceleration time and low level of deceleration in the passenger car having the CEM system.

The time history of the longitudinal deceleration of the occupant volume for both car is shown in Figure 5.38. In order to produce meaningful comparisons, SAE filtering is done within the ABAQUS/Viewers post-processing program. The average deceleration, which is more closely related to occupant response for the passenger car having the CEM system and conventional one are approximately 5.88 g and 8.9 g respectively. According to EN12663, a general acceleration/deceleration level which an unrestrained passenger can be expected to survive is limited to around 5g, but not

more than 8g. in this acceleration/deceleration level the integrity of the attachment of equipment and fittings is preserved [94].

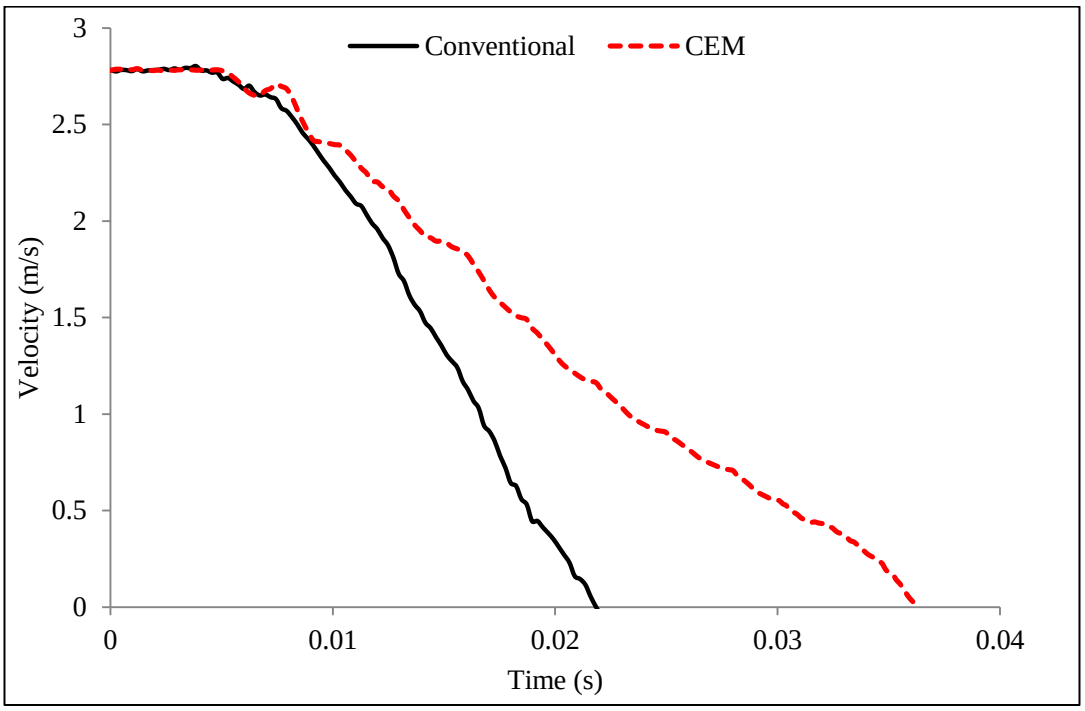

Figure 5.37 : Velocity-time histories of the conventional and the passenger car equipped with the proposed CEM system after 10 km/h impact.

The pulse duration for conventional passenger car with 10 km/ h is about 0.02 s. The safe acceleration limit for standing passenger without restraints for 0.02 s pulse duration is 40 m/s^2 ($\approx 4g$). The average acceleration of conventional car for standing passenger without restraints is near to 2.2 times higher than safe acceleration limit. The pulse duration for passenger car having CEM with 10 km/ h is about 0.03 s. The safe acceleration limit for standing passenger without restraints for 0.03 s pulse duration is 30 m/s^2 ($\approx 3g$). The average acceleration of passenger car with CEM system for standing passenger without restraints is near to 2 times higher than safe acceleration limit. The safe acceleration limit for passenger in seating posture and without restraints for 0.02 s and 0.03 s pulse duration are 130 m/s^2 ($\approx 13g$) and 120 ms^{-2} ($\approx$ 12g) respectively. Based on the these information both car with and without CEM system are in safe region from point view of shock tolerance.

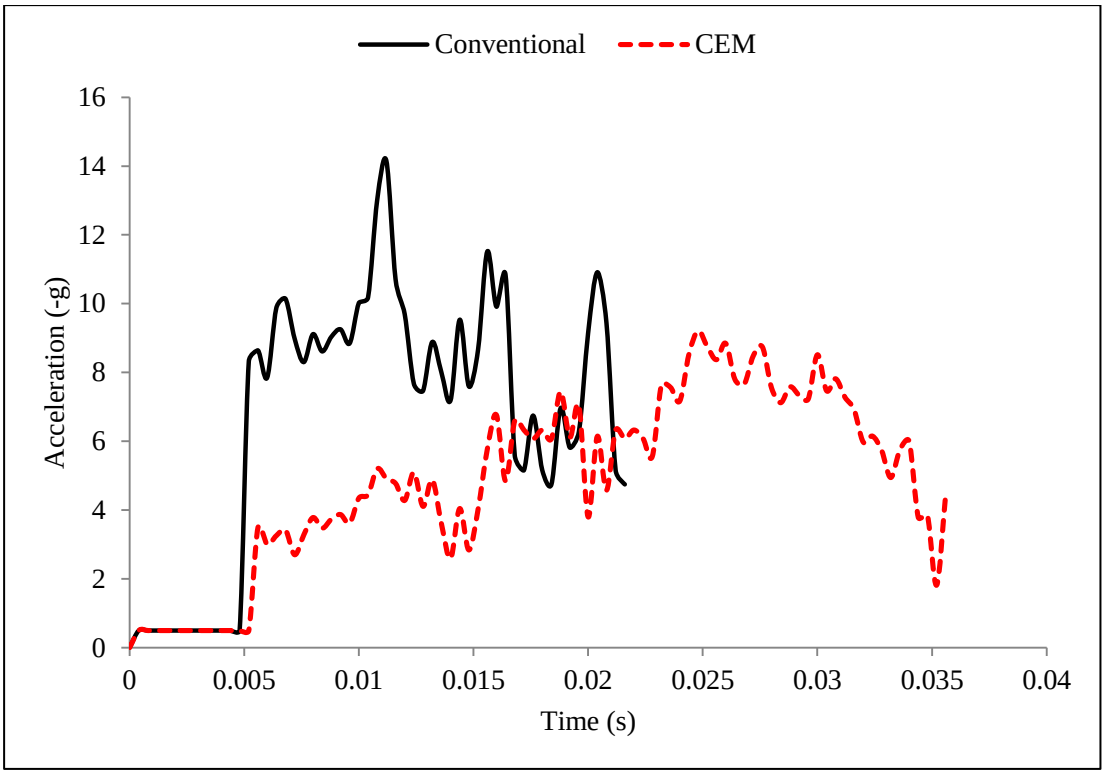

Figure 5.38 : Acceleration-time histories of the conventional and the passenger car equipped with the proposed CEM system after 10 km/h impact.

5.9.3 Stress distribution for CEM and conventional car for 15 km/h velocity

Figure 5.39 and 5.40 demonstrate the post-impact views of the passenger cars with and without the CEM system for 15 km/h impact in different time steps. In the corresponding collision simulation of the conventional passenger car, high stress distribution is observed on the occupied volume of the passenger car as seen in Figure 5.39. In comparison with the conventional, passenger car with CEM has low stress distribution in carbody. Figure 5.41, shows Von Mises stress changes respect to time after 15 km/h impact with a rigid wall. Von Mises stress changes with time has been showed in Figure 5.41 for conventional and car with CEM system. These stresses selected from the high stress region of the both car. As it is clear from the figure, after the impact, during about 3 ms elastic wave reaches to the element. About 8 ms plastic wave is observed in the element. In the passenger car with CEM system, elastic wave reaches to the element with delay in comparison with conventional one, because energy dissipated in the crush zone area. Plastic wave has reached to the selected element in 12 ms after the impact. Elastic wave in passenger car with CEM system fluctuated around 135 MPa. The remained stress on conventional passenger

when came to rest in 42 ms is 124 MPa. The remained stress on passenger equipped with CEM when came to rest in 72.4 ms is 98 MPa.

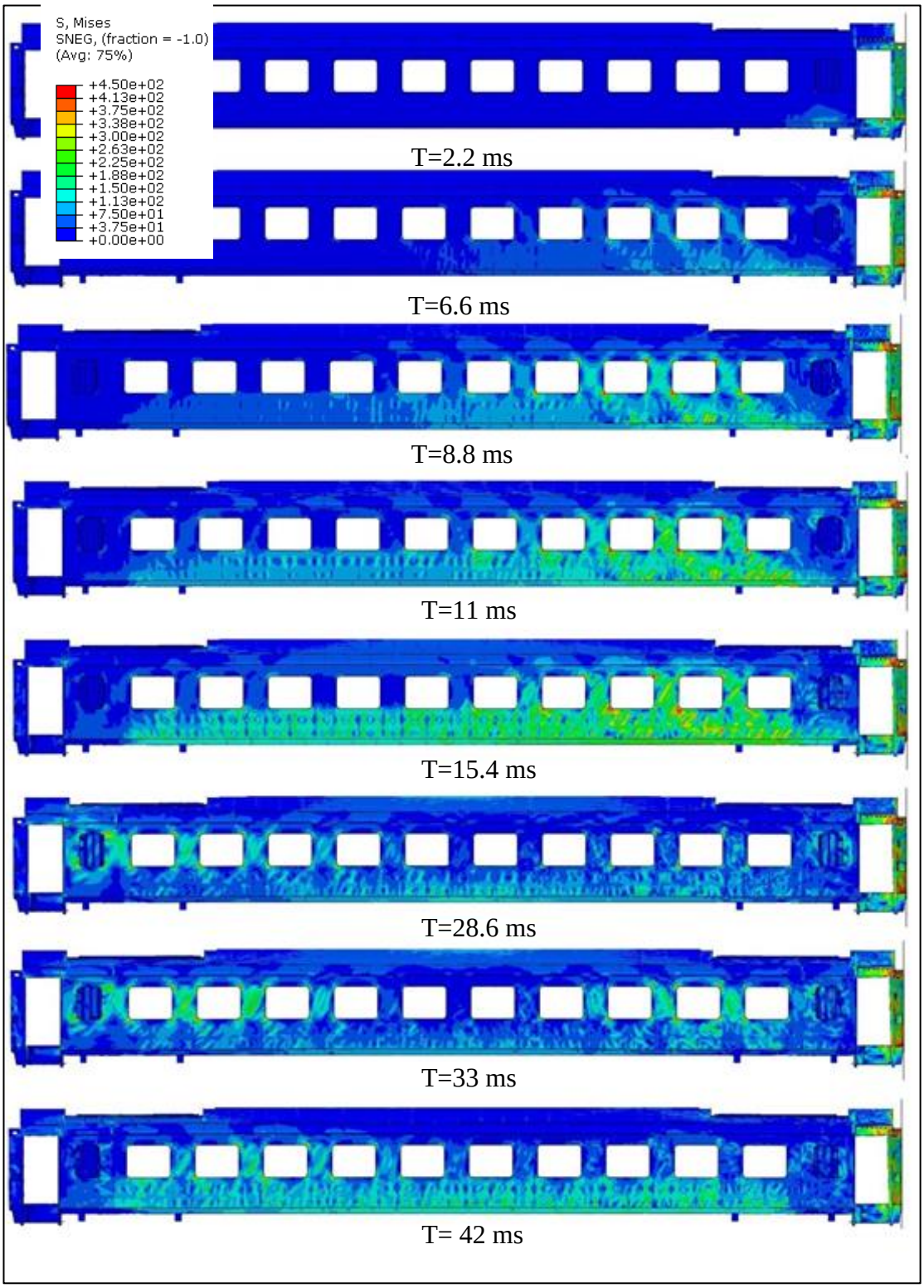

Figure 5.39 : The stress distribution in conventional car after impact with 15 km/h velocity.

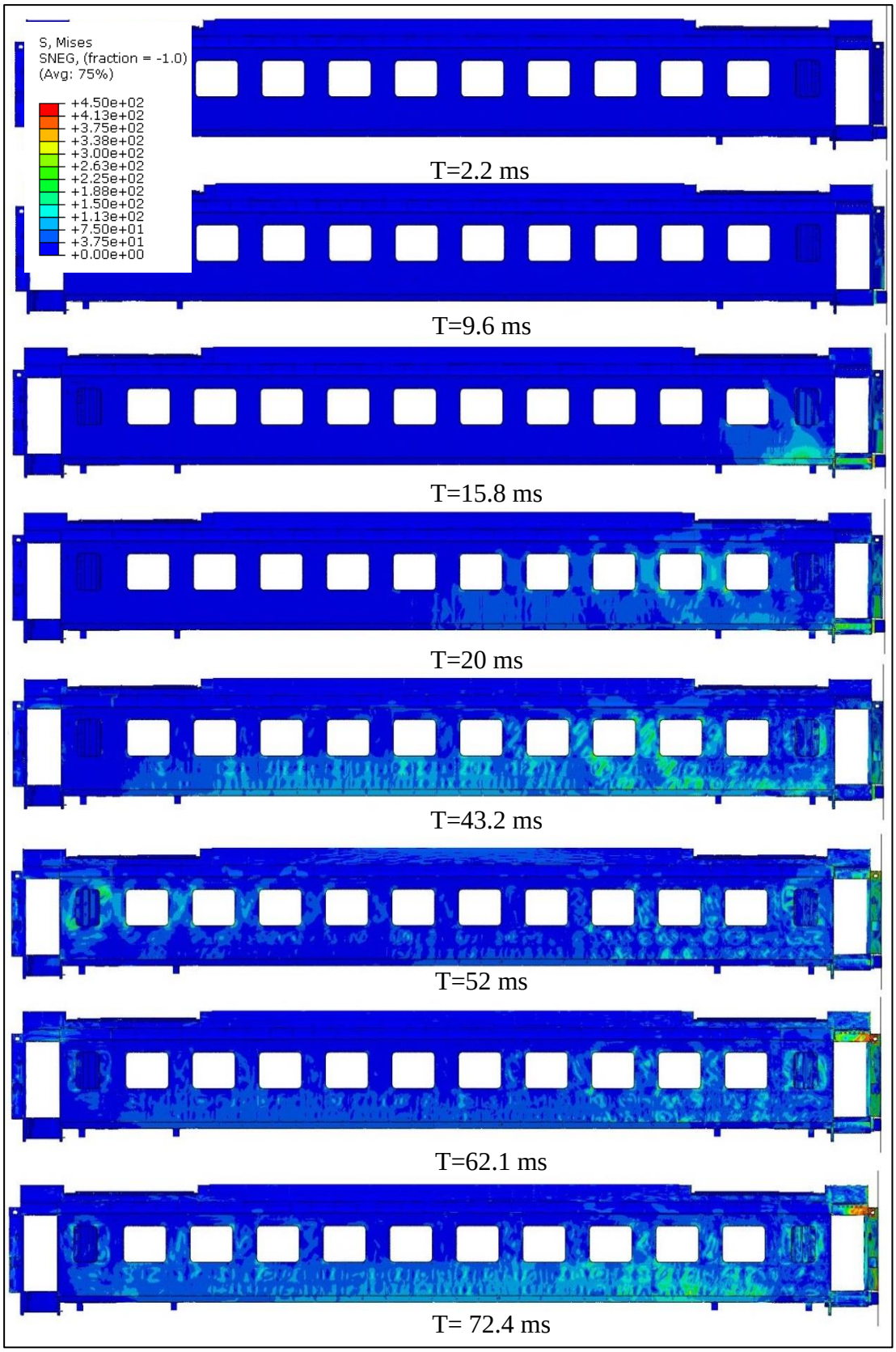

Figure 5.40 : The stress distribution in passenger car with an installed CEM system after 15 km/h impact velocity with a rigid wall.

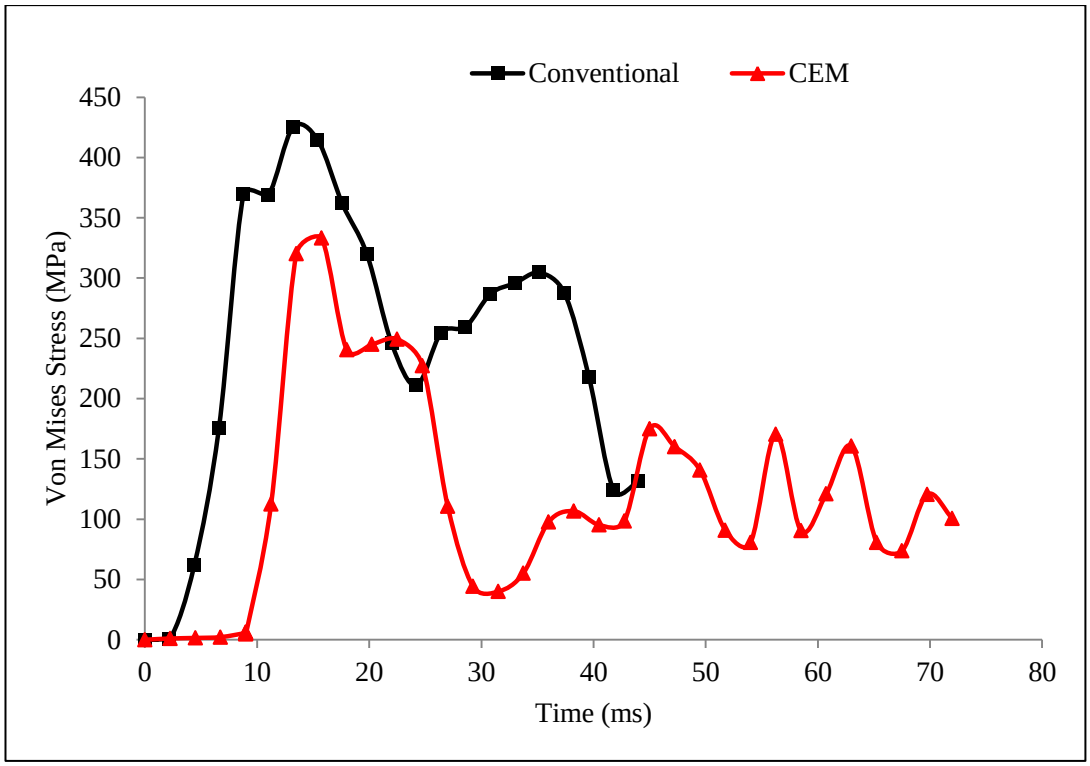

Figure 5.41 : Von Mises Stress changes respect to the time after 15 km/h impact velocity.

5.9.4 Velocity and acceleration-time histories for 15 Km/h impact velocity

Figure 5.42 shows the time history of the longitudinal velocities of the passenger car having the CEM system and conventional passenger car after the impact for 15 km/h initial impact velocity. The slope of the velocity plots show the intensity and the timing of the collision. The conventional passenger car comes to rest in 0.04 seconds after impact with initial 15 km/h velocity, whereas this time for the passenger car having the CEM system is near to 0.07 seconds after impact with initial 15 km/h velocity. These plots are an indication of the higher level of deceleration in the conventional passenger car in comparison with the longer deceleration time and low level of deceleration in the passenger car having the CEM system.

Figure 5.43 shows the time history of the longitudinal deceleration of the occupant volume for conventional and passenger car equipped with the proposed CEM system with 15-km/h initial impact velocity. In order to produce meaningful comparisons, SAE filtering is done within the ABAQUS/Viewers post-processing program. The average deceleration, which is more closely related to occupant response are approximately 6.2 g and 9.9 g for the passenger car having the CEM system and conventional one respectively.

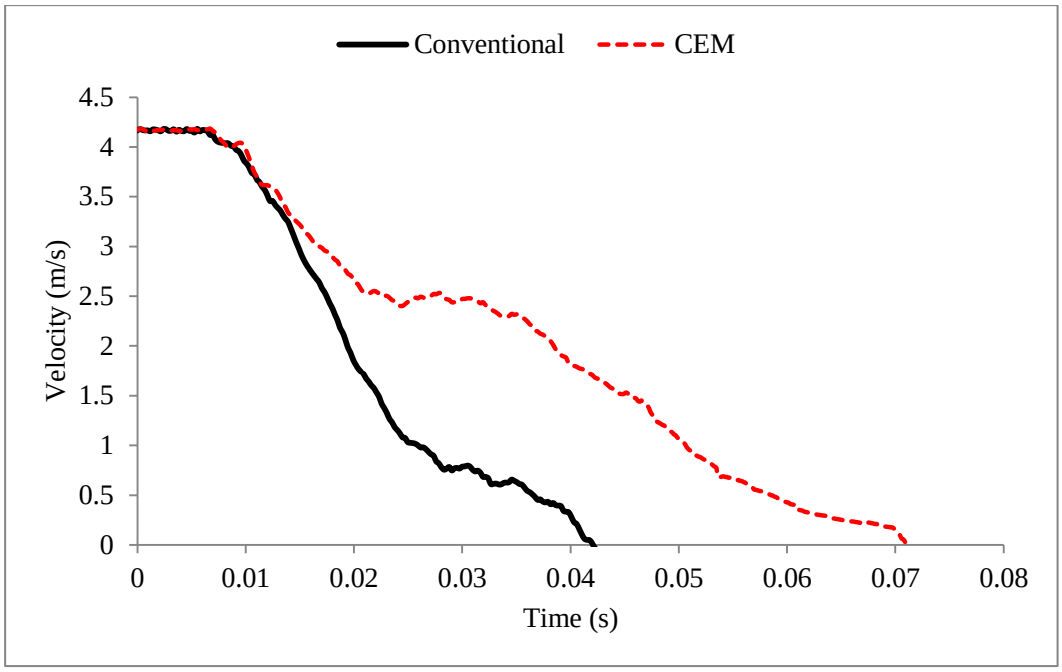

Figure 5.42 : Velocity-time histories of the conventional and the passenger car equipped with the proposed CEM system after 15-km/h impact.

High level of acceleration influences the SIV of occupants. The larger average acceleration or the longer acceleration peak causes the faster train velocity reduction and higher SIV is generated, consequently, more serious injuries arise. According to EN12663, a general acceleration/deceleration level which an unrestrained passenger can be expected to survive is limited to around 5g, but not more than 8g. in this acceleration/deceleration level the integrity of the attachment of equipment and fittings is preserved [94]. The pulse duration for conventional and passenger car having with 15 Km/h impact are 0.04 s and 0.07 s respectively. The safe acceleration limit for standing passenger without restraints for 0.04 s and 0.07 s pulse duration are 20 m/s^2 ($\approx 2g$) and 10 m/s^2 ($\approx g$). The average acceleration of conventional car for standing passenger without restraints is near to 5 times higher than safe acceleration limit. The average acceleration of passenger car with CEM system for standing passenger without restraints is near to 6.2 times higher than safe acceleration limit. The safe acceleration limit for passenger in seating posture and without restraints for 0.04 s and 0.07 s pulse duration are 120 m/s^2 ($\approx 12g$) and 110 ms^{-2} ($\approx$ 11g) respectively. Based on the these information both car with and without CEM system are in safe region from point view of shock tolerance.

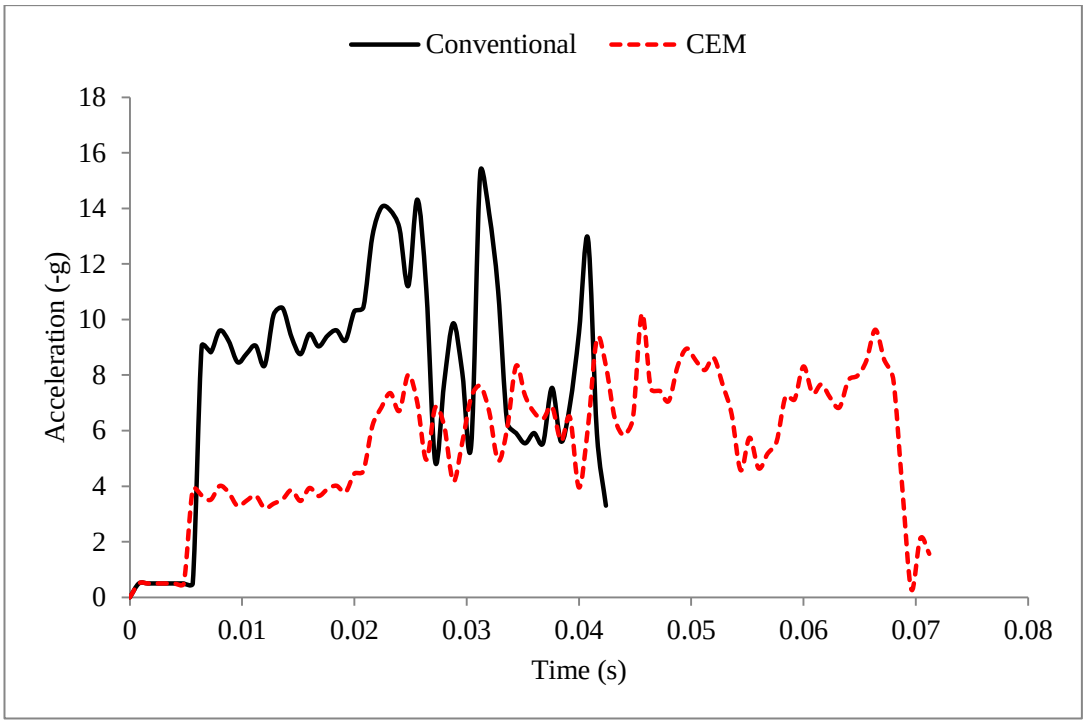

Figure 5.43 : Acceleration-time histories of the conventional and the passenger car equipped with the proposed CEM system after 15-km/h impact.

In this chapter full-scale FE simulation of conventional passenger car in collision with rigid wall is conducted. A crash energy management system has been designed. The crashworthiness behavior of crush zone is investigated by numerical simulation.then the proposed crush zone system has been applied to conventional passenger car. . In order to investigate the benefits provided by the CEM system, the full-scale railway passenger car collision with a rigid wall is simulated by using dynamic/explicit finite element (FE) methods. The force-crush, secondary impact velocity, acceleration and velocity curves, and deformation modes are computed to compare the crashworthiness performance of the CEM system with that of a conventional passenger car. Comparisons of FE analysis results show that the passenger car having CEM system has superior crashworthiness performance over the conventional passenger car [99].

6. CONCLUSIONS AND RECOMMENDATIONS

This thesis describes an innovative crash energy management (CEM) system designed for railroad passenger cars to improve the crashworthiness. The CEM system is composed of a crush zone that collapse during collision. The crush zone is located in the unoccupied ends of the passenger car and consists of shear bolts, the sliding sill mechanism, the fixed sill mechanism and energy absorption elements. The aim of a CEM system is to absorb the kinetic energy during collision of railway cars in a controlled manner and decrease the acceleration of passengers to reduce fatal injury risks. The crush zone is attached to the under-frame of passenger car by fixed sill and specially engineered to absorb collision energy of about 2.7 MJ.

6.1 Thin-Walled Tube Cross-Section Shape and conical angle and Wall Thickness Effect on Crashworthiness Characteristics

The primary energy absorber inside of the crush zone composed of thin-walled tube. In order to find the optimum design of thin-walled tube with high crashworthiness characteristic, numerical study conducted. Thin-walled tubular structures are widely used in railway and road vehicles to improve the safety of occupants during collision. The numerical simulation of thin walled tubes crushing pattern are carried out with different cross-sectional shapes. The crashworthiness characteristics of different shape are compared together. The FE simulation result reveals that multicell cross-section is effective in increasing energy absorbing factor. But in order to achieve optimum design the cell number and configuration should be investigated. The comparison results indicate that the square tube with low striker acceleration, stable deformation and reasonable energy absorption capacity is the favorable cross section geometry as energy absorption elements in passive safety issue. In order to obtain the pyramidal tube dimension with high crashworthiness characteristics, response surface methodology (RSM) and MATLAB optimization tool is used. By changing the thickness of the tube between 4 mm to 10 mm and pyramidal angle between 0º to 4.5º, it is attempted to maximize total efficiency function. The pyramidal angle and

tube thickness constraints are limited by bending buckling pattern and space restrictions on the under-frame of passenger car. The optimum pyramidal angle and thickness are obtained with 3.06º pyramidal angle with 6 mm thickness. The optimum pyramidal angle and thickness are obtained with 3º pyramidal angle with 6 mm thickness Two primary energy absorbers exist on the car, one on each side of the centerline of the car and consist of four pyramidal thin walled tubes having 1,000 mm lengths. Each absorber is welded to and supported by the passenger car structure that is not intended to deform. The load on the outboard ends of the primary energy absorbers is applied to the back of the support plate. An initial gap exists between the outboard end of the absorber and the back of the buffer beam before activation of the crush zone (so that the absorbers do not carry any operational loads). The energy absorption capacity of primary energy absorber is 2.2 MJ within 80 cm stroke.

6.2 Effect of Cell Configuration of Honeycomb Structures on Crashworthiness Parameters

Low energy absorber component in crush zone system is honeycomb structure. Honeycomb structures collide with low and mainly constant average force and provide low acceleration/deceleration in crush patterns. A parametric study is conducted to investigate the effect of foil thickness, cell side size, cell expanding angle, impact velocity and mass on crashworthiness parameters of the honeycomb structures. Crashworthiness parameters of hexagonal honeycomb structures made of aluminum alloy A5052 under out-of-plane impact loads are numerically investigated. To verify the results of explicit nonlinear finite element models, the mean crush strength and stress-strain curve obtained from numerical solution are compared with experimental measurements and theoretical results reported in literature. It is observed that by changing the expanding angle α between 90º and 150º with constant total mass, the crush force efficiency, total energy absorption and energy absorber effectiveness parameters increase up to 120º, thereafter these parameters decrease. The honeycomb structure with 120º expanding angle yields the largest crashworthiness parameters. By changing the foil thickness between 0.025 mm and 0.0435 mm and the cell side size between 2 mm and 5 mm simultaneously where the total mass of model is constant, it is concluded that the crush force efficiency, total energy absorption and energy absorber effectiveness parameters decrease by

increasing the foil thickness and cell side size. Therefore, the honeycomb structure with small cell size and thin foil thickness has relatively larger crashworthiness parameters.

When the cell side size is constant, by changing the foil thickness between 0.01 mm and 0.05 mm, the crush force efficiency, specific energy absorption and energy absorber effectiveness factor increase slightly. In order to study the effect of impact inertia on crashworthiness parameter values, the load-deformation curves for different impact mass and velocity are obtained. It is observed that by changing the impact mass between 0.6 kg and 4.7 kg while the impact velocity is constant; higher impact mass results in increasing crushing distance, because the TEA and SEA values increase as the impact mass increases. Also an increment in the impact mass causes an increment in the energy absorber effectiveness factor. variation the initial impact velocity from 5 m/s to 14 m/s with constant impact mass results in increasing crushing distance, because the TEA and SEA values increase as the impact initial velocity increases. Also it is observed that there is a tendency of energy absorber effectiveness factor to increase with an increase in the initial impact velocity. Finally the geometric configuration of hexagonal honeycomb structure with high crashworthiness characteristic has been achieved for application in crush zone of railway passenger car. In the honeycomb box, two aluminum honeycomb blocks with the dimensions of 360 mm width, 360 length and 440 mm height are positioned. These blocks absorb the energy of 0.5 MJ in 30 cm stroke which was the design goal.

6.3 CEM System Benefits to Improve Crashworthiness of Railway Passenger Car

In order to investigate the benefits provided by the CEM system, designed crush zone is applied a N13-type used by the Turkish State Railway Company. The full scale explicit FE analysis is conducted to compare the crashworthiness performance of the passenger car having the CEM system with the conventional one. In order to compare the crashworthiness performance of the CEM system, the force-crush, acceleration, SIV, velocity diagrams and deformation modes are computed. The deformation patterns indicated the large lateral buckling happened in the occupied volume of conventional passenger car, whereas, in the passenger car having the CEM system, no damage occurs out of the crush zone area that is the first one meter of the

car. Shock tolerance of the human body in standing posture and without restraint, with pulse duration near to 0.1 s is $7ms^{-2}$. The average acceleration in car with CEM system, is about 15 times higher than safe shock. The average acceleration for conventional car is 22 times higher than safe acceleration for standing passenger without restraints. The safe acceleration limit for seating posture without restraints with pulse duration near to 0.1 s is $110ms^{-2}$. The average acceleration in car with CEM system, is safe area but the average acceleration for conventional car is 14% higher than safe acceleration limit. The safe acceleration limit for seating posture with restraints with pulse duration near to 0.1 s is $140ms^{-2}$. The average acceleration of car with CEM system, is in safe area but the average acceleration for conventional car is 1.5g higher than safe acceleration limit. The SIV value at a distance over 600 mm for conventional passenger car is found to be approximately 11.2 m/s while it is found to be approximately 7.1 m/s for the passenger car having the CEM system. Therefore, it is concluded that CEM system improved the reduction of injuries and fatalities occurring in distances over 600 mm. The comparison of velocity-time diagrams of the conventional passenger car and the passenger car having the CEM system revealed higher levels of deceleration in the conventional passenger car in comparison with the longer deceleration time and low level of deceleration in the passenger car having the CEM system. Finally, the comparison between the crashworthiness results of two types of passenger car concretely proved the effectiveness of the CEM system to improve crashworthiness of railway passenger car.

6.4 Recommendations

The benefits of CEM system have been proved for a type of passenger car traveling in Turkey railway. With consideration that European Union has own crashworthiness regulations for railway vehicle, this study can be a start for applying crashworthiness standards and regulations on design of railway passenger cars traveling in Turkey. Also car-to-car collision, two passenger car collision with rigid wall and train collision with standing train simulations give more insight about the efficiency of CEM system.

REFERENCES

[1] **Scholes, A.** (1987). Railway passenger vehicle design loads and structural crashworthiness, *Proc Institute of Mechanical Engineers, 201*, 201-207.

[2] **Mayville, R., Stringfellow, R., Rancatore, R. & Johnson, K.** (1999). Development of a passenger rail vehicle crush zone, *Proc Institute of Mechanical Engineers, 212,* 151-157.

[3] **Scholes, A. & Lewis, J.** (1993). Development of crashworthiness for railway vehicle structures, *Proc ImechE, Part F: J Rail Rapid Transit, 207*,1-16.

[4] **Lewis, J. H., Rasaiah, W. G. & Sholes, A.** (1996). Validation of measures to improve rail vehicle crashworthiness, *Proc ImechE, Part F: J Rail Rapid Transit, 210,* 73-85.

[5] **Tyrell, D. C., Jacobsen, K., J. & Martinez, E.** (2006). A Train-to-Train Impact Test of Crash Energy Management Passenger Rail Equipment: Structural Results. *ASME International Mechanical Engineering Congress and Exposition,* Chicago, Illinois, USA. 24-25 October.

[6] **Lu, G., & Yu, T.** (2003). *Energy Absorption of Structures and Materials*. Cambridge, England: Woodhead.

[7] **Sutton, A.** (2001). The development of rail vehicle crashworthiness, *Proc IMechE, Part F, J Rail Rapid Transit, 216* (2), 97–108.

[8] **Tyrell, D. & Martinez, E.** (2006). A Train-to-Train Impact Test of Crash Energy Management Passenger Rail Equipment, *The 6th International Symposium PASSIVE SAFETY OF RAIL VEHICLES*, Bahne: Germany: December 4-5.

[9] **Tyrell, D., Severson, K. & Perlman. A.B.** (2000). Single Passenger Rail Car Impact Test Volume I: Overview and Selected Results. U.S: Department of Transportation Report.

[10] **Tyrell, D., Severson, K., Perlman. A.B., Brickle, B. & VanIngen-Dunn, C.** (2000). Rail passenger equipment crashworthiness testing requirements and implementatoin, *ASME RTD, 19*, 203-209.

[11] **Xue, X. Smith, R.A. & Schmid, F.** (2005) Analysis of crush behaviors of a rail cab car and structural modifications for improved crashworthiness, *Int. J. Crashworthiness 10* (2), 125–136.

[12] **Cleon, L. M., Legait, J. & Villemin, M.** (1996). SNCF Structural crashworthiness design strategy. *Rail Vehicle Crashworthiness Symposium,* Cambridge, MA, USA: June 24-26.

[13] **Kishore, S.** (2007). Emerging development project patterns in management of rolling stock safety, *International Railway safety Conference*, Goa, India: Spetember 30- October 6.

[14] **Martinez, E., Tyrell, D. & Perlman, B.** (2004). Development of Crash Energy Management Designs for Existing Passenger Rail Vehicles, *ASME International Mechanical Engineering Congress*, Anaheim, CA: November 13-19.

[15] **Priante, M., Tyrell, D. & Perlman, B.** (2006). A Collision Dynamics Model of a Multi-Level Train, *ASME International Mechanical Engineering Congress and Exposition*, Chicago, Illinois, USA: November 5-10

[16] **Lu, G.** (2002). Energy absorption requirement for crashworthy vehicles, *Proc ImechE, Part F: J Rail Rapid Transit, 216*, 31-39

[17] **Nemeth, I., Kovacs, K., Reimerdes, H. G. & Zobory, I.** (2002). Crashworthiness study of railway vehicles developing of crash elements, *In: 8th Conference on Vehicle system dynamic*, Budapest, Hungary: November 11-13.

[18] **Url-1** <http://www.krri-crash.com/news.asp?idx=28>, date Retrieved 20.04 2013.

[19] **Gao, G. J. & Tian, H. Q.** (2007). Train's crashworthiness design and collision analysis, *J Crashworthiness*, *12*, 21-28.

[20] **Han, H. S. & Koo, J. S.** (2003). Simulation of train crashes in three dimensions, *Veh Syst Dyn*, *40*, 435-450.

[21] **Xue, X., Robinson, M., Schmid, F. & Smith, R.** (2013). Rail vehicle impact analysis: A critique of the suitability of the rigid wall model and the assumption of symmetrical behavior, *Proc ImechE, Part F: J Rail Rapid Transit*, doi: 10.1177/0954409713504393.

[22] **Sun, Y. Q., Cole, C. Dhanasekar, M. & Thambiratnam, D. P.** (2012). Modelling and analysis of the crush zone of a typical Australian passenger train, *Vehicle System Dynamics: J Vehicle Mechanics and Mobility*, *50* (7), 1137-1155.

[23] **Kirkpatrick, S. W., Schroeder, M. & Simons, J. W.** (2001). Evaluation of passenger rail vehicle crashworthiness, *J Crashworthiness, 6* (1), 95-106.

[24] **Simic, G., Lucanin, V. & Milkovic, D.** (2006). Elements of passive safety of railway vehicle in collision, *J Crashworthiness*, *11*, 357-369.

[25] **Xie, S. & Tian, H.** (2013). Dynamic simulation of railway vehicle Occupants under secondary impact, *Vehicle System Dynamics: J Vehicle Mechanics and Mobility*, *51* (12), 1803-1817.

[26] **Xie, S. C. & Tian, H. Q.** (2013). Influencing factors and sensitivity analysis of occupant impact injury in passenger compartment, *Traffic Injury Prev. Traffic Injury Prevention*, *14* (8), 816-822.

[27] **Xue. X., Schmid, F. & Smith, R. A.** (2004) A study of modeling approaches for rail vehicle collision behavior, *J Crashworthiness*, *9*, 515-525.

[28] **Xue. X., Schmid, F. & Smith. R. A.** (2007). Analysis of the structural characteristics of an intermediate rail vehicle and their effect on vehicle crash performance, *Proc ImechE, Part F: J Rail Rapid Transit, 221*, 339-352.

[29] **Amraei, M., Shahravi, M., Noori, Z. & Lenjani, A.** (2013). Application of aluminum honeycomb sandwich panel as an energy absorber of high-speed train nose, *J Com. Mat*, doi: 10.1177/0021998313482019.

[30] **Mehryari, R., Ismarrubie, Z. N., Zainudin, E. S. & Tang, S. H**. (2012). Effect of length on crashworthiness parameters and failure modes of steel and hybrid tube made by steel and GFRP under low velocity impact, *J Crashworthiness, 17* (3), 319-325.

[31] **Grasso, M.** (2013). About the preliminary design of a self-aligning energy absorber system for railway vehicles, *J Crashworthiness, 18* (5), 544-557.

[32] **Laberge-Nadeau, C., Bellavance, F., Messier, S.,Vezina, L. & Pichette, F**. (2009). Occupant injury severity from lateral collisions: a literature review, *Journal of Safety Research, 40*, 427-435.

[33] **Wang, W., Zhang, G., Zhao, H. & Lu, Z.** (2008). Second impact effect of chair distance of high-speed train on occupant injury, *International Journal of Computer Aided Engineering and Technology, 17*, 1-3.

[34] **Hosseini-Tehrani, P. & Bayat, V.** (2011). Study on crashworthiness of wagon's frame under frontal impact, *J Crashworthiness, 16* (1), 25-39.

[35] **APTA SS-C&S-034-99** (2006). *Standard for the design and construction of passenger railroad rolling stock*. Retrieved from http://www.apta.com/resources/standards/Documents/APTA-PR-CS-S-034-99.

[36] **European Standard EN 15227** (2008). *Railway application-crashworthiness requirements for railway vehicle bodies.* Retrieved from http://law.resource.org/pub/bg/ibr/bds.en.15227.2010.

[37] **Marsolek, J. & Reimerdes, H. G.** (2004). Energy absorption of metallic cylindrical shells with induced non-axisymmetric folding patterns, *International Journal of Impact Engineering, 30*, 1209–1223.

[38] **Alavinia, A. & Hamedani, J. H.** (2010). Comparative analysis of energy absorption and deformations of thin walled tubes with various section geometries, *Thin- Walled Structures, 48* (12), 946–954.

[39] **Alavi Nia, A. & Parsapour, M.** (2014). Comparative analysis of energy absorption capacity of simple and multi-cell thin-walled tubes with triangular, square, hexagonal and octagonal sections, *Thin-Walled Structures, 74*, 155–165.

[40] **Jones, N.** (2010). Energy absorbing effectiveness factor, *International Journal of Impact Engineering, 37* (6), 754-765.

[41] **Song, J. & Guo, F.** (2013). A comparative study on the windowed and multi-cell square tubes under axial and oblique loading, *Thin-Walled Structures, 66*, 9–14.

[42] **Algalib, D. & Limam, A**. (2004). Experimental and numerical investigation of static and dynamic axial crushing of circular aluminum tubes, *Thin-Walled Structures*, *42* (8), 1103–1137.

[43] **Zhang, X.W., H. Su & Yu, T.X.** (2009). Energy absorption of an axially crushed square tube with a buckling initiator, *International Journal of Impact Engineering*, *36* (3), 402–417.

[44] **Aljawi, A. A. N., Abd-Rabou, M. & Asiri, S.** (2004). Finite element and experimental analysis of square tubes under dynamic axial crushing, *European Congress on Computational Methods in Applied Sciences and Engineering*, Jyväskylä, Finland: July 24–28.

[45] **Zhang, X. & Cheng, G.** (2007). A comparative study of energy absorption characteristics of foam-filled and multi-cell square columns, *International Journal of Impact Engineering*, *34* (11), 1739–52.

[46] **Zhang, X. & Huh, H.** (2009). Energy absorption of longitudinally grooved square tubes under axial compression, *Thin-Walled Structures*, *47* (12),1469–1477.

[47] **Nagel, G. & Thambiratnam, D.** (2006). Dynamic simulation and energy absorption of tapered thin-walled tubes under oblique impact loading, *International Journal of Impact Engineering*, *32* (10), 1595–620.

[48] **Lee, S., Hahn, C., Rhee, M. & Oh, J. E.** (1999). Effect of triggering on the energy absorption capacity of axially compressed aluminum tubes, *Materials and Design*, *20* (1), 31–40.

[49] **Jandaghi Shahi, V. & Marzbanrad, J.** (2012). Analytical and experimental studies on quasi-static axial crush behavior of thin-walled tailor-made aluminum tubes, *Thin-Walled Structures*, *60*, 24–37.

[50] **Hong, W., Jin, F., Zhou, J., Xia, Z., Xu, Y., Yang, Y., Zheng, Q. & Fan, H.** (2013). Quasi-static axial compression of triangular steel tubes, *Thin-Walled Structures*, *62*, 10–17.

[51] **Mahdi, E. & Sebaey, T. A.** (2014). An experimental investigation into crushing behavior of radially stiffened GFRP composite tubes, *Thin-Walled Structures*, *76*, 8–13.

[52] **Gupta, P. K. & Gupta, N. K.** (2013). A study on axial compression of tubular metallic shells having combined tube–cone geometry, *Thin-Walled Structures*, *62*, 85–95.

[53] **Salehghaffari, S., Tajdari, M., Panahi, M. & Mokhtarnezhad, F**. (2010). Attempts to improve energy absorption characteristics of circular metal tubes subjected to axial loading, *Thin-Walled Structures*, *48* (6), 379–90.

[54] **Zhao, H. & Gary, G.** (1998). Crushing behavior of aluminum honeycombs under impact loading, *Int J Impact Eng*, *21*, 827-836.

[55] **Url-2** <http://www.hexcel.com/Resources/honeycomb-data-sheets>, date retrieved 20.04.2012.

[56] **Zhang, J. & Ashby, M. F**. (1992). The out-of-plane properties of honeycombs, *Int J Mech Sci*, *34* (6), 475-489.

[57] **Deqiang, S., Weihong, Z. & Yanbin, W.** (2010). Mean out-of-plane dynamic plateau stresses of hexagonal honeycomb cores under impact loadings, *J Composite Structures, 92*, 2609-2621.

[58] **Mellquist, E. C. & Waas. A. M**. (2004). Size effects in the crushing of honeycomb structures. In: 45th AIAA/ASME/ASCE/AHS/ASC structures, structural dynamics & materials conference. Palm Springs, California.

[59] **Yin, H. & Wen, G**. (2011). Theoretical prediction and numerical simulation of honeycomb structures with various cell specifications under axial loading. *Int J Mech Mater Des*, 7, 253-263.

[60] **Gotoh, M., Yamashita, M. & Kawakita, A.** (1996). Crush behavior of honeycomb structure impacted by drop-hammer and its numerical analysis, *Mater Sci Res Int, 2* (4), 261-266.

[61] **Yamashita, M. & Gotoh, M.** (2005). Impact behavior of honeycomb structures with various cell specifications-numerical simulation and experiment, *Int J Impact Eng, 32* (1), 618-630.

[62] **Hou, B., Pattofatto, S., Li, Y. L. & Zhao, H.** (2011). Impact behavior of honeycombs under combined shear-compression, part II analysis, *Int J Solids Struc, 48* (5), 698 (697).

[63] **Hu, L. L. & Yu, T. X.** (2010). Dynamic crushing strength of hexagonal honeycombs, *Int J Impact Eng, 37*, 467–74.

[64] **TrongNhan, T., Hou, S., Han, X. & Nguyen, N.** (2014). Theoretical prediction and crashworthiness optimization of multi-cell triangular tubes, *Thin-Walled Structures, 82*, 183–195.

[65] **Hou, S., Han, X., Sun, G., Long, S., Li, W., Yang, X. & Li, Q.** (2011). Multiobjective optimization for tapered circular tubes, *Thin-Walled Structures, 49*, 855–863.

[66] **Qi, C., Shu Yang, S. & Dong, F.** (2012). Crushing analysis and multiobjective crashworthiness optimization of tapered square tubes under oblique impact loading, *Thin-Walled Structures, 59*, 103–119.

[67] **Yin, H., Wena G., Zhibo Liu, Z. & Qing, Q.** (2014). Crashworthiness optimization design for foam-filled multi-cell thin-walled structures, *Thin-Walled Structures, 75*, 8–17.

[68] **Fang, H., Rais-Rohani, M., Liu, Z. & Horstemeyer, M.** (2005). A comparative study of metamodeling methods for multiobjective crashworthiness optimization, *Comput Struct 83*, 2121–36.

[69] **Hou, S., Li, Q., Long, S., Yang, X. & Li, W.** (2008). Multiobjective optimization of multi-cell sections for the crashworthiness design, *International Journal of Impact Engineering, 35* (11), 1355-1367.

[70] **Liu**, **Y.** (2008a). Crashworthiness design of multi-corner thin-walled columns, *Thin-Walled Structures, 46* (12), 1329-1337.

[71] **Chiandussi, G. & Avalle, M.** (2002). Maximization of the crushing performance of a tubular device by shape optimization, *Computers and Structures, 80*, 2425–2432.

[72] **Liu, Y**. (2008b). Design optimization of tapered thin-walled square tubes, *International Journal of Crashworthiness, 13* (5), 543-550.

[73] **Zarei, H. R. & Kröger, M**. **(**2006). Multiobjective crashworthiness optimization of circular aluminum tubes, *Thin-Walled Structures, 44* (3), 301-308.

[74] **Cho, Y. B., Bae, C. H., Suh, M. W. & Sin, H. C**. (2006). A vehicle front frame crash design optimization using hole-type and dent-type crush initiator, *Thin-Walled Structures, 44*, 415–428.

[75] **Kim, H. S., Chen, W. & Wierzbicki, T**. (2002). Weight and crash optimization of foam-filled three-dimensional-S frame, *Computational Mechanics, 28* (5), 417-424.

[76] **Zarei, H. R. & Kröger, M. (**2008b). Optimization of the foam-filled aluminum tubes for crush box application, *Thin-Walled Structures, 46* (2), 214-221.

[77] **Zhang, X., Cheng, G., Wang, B. & Zhang, H.** (2008). Optimum design for energy absorption of bitubal hexagonal columns with honeycomb core, *International Journal of Crashworthiness, 13* (1), 99-107.

[78] **Yamazaki, K. & Han, J**. (2000). Maximization of the crushing energy absorption of cylindrical shells, *Advances in Engineering Software, 31* (6), 425-434.

[79] **Hou, S., Li, Q., Long, S., Yang, X. & Li, W.** (2007). Design optimization of regular hexagonal thin-walled columns with crashworthiness criteria, *Finite Elements in Analysis and Design, 43* (7), 555–565.

[80] **Toksoy, A. K. & Guden, M**. (2011). The optimization of the energy absorption of partially Al foam-filled commercial 1050H14 and 6061T4 Al crash boxes, *International Journal of Crashworthiness, 16* (1), 97–109.

[81] **Partovi-Meran, A. & TOPRAK T.** (2011). Comparative Non-linear Finite Element Analysis of Thin Walled Tubes Under Axial Impact Load, *International Symposium on Advances in Applied Mechanics and Modern* (pp. 223-227), Baku, Azerbaijan, 22-23 September.

[82] **ABAQUS.** (2010). User's Manual Ver. 6.10 Dausault Systems Inc. Retrieved from http://www.tu-chemnitz.de/v6.10/usb-link.htm

[83] **American Iron and Steel Institute.** Retrieved December 20, 2013, from http://www.steel.org/

[84] **Liu, Y. C.** (2009). Collapse behaviour and simplified modeling of triangular cross section columns, *Indian Journal of Engineering and Materials Sciences, 16*, 71–8.

[85] **Abramowicz, W. & Wierzbicki, T.** (1989). Axial crushing of multicorner sheet metal Columns, *Journal of Applied Mechanics, 56*, 113-124.

[86] **Wierzbicki T.** (1983). Crushing analysis of metal honeycombs, *Int J Impact Eng, 1* (2),157-74.

[87] **Partovi-Meran, A., Toprak, T. & Muğan, A.** (2014). Numerical and experimental study of crashworthiness parameters of honeycomb structures, *Thin-Walled Structures, 78*, 87–94.

[88] **Montgomery, D. C**. (1997). *Design of Experiments*. London, England: John Wiley & Sons Inc.

[89] **Myers, H. R. & Montgomery, D. C**. (1995). *Response surface methodology: process and product optimization using designed experiments*, London, England: John Wiley & Sons.

[90] **Altair HyperWorks/Hypermesh.** (2011). *User's Manual Ver. 11.4.* Retrieved from http://www.altairhyperworks.com/TrainingHome.aspx

[91] **Baykasoglu, C., Sunbuloglu, E., Bozdag, E., Aruk, F., Toprak, T. & Mugan, A.** (2011). Railroad passenger car collision analysis and modifications for improved crashworthiness, *J Crashworthiness, 16*(3), 319–329.

[92] **Hong, S. T., Pan, J., Tyan, T. & Prasad, P.** (2006). Quasi-static crush behavior of aluminum honeycomb specimens under compression dominant combined loads, *International Journal of Plasticity*, *22*, 73–109.

[93] **Baykasoglu, C., Mugan, A., Sunbuloglu, E., Bozdag, E., Aruk, F. & Toprak, T.** (2013). Rollover crashworthiness analysis of a railroad passenger car, *J Crashworthiness, 18* (5), 492-501.

[94] **Riazi, S., Feizi, M. M. & Hosseini-Tehrani, P**. (2012). Improving crashworthiness in railcar against rollover, *Trans. Can. Soc. Mech. Eng*, *36* (4), 383–397.

[95] **Griffin, M., J.** (1996). *Handbook of Human Vibration*, Amsterdam, Holland: Elsevier.

[96] **EN 12663** (2010). *Railway Applications - Structural Requirements Of Railway Vehicle Bodies*. Retrieved from http://shop.austrian-standards.at/Preview.action

[97] **Uniform technical prescriptions concerning the approval of railway large passenger vehicles.** (2013). Retrieved Marth 23, 2013 from http://www.unece.org

[98] **Carolan, M., Tyrell, D. & Perlman, A.** (2007). Performance efficiency of a crash energy management system, *ASME/IEEE Joint Rail Conference & Internal Combustion Engine Spring Technical Conference*, Pueblo, Colorado, USA: March 13-16.

[99] **Partovi-Meran, A., Baykasoğlu, C., Mugan, A. & Toprak, T.** (2014). Development of crash energy management system design for a railway passenger car, *Int Journal of Rail and Rapid Transit*. doi: 10.1177/0954409714533321.

CURRICULUM VITAE

Name Surname **:** Ahmad PARTOVI MERAN

Place and Date of Birth: TEBRİZ- 23/09/1980

E-Mail **:** ahmad.partovi@gmail.com

EDUCATION:

- **B.Sc.** **:** 2003**,** K.N.T. Uni. of Tech, Mechanical Eng., Mechanical Engineering
- **M.Sc.** **:** 2006**,** Bu-Ali Sina University, Eng. Fac., Mechanical Engineering

PROFESSIONAL EXPERIENCE AND REWARDS:

- Researcher Assistant, Istanbul Technical University, Mechanical Engineering Faculty (2012-Present).
- Member of EPC Project management team & Steel Structure construction and Execution Supervisor in Direct Reduction Iron Plant- Azerbaijan Steel Project; : Khatam Al Anbia- Canymes Consortium (2007-2008).
- Hydrostatic & Pneumatic Test Supervisor in Phase 6,7& 8 South Pars (Asalueh) Gas Refineries Project; Yekan Foolad Co. (2004-2006).
- Responsibilities: Technical Study Expert in Feasibility study projects; Tarhyar Research & Technical services Co. (2003-2004 Part time).
- TÜBİTAK-2215 Graduate Scholarship Program For International Students (2009-2012).

PUBLICATIONS/PRESENTATIONS ON THE THESIS

- **Partovi Meran**, **A.**, Toprak, T., Mugan, A. (2013). "Design of a Crush Zone System for a Railway Passenger Car to Improve Crashworthiness", *JESTECH, 16* (2), 67-73.
- **Partovi Meran, A.**, Toprak,T., Muğan, A. (2014). Numerical and experimental study of crashworthiness parameters of honeycomb structures, *Thin-Walled Structures 78*, 87–94.
- **Partovi Meran**, **A.**, Baykasoğlu, C., Mugan, A., Toprak, T. (2014). Development of crash energy management system design for a railway passenger car, *International Journal of Rail and Rapid Transit*, doi: 10.1177/0954409714533321.
- **Partovi Meran, A.**, TOPRAK, T. Comparative Non-linear Finite Element Analysis of Thin Walled Tubes Under Axial Impact Load, *International Symposium on Advances in Applied Mechanics and Modern*, Baku, Azerbaijan: September 22-23.

- **Partovi Meran, A.**, Toprak, T., Mugan, A. (2012). Design of a Crush Zone System for a Railway Passenger Car to Improve Crashworthiness, *1th International Workshop on Railway Systems Engineering (IWRSE'12)*, Karabuk, Turkey: October 11-13.

LIST OF OTHER PUBLICANTS AND PATENTS:

- Sadeghi-Mehr, M., **Partovi Meran, A.** (2008). Torsional properties of cortical bone in longitudinal and transverse directions, *Bone, 43,* S111-S126, S17.
- **Partovi Meran, A.**, Sadeghi-Mehr, M. (2007). Effect of loading rate on the Torsional Properties of Cortical Bone, *24th DANUBIA-ADRIA symposium on Developments in Experimental Mechanics*, Sibiu, Romania: September 19-22,